

**NEURAL CYTOSKELETON MODULATION AFTER TRANSIENT ISCHEMIC ATTACK
AND REGION-SPECIFIC BRAIN METABOLISM INSIGHTS**

Linshu Wang, M.D., Ph.D.

APPROVED:

Shaohua Yang, M.D., Ph.D.; Major Professor

Nathalie Sumien, Ph.D.; Committee Member

Derek Schreihofner, Ph.D.; Committee Member

Ran Liu, M.D.; Committee Member

Lisa Hodge, Ph.D.; University Member

David Siderovski, Ph.D.; Chair, Department of Pharmacology and Neuroscience

Michael Mathis, Ph.D.; Dean, School of Biomedical Science

NEURAL CYTOSKELETON MODULATION AFTER TRANSIENT ISCHEMIC ATTACK
AND REGION-SPECIFIC BRAIN METABOLISM INSIGHTS

DISSERTATION

Presented to the Graduate Council of
The School of Biomedical Sciences
University of North Texas
Health Science Center at Fort Worth
In partial Fulfillment of the Requirements

For the Degree of
DOCTOR OF PHILOSOPHY

By

Linshu Wang, M.D.

Fort Worth, Texas

July 2022

ACKNOWLEDGEMENT

I would like to express my sincere gratitude to my major professor Dr. Shao-hua Yang for his excellent mentorship and training during the past five years of my graduate career. His guidance, patience, and encouragement make the challenges on this uneasy journey more manageable. He has taught me not only on the scientific thinking, but the ability to troubleshoot problems in science and in life. I also like to thank other members of my advisory committee: Drs. Nathalie Sumien, Derek Schreihof, Ran Liu, Lisa Hodge, as well as our department chair Dr. David Siderovski. I am grateful for having them to share their wisdom and offer constructive suggestions on my research project and career development. Each of you has played a critical role in my success. I also want to recognize my lab members (Ali Winters, Kiran Chaudhari, Yuanhong Sun, Ran Liu) and my friends, your companion and support definitely add significance values and meanings to my life. A special thanks to my family. Words cannot express how grateful I am to my parents, grandparents for all of the sacrifices that you've made on my behalf. Last, I would also like to thank my beloved husband—Jiangnan. Thank you for supporting me for everything, and especially I can't thank you enough for encouraging me throughout this experience.

TABLE OF CONTENTS

ACKNOWLEDGEMENTS	i
TABLE OF CONTENTS	ii
LIST OF ILLUSTRATION	v
INTRODUCTION	1
1. Transient ischemic attack.....	1
1.1 Definition and pattern of TIA.....	1
1.2 Microstructure changes and damage after TIA.....	2
1.3 Rodent TIA model.....	3
2. Ischemia-induced AD-related biomarkers, neuronal cytoskeletal modification, and neuroinflammation.....	4
2.1 Ischemia-induced AD-related biomarkers.....	4
2.2 Ischemia-induced neuronal cytoskeletal modification.....	5
2.2.1 Microtubule associated proteins (MAPs)	6
2.2.2 Neurofilament (NF)	8
2.3 Neuroinflammation.....	9
2.3.1 Microglia.....	10
2.3.2 Astrocyte.....	12
3. Glucose metabolic regulation in brain function and diseases.....	14

CHAPTER 1 (Summary and keywords)	16
1. Introduction.....	18
2. Materials and methods.....	19
2.1 Animals.....	19
2.2 Surgical procedures.....	19
2.3 Behavior test.....	20
2.3.1 Garcia neurological test.....	20
2.3.2 Cylinder Test.....	20
2.4 Sample preparation and Western blot analysis.....	20
2.5 Immunohistochemistry and TUNEL Staining.....	21
2.6 Imaging analysis.....	22
2.7 Data collection and statistics.....	22
3. Results.....	23
3.1 Establishment of recurrent TIAs model based on TIA definition.....	23
3.2 BACE1 expression and vascular endothelial growth factor (VEGF) expression after recurrent TIA.....	24
3.3 Neuronal cytoskeletal modification induced by recurrent TIA.....	24
3.4 Recurrent TIA induces astrogliosis and microgliosis.....	26
3.5 White matter modification in response to recurrent TIA.....	26
4. Conclusion.....	27
CHAPTER 2 (Summary and keywords)	33
1. Introduction.....	34
2. Materials and methods.....	35

2.1 Animals.....	35
2.2 Preparation of acute brain slices.....	35
2.3 Tissue punching and Seahorse XFe96 analysis.....	36
2.4 Immunohistochemistry and confocal microscopy.....	37
2.5 Western blots.....	38
2.6 Data collection and statistical analysis.....	38
3. Results.....	40
3.1 Region-specific glucose metabolic profile of the young and old rat brain.....	40
3.2 Region-specific glucose metabolic profile of the mouse brain.....	42
3.3 Oxidative phosphorylation efficiency of mouse brain.....	43
3.4 Region-specific metabolic signaling in the mouse brain.....	44
4. Conclusion.....	44
DISCUSSION AND FUTURE DIRECTION.....	52
1. Recurrent TIA induces neuronal cytoskeleton change and gliosis.....	52
2. Region-specific metabolic profile of the brain.....	54
BIBLIOGRAPHY.....	57
FIGURES.....	85
APPENDIX.....	158

LIST OF ILLUSTRATION

Table 1. Antibodies used in Western blots and immunofluorescence.....	85
Figure 1. A schema depicts the process of recurrent TIA, behavior assessment, and tissue harvest	86
Figure 2. Behavior assessment and body weight measurements after recurrent TIA, ischemic stroke, and sham groups	88
Figure 3. A schema depicting the location and region collected for tissue analysis from recurrent TIA samples.....	90
Figure 4. Terminal deoxynucleotidyl transferase-mediated dUTP nick-end labeling (TUNEL) staining on day-1,3,7 after recurrent TIA.....	92
Figure 5. Beta-site amyloid precursor protein (APP) cleaving enzyme-1 (BACE1) alteration after recurrent TIA.....	94
Figure 6. Vascular endothelial growth factor (VEGF) alteration after recurrent TIA.....	96
Figure 7. Recurrent TIA-induced phospho-tau and tau alteration in Western blot.....	98
Figure 8. Confocal microscopy of p-tau (S396) and tau alteration after recurrent TIA...	100
Figure 9. Immunofluorescent quantitative analysis of total tau alteration after recurrent TIA.....	102
Figure 10. Immunofluorescent quantitative analysis of p-tau (Ser396) alteration after recurrent TIA.....	104
Figure 11. Recurrent TIA-induced phospho-tau (AT8) in Western blot.....	106

Figure 12. Confocal microscopy of p-tau (AT8) and tau alteration after recurrent TIA...	108
Figure 13. Microtubule-associated protein 2 (MAP2) reduction induced by recurrent TIA by Western blots.....	110
Figure 14. Confocal images of MAP2 expression on PSD1/3/7 after recurrent TIA.....	112
Figure 15. Immunofluorescent quantitative analysis of MAP2 alteration after recurrent TIA.....	114
Figure 16. Neurofilament-Light (NFL) elevation after recurrent TIA by Western blots...	116
Figure 17. Confocal image and quantitative analysis of Neurofilament-Light (NFL) elevation after recurrent TIA.....	118
Figure 18. Glial fibrillary acidic protein (GFAP) induction after recurrent TIA by Western blots.....	120
Figure 19. Confocal image and quantitative analysis of Glial fibrillary acidic protein (GFAP) elevation after recurrent TIA.....	122
Figure 20. Confocal image and quantitative analysis of ionized calcium binding adaptor molecular 1 (Iba1) alteration after recurrent TIA.....	124
Figure 21. Neurofilament-light (NFL), glial fibrillary acidic protein (GFAP) alteration in corpus callosum in response to recurrent TIA.....	126
Figure 22. Ionized calcium binding adaptor molecular 1 (Iba1) alteration in corpus callosum in response to recurrent TIA.....	128
Figure 23. Triple staining of NFL, GFAP, Iba1 and DAPI for potential interaction in corpus callosum induced by recurrent TIA.....	130
Figure 24. Myelin binding protein (MBP) alteration in corpus callosum in response to recurrent TIA.....	132

Figure 25. Schematic of pathological changes after recurrent TIA.....134

Figure 26. Metabolic analysis of acute tissue punches (0.5 mm diameter) from rodent brain sections (180 μ m thick)136

Figure 27. Optimization of brain punch size for metabolic analysis using XF96 analyzer..... 138

Figure 28. Metabolic analysis of cerebral cortex (CX), basal ganglia (BG), and cerebellum (CE) punches from a 3-month-old female rat using Seahorse XF96 analyzer.....140

Figure 29. Metabolic analysis of in hippocampal CA1, dentate gyrus (DG), and CE punches from 3-month-old female rat using a Seahorse XFe96 analyzer.....142

Figure 30. Metabolic analysis of CX, BG, and CE punches from a 12-month-old female rat using a Seahorse XFe96 extracellular flux analyzer.....144

Figure 31. Metabolic analysis of CX, BG, and CE punches from a 3-month-old female mouse using a Seahorse XFe96 extracellular flux analyzer.....146

Figure 32. Metabolic analysis of hippocampal (CA1), DG, and CE punches from a 3-month-old female mouse using a Seahorse XFe96 extracellular flux analyzer.....148

Figure 33. Optimization of mitochondrial complex V inhibition and measurement of non-mitochondria respiration, ATP production-linked respiration, and proton leak-linked respiration in the cerebral cortex and cerebellum.....150

Figure 34. Inhibition of uncoupling proteins decreased proton leak coupled OCR in cerebral cortex punches..... 152

Figure 35. Immunohistochemistry of GFAP, NeuN, and DAPI depict different cellular components of different brain regions.....154

Figure 36. Cellular composition and metabolic signaling in different mouse brain regions.....156

INTRODUCTION

1. Transient ischemic attack (TIA)

1.1 Definition and pattern of TIA.

Strokes are classified into hemorrhagic, ischemic stroke and transient ischemic attack. As a “Mini-stroke”, transient ischemic attack (TIA) used to be a symptomatic diagnosis disease with signs and symptoms disappear quickly. Recently, American Heart Association (AHA) and the American Stroke Association (ASA) council has revised the TIA definition from time-based (less than 24-hour symptom) to tissue-based as a sudden onset of focal neurological symptoms caused by focal brain, spinal cord or retinal ischemia without acute infarction. ¹ TIA incidence is half a million per year with the prevalence at 2%, which is approximately five million individuals in the United States. ² However, up to 40% of stroke patients reported experiencing TIA episodes before stroke, suggesting that TIA incidence could be even much higher. ³ TIA usually occurs more than once. Previous reports indicate that 68% of patients recurrence around 2-5 times in the following-up 16 months after the initial TIA, and 56% of patients have recurrent episode within one month. ⁴ Recurrent TIA within 7 days is associated with a higher risk of severe stroke than after a single TIA. ³⁻⁵ TIA, as well as ischemic stroke, has been reported as a high-risk factor for delayed on-set dementia, Alzheimer Disease (AD) and AD-related dementia (ADRD) ^{6,7}, besides, white matter damage in TIA patients correlates with early cognitive decline ⁸, demonstrating its essential role as a cerebrovascular factor

contributing to AD or ADRD.^{9,10} However, TIA has received only little attention in the experimental research field compared with ischemic stroke and hemorrhagic stroke, and its pathophysiology have been less studied.

1.2 Microstructure changes and damage after TIA

The traditional TIA definition was based on self-resolving neurological deficits within 24 hours of onset. However, full functional recovery does not indicate absence of neuropathological changes in the central nervous system. Early magnetic resonance imaging (MRI) has shown TIA-associated infarct in 46-81% diagnosed TIA patients.^{11,12} Diffusion-weighted MRI (DWI) lesion are frequently observed in TIA patients.¹ White matter hyperintensity (WMH) has been found in TIA patients and can be potentially used as a neuroimaging marker for TIA diagnosis certainty.¹³ WMH often involves more than one structure, and several pathological changes have been noted, including axonal and myelin disruption, astrogliosis, or microglia activation in periventricular white matter.¹⁴ Furthermore, decreased fractional anisotropy has been found in TIA patients even without DWI lesion.¹⁵ Functional MRI (fMRI) recently showed a decreased resting state network connectivity with reduced regional homogeneity at 1-month after onset of TIA symptoms.^{16,17} An electroencephalography (EEG) study has shown enhanced focal slow wave activity in TIA patients for up to 1 month even without DWI lesion in the brain.¹⁸ Besides, clinical studies indicate TIA patients exhibit Blood-Brain-Barrier (BBB) dysfunction using MRI diffusion-weighted imaging.¹⁹ In an experimental setting of TIA model, consistent cortical selective neuronal loss with microglia activation was observed in rats even without

MRI lesion and necrosis.²⁰ Transient ischemia can also decrease cerebral blood volume (CBV), leading to increase neural activity, which may potentially impair neural integrity and contribute to subsequent vascular consequence.²¹ Neuronal apoptosis and neurovascular impairment has been found without DWI and T2-weighted MRI (T2WI) lesion in mouse model, evidenced by decreased vascular density in TIA-affected cortical and striatum region at the acute stage.²² These studies suggest that TIA may induce microstructure modification and damage in the brain even without detected infarct.

1.3 Rodent TIA model

An appropriate TIA animal model to mimic human TIA characteristics should be set up to help exploring pathological changes of TIA. TIA animal models using rodents are rarely found in literature review. Three criteria should be met for an experimental TIA model based on TIA definition: a successful occlusion and reperfusion, no sensorimotor deficit observed at 24 hours after reperfusion, and no detected infarct lesion.²³ The rodent intraluminal suture middle cerebral artery occlusion (MCAO) model is the most widely used and reliable experimental stroke model that revealed many aspects of ischemic stroke pathophysiology.²⁴⁻²⁶ Dr. T. Tatlisumak et.al have developed an optimized TIA model by MCAO in both NMRI mice and Wistar rats.^{27,28} They found that 12.5-min MCAO is the threshold for inducing MRI-detected infarction. 10-min or shorter MCAO proved a suitable TIA model with no acute infarction and neurological deficits confirmed by MRI and neurological score, as well as no significant increase of terminal deoxynucleotidyl transferase-mediated dUTP nick-end labeling (TUNEL)-positive cells. Besides, 5- and 10-

min MCAO in male Sprague-Dawley rats also showed no neurological deficit in Garcia score with no infarct in the TIA-affected cortical and basal ganglia region within 24 hours after reperfusion.²⁹ Swiss Albino mice exhibited selective neuronal necrosis up to 3 days following 15-min distal MCAO, and 15-min MCAO in Spontaneously Hypertensive rats have shown consistent selective neuronal loss, microgliosis and neurological deficit during the subacute and chronic phase.²⁰ Thus, preliminary MCAO experiments from 10-15 min duration to detect the infarction threshold in different strain need to be determined when applying TIA model in rodents.

2. Ischemia-induced AD-related biomarkers, neuronal cytoskeletal modification, and neuroinflammation

2.1 Ischemia-induced AD-related biomarkers.

Although cerebrovascular disease has been considered as an exclusion criterion for Alzheimer disease clinical diagnosis,³⁰ emerging evidence has shown the significance contribution of cerebrovascular factors to cognitive decline and neurodegeneration in AD. Vascular diseases share common risk factors with AD, such as diabetes, atherosclerosis, hypertension etc., evidenced by populational-based epidemiological studies.³¹ Cerebral blood flow decrease with reduced brain blood metabolism have been observed in AD patients.^{32 33} Besides, previous case reports demonstrated the patients who have ischemic stroke with small lesion which would not impair cognitive function, further developed dementia during the follow-up period, indicating AD might interact with cerebrovascular dysfunction to aggravate the outcome of the disease.³⁴ In 2011, Dr. Zlokovic brought up the two-hit vascular hypothesis of AD. The hypothesis states that

vascular risk factors (diabetes, stroke, or cardiac disease) may trigger the cerebrovascular damage, including BBB dysfunction and oligemia as primary damage (hit 1). BBB dysfunction and oligemia further initiates non-amyloidogenic pathway that contributes to neuronal dysfunction and damage mediated by toxin accumulation and capillary hypoperfusion, on the other hand, BBB dysfunction and oligemia can also induce amyloidogenic pathway by inhibiting clearance or enhancing production of amyloid beta, leading to amyloid beta accumulation and tau hyperphosphorylation (hit 2), which further aggravate neuronal dysfunction and accelerate the progression of neurodegeneration.³⁵ Ischemic stroke and TIA are associated with high risk of AD and ADRD.^{9,10} Increased expression and activity of amyloid precursor protein cleaving enzyme-beta secretase (BACE1) has been found after ischemic stroke model, which may support the two-hit hypothesis to AD and partially explain epidemiological study that cerebrovascular changes can coexist with AD.^{36,37} In the current study, we aimed to investigate if TIA can induce the AD-related biomarkers which have been recognized following ischemic stroke.

2.2 Ischemia-induced neuronal cytoskeletal modification.

The neuronal cytoskeleton is a 3-dimensional lattice composed of actin filaments, neurofilaments, and microtubules. The recent studies of neuronal cytoskeleton under physiological and pathological conditions have advanced our knowledge on its vital role in the central nervous system (CNS) beyond mere scaffolding.³⁸ Neuronal cytoskeleton participates in the axonal guidance and growth, maintaining neuronal homeostatic plasticity and regulation of axonal regeneration after damage or neurodegeneration.^{39,40} The altered neuronal cytoskeleton has been recognized as the hallmarks of many

neurodegenerative diseases, for instance, tauopathy and neurofilament-light aggregation have been recognized in AD pathology.⁴¹ Ischemic injury can induce retraction or loss of neuronal dendritic spines and axons which contribute to functional disability even when the parent neuron survives.^{42,43} The injured neurons further undergo axonal regeneration or regrowth for neurite network reconstruction to promote functional recovery following CNS injury.⁴⁴ All these neuronal morphological and functional changes are closely associated with dynamic cytoskeletal remodeling and organization. Given the close linkage between cerebrovascular dysfunction and AD, together with the strong evidence supporting the vital role of cytoskeletal alteration in AD pathology, the neuronal cytoskeletal modification as a response to cerebral ischemia has been receiving notable attention for exploring new therapeutic targets to prevent and slow down the progression of AD and ADRD.

2.2.1 Microtubule associated proteins (MAPs)

MAPs are the family of proteins that interact with microtubules (MTs) to regulate its dynamics and stability. MAP2/tau family include neuronal MAP2, tau and non-neuronal MAP4. Tau and MAP2 are stabilizing MT associated proteins, whose functions are predominantly mediated by phosphorylation to maintain or reorganize MT bundles. MAP2 is mainly expressed in soma and dendrites with mixed orientation, which has higher and lower molecular weight isoforms: MAP2a, 2b (~270kDa), MAP2c, 2d (~70kDa).⁴⁵ Tau is primarily distributed in neuronal axons with distinct polarity and at the lower expression in oligodendrocytes and astrocytes. It has six major isoforms in the brain, and perform the function of neuronal morphology maintenance, axonal formation and transport

modulation.⁴⁶ Only MAP2 can bundle actin filament, which may promote neurite initiation, contributing to the neuronal functional difference between MAP2 and tau.⁴⁵

In the setting of ischemia, a diminished MAP2 immunoreactivity has been widely recognized as a sensitive ischemic marker in various cerebral ischemia/hypoperfusion models established in gerbil,^{47,48} rats,^{49,50} monkeys,⁵¹ or even human cases.⁵² MAP2-related immunoreactivity intensity shows rapid reduction as early as 2 hours after mild and severe cerebral ischemia, and it proves to be a promising candidate to identify core region, as well as perilesional region.⁵³ In response to ischemia, calpain-mediated proteolytic degradation is primarily responsible for MAP2 loss. In hippocampal slice, OGD can activate NMDA receptor and trigger calcium influx, contributing to MAP2 degradation and redistribution from dendrites to somata, which can be alleviated by calpain inhibitor,⁵⁴ suggesting a critical role of calpain as calcium-dependent enzyme in ischemia-induced MAP2 decline. It is plausible that MAP2 might be degraded and potentially released to the blood. Indeed, serum MAP2 elevation subjected to MCAO can be detected as early as 30 min, even before the appearance of visible infarction, indicating that serum MAP2 might serve as a biomarker for ischemia-induced neuronal damage.^{55,56} Besides MAP2, tauopathy has been identified in cerebral ischemia and recognized as vascular risk factors for AD. Previous data from our lab provides evidence that hyperphosphorylation of tau and neurofibrillary tangle (NFT)-like tauopathy can be induced after transient cerebral ischemia.^{37,57} The tau protein dysfunction after ischemia-reperfusion injury has been previously reviewed in detail.⁵⁸ Ischemic brain injury affects the tau modification at gene and protein level, leading to tau deposition, and the potential underlying mechanisms including autophagy, oxidative stress, apoptosis etc. give new insights to therapeutic

strategy of irreversible post-ischemic AD-type neurodegeneration.

2.2.2 Neurofilament (NF)

NF is the type-IV family of intermediate filament (IFs) in the CNS, consisting of NF-heavy, medium, light subunits (NFH, NFM, NFL), and α -internexin (INA), which is functionally interdependent from NF triplet proteins.⁵⁹ Unlike the other two cytoskeleton components, NF are more stable and set up cross-bridge with microfilaments or MTs to form dynamic cytoplasmic bundles or networks. NF phosphorylation plays an essential role in axon diameter and transport regulation, whereas aberrant NF alternation has been widely recognized in many neurodegenerative diseases.⁶⁰ Increasing evidence has indicated that NF-Light as a potential biomarker for axonal injury in cerebral ischemia/hypoperfusion, which further suggest the significant impact of vascular dysfunction in neuron degeneration.

NF is an ischemia-sensitive element of the neuronal cytoskeleton. The mRNA level of NFL, NFH and INA in the neocortex region dramatically decreased during the first 24-hours after focal cerebral ischemia.⁶¹ Similar transcriptional patterns and distinct immunofluorescence signaling of NFs are confirmed using different experimental focal cerebral ischemic models and human stroke samples.⁶² Increased NFL fluorescence intensity with down-regulated INA, NFM and NFH immunoreactivity was identified in the ischemic area. The up-regulated NFL further expanded to the penumbra region and colocalized with neuroprotective HSP70 positive area at 24-hour post-ischemia, suggesting that NFL alteration happens as an early event and tends to be a potential biomarker to identify salvageable tissue when subjected to ischemia.⁶² Additionally,

increased NFL degradation products of lower molecular weight with full length 69 kDa-NFL downregulation have been identified using polyclonal antibody in Western Blot, which is consistent with previous study showing reduced NFL immunoreactivity from the infarct region detected by monoclonal antibody.⁶³ Not only NFL expression levels altered, its staining pattern also changed from smooth, even distribution to a loose, bulb-like, disconnected deformation in axon, reflecting axonal functional and integrity impairment after cerebral ischemia.^{56,62,64,65} Ischemia-induced neuronal damage and blood-brain-barrier (BBB) dysfunction leads to the quick release of neuroaxonal markers (NFs) from disrupted axonal membrane to plasma and cerebrospinal fluid (CSF). Elevated NFL and phospho-NFH expression level in CSF and serum have been observed within the first 3 weeks in ischemic stroke patients.⁶⁶ Serum NFL elevation can be observed as early as 24 hours following ischemic stroke or TIA, and it can correlate with clinical severity on admission and functional outcomes at 3-month, indicating that serum NFL level might be a good indicator to differentiate TIA from ischemic stroke patients.^{67,68} Overall, NF-light is likely to represent a sensitive biomarker for early ischemia-induced axonal damage.

In the current study, we aimed to investigate if TIA can induce the neuronal cytoskeletal modification which might share the similar feature with AD pathology.

2.3 Neuroinflammation

Cerebral ischemia can trigger the acute injury phase, characterized as excitotoxicity, impaired ionic homeostasis, mitochondria dysfunction, edema and free radical formation.⁶⁹ The depletion of oxygen and glucose causes irreversible damage to

neural cells, and when ischemia persists long enough, it can induce neuronal death, forming an ischemic core and the surrounding hypoperfused penumbra region. Neural cells affected by the initial ischemic injury can trigger multiple cascades of secondary injury in the following hours to days after cerebral ischemia, which are predominately resulted from neuroinflammatory response.⁷⁰ Neuroinflammation plays a critical role in cerebral ischemia pathophysiology, especially in respect of reperfusion, and the blockage of neuroinflammation can dramatically reduce ischemic injury in experimental settings.⁷¹

Cerebral ischemia induces a robust neuroinflammatory response by danger-associated molecular patterns (DAMPs) release from injured brain regions. The immune cells can identify DAMPs through pattern recognition receptor and further triggers the intracellular signaling pathways.⁷² Among activated immune cells in the CNS, microglia are the first cell population to respond to these dangerous signaling. Within minutes following cerebral ischemia, microglia are activated and undergo morphological changes, secreting multiple cytokines. At the same time, astrocytes as the most abundant glia in CNS, are highly involved in the immune response and support the neuronal survival in the acute phase.⁷²

2.3.1 Microglia

Microglia are resident immune cells in the central nervous system, and it plays an essential role in neurogenesis, myelin turnover and dynamic synaptic remodeling through monitoring functional state of synapses.^{73,74} Microglia also represent the only population of macrophage-like cells in CNS parenchyma, and function in phagocytosis and

orchestrating inflammatory cascade in response to various neurological diseases.⁷⁵ Resident microglia are activated shortly and accumulated in the ischemic-affected core and penumbra regions following cerebral ischemia.⁷⁶ Upon activation, microglia can undergo morphological changes to decrease complexity of cellular processes and shift from a specific ramified phenotype termed 'resting microglia' to an amoeboid appearance termed 'activated microglia' with round cell body and short pseudopodia, which enable them to move quickly towards the affected region and perform immune response.⁷⁷ Activated microglia can exhibit phenotypic and functional diversity based on the strength and the duration of stimulator.⁷⁸ Traditionally, at least two activated phenotypes have been categorized: 'classical activated' (M1 type) and 'alternative activated' (M2 type). The M1 type microglia can release various proinflammatory cytokines (e.g., IL-1 β , TNF- α , nitrous oxide) which can induce neuroinflammation, neurotoxicity, and aggravate the brain infarction, meanwhile, the M2 type microglia can release various anti-inflammatory cytokines (e.g., IL-10, TGF- β) and neurotrophic factors (e.g., brain-derived neurotrophic factors/BDNF, vascular endothelial growth factor/VEGF), which can induce anti-inflammation, neuroprotection and improve stroke outcomes.⁷⁹ In addition to secreting pro- or anti-inflammatory cytokines, microglia activation can be characterized as high capacity for phagocytosis, which enable to remove apoptotic cells and debris following brain injury, especially in M2 microglia. Although there is no convincing evidence supporting microglial phagocytosis is beneficial or detrimental in tissue repair, it is true that microglia function as double-edged sword after cerebral ischemia, as its phenotypic distribution either in 'toxic' M1 or 'protective' M2 microglia is regulated by surrounding environment and changes along with the time.⁸⁰ The microglia phagocytosis can be

activated by various receptors expressed on the microglia surface, such as complement receptors, toll-like receptors, etc.⁸¹ Cerebral ischemia induces peripheral neutrophils and macrophages infiltration, as well as resident microglia activation.⁸² The activated microglia can rapidly migrate towards the infarction region and perform phagocytosis to clear cellular debris.⁸³ Interestingly, phagocytic activated microglia reached their peak number as early as 24 hours after reperfusion and persisted in the similar levels within the following few days, which provide evidence that microglia can elicit phagocytic response to mediate inflammation at the early stage even before peripheral macrophages infiltration.⁸⁴

2.3.2 Astrocyte

Astrocytes are the most numerous glia cell type within CNS and are critical for brain homeostasis, as astrocytes can provide regulatory role in neurogenesis, synaptogenesis, maintaining BBB permeability, and controlling extracellular balance of ions and neurotransmitters.⁸⁵ Astrocytes are also immune-competent glia which enable to receive danger signals and get respond through cytokines and chemokines release, leading to adaptive immune defense activation.⁸⁶ Brain injury induces an extensive glial response in terms of reactive gliosis, and eventually leading to scar formation surrounding affected region. Expression of the intermediate filament—glial fibrillary acidic protein (GFAP) is expressed not only in the progenitor cells of astrocyte, oligodendrocytes, and neurons, but also widely recognized as the identification of astrocytes *in vitro* and *in vivo*, and an increased expression of GFAP in astroglia is a hallmark for CNS pathology.^{85,87} The astrogliosis has been well studied in various animal models and human brain samples

following cerebral ischemia, especially ischemic stroke.^{88,89} Recent evidence show that the outcome of astrogliosis is time- and context-dependent, and astrogliosis can exert both beneficial and detrimental effects on the neural tissue repair after injury. Once CNS injury occurs, the astrocyte undergoes hypertrophy, migration, proliferation and functional modification determined by the distance from infarction and the severity of the injury. During this process, ependymal cells and NG2⁺ cells are highly involved in the progress of gliogenesis. The gliogenesis, together with astrocyte hypertrophy, leads to the astrocyte activation, then, the astrocytic activation, proliferation and migration coordinate and contribute to form the glia scar, which mediated via key molecules, such as TGF- β 1, matrix metalloproteinase (MMP9) etc.⁹⁰ At the acute phase following cerebral ischemia, glia scar formation is essential for confining the injury site to remodel the tissue, as well as spatial and temporal controlling local immune responses. The glial barrier enables to seal the lesion area, regulate extracellular matrix maintenance, prevent potential infections, limit inflammatory and growth factor cascade, and scavenge free radicals generation from injured tissue.⁹¹ The glial scar also contribute to revascularization which strengthen the nutritional, trophic, and metabolic support of the neural tissue. ⁹¹ On the other hand, the glia scar may prevent axonal regeneration and interfere with functional recovery by forming a physical and chemical (proteoglycans and tenascins) barrier during the chronic phase following cerebral ischemia.⁹² Therefore, modulating astrocyte activation and the underlying signal mechanisms may promote the neuronal functional recovery after CNS pathology, and they may be the potential therapeutic targets to get more attention and investigation.

Here, we focused on microglia and astrocytes in this project to investigate the effect of TIA on astrocyte and microglia activation.

3. Glucose metabolic regulation in brain function and diseases

During the neuronal cytoskeletal modification under pathological conditions, the cytoplasmic organelles orchestrate and coordinate each other to mediate compartmentalized signaling mechanism through transporting and regulating mitochondrial and glycolytic-related enzymes.⁹³ Glucose is the primary fuel for the brain, which accounts for around 20% of whole body glucose consumption.⁹⁴ Other alternative substrates including lactate, fatty acid and some amino acids can also be used for the brain in response to stress and high glucose consumption, such as fasting or prolonged exercise.⁹⁵ Glucose is primary responsible for fulfilling complicated neurological functions, including neuronal signaling transmission (synaptic signaling, action potential) and non-signaling activity (cytoskeletal remodeling, axonal transport). At the same time, glucose can provide carbon for the synthesis of biological molecules (amino acid, fatty acid), and glucose metabolites—NADPH, which has been considered to play an important role in antioxidant reaction.⁹⁶ Disturbances of brain glucose metabolism provides the pathophysiological basis for neurological disorders, especially during the early stage in cerebral ischemia, AD and PD.^{95,97} After cardiac arrest, reduced brain glucose metabolism has been observed in the cortical region as early as 2 hours and up to 5 weeks following return of spontaneous circulation (ROSC).⁹⁷⁻⁹⁹ From fluorodeoxyglucose (FDG)-positron emission tomography (PET), decreased glucose uptake in the infarct region with up-regulated glucose uptake in the peri-infarct region has been indicated at 2 hours after ischemic stroke, which may indicate the neural cells from peri-infarct region undergo

aerobic glycolysis to compensate and provide energy in response to cerebral ischemia.^{100,101} Additionally, glia cells have been highly involved in the glucose metabolism disruption after cerebral ischemia. Compared with neurons and astrocytes, microglia have a higher capacity to support energy needs through non-oxidative phosphorylation pathway in the peri-ischemic region.¹⁰² The penumbra region within hyper-glycolytic activity following cerebral ischemia has been reported to activate microglia and increase ROS production, leading to more severe brain injury, however, the inhibition of glycolytic key enzyme can suppress microglia activation and alleviate the ischemic outcomes.¹⁰³ Recent study further indicates that fractalkine receptor chemokine ligand 1 (CX3CL1) from microglia can mediate glucose metabolism to up-regulate anti-inflammation signaling and decrease ischemic brain injury via elevating oxidative phosphorylation and suppressing glycolysis.¹⁰⁴ During the recovery phase after oxygen-glucose-deprivation (OGD) in primary astrocyte, astrocytic energy metabolism to support survival and recovery predominantly exhibit an increased glucose mobilization through pentose-phosphate-pathway (PPP) and tricarboxylic acid (TCA) cycle.¹⁰⁵ Besides, following ischemic stroke, the elevation expression of monocarboxylate transporter 1 (MCT1) in oligodendrocytes has been observed in the myelinated axons-enriched per-infarct striatum region, which may redistribute energy substrate and up-regulate lactate release to satisfy neuronal needs in response to ischemic condition.¹⁰⁶ Overall, advanced methods for analyzing cell-type-specific or region-specific features of glucose metabolism, as well as a deeper exploration for the links between glucose metabolism and cerebral ischemia are warranted to facilitate the understanding of normal brain physiology and neuropathology of neurological diseases.

CHAPTER 1

Recurrent Transient Ischemic Attack Induces Neural Cytoskeleton Modification and Gliosis in an Experimental Model

SUMMARY: Transient ischemic attack (TIA) presents a high risk for subsequent stroke, Alzheimer's disease (AD) and related dementia (ADRD). However, the neuropathophysiology of TIA has been rarely studied. By evaluating recurrent TIA-induced neuropathological changes, our study aimed to explore the potential mechanisms underlying the contribution of TIA to ADRD. In the current study, we established a recurrent TIA model by three times 10-minute middle cerebral artery occlusion within a week in rat. Neither permanent neurological deficit nor apoptosis were observed following recurrent TIA. No increase of AD-related biomarkers was indicated after TIA, including increase of tau hyperphosphorylation and β -site APP cleaving enzyme 1 (BACE1). Neuronal cytoskeleton modification and neuroinflammation was found at 1, 3, and 7 days after recurrent TIA, evidenced by the reduction of microtubule-associated protein 2 (MAP2), elevation of neurofilament-light chain (NFL), and increase of glial fibrillary acidic protein (GFAP)-positive astrocytes and ionized calcium binding adaptor molecule 1 (Iba1)-positive microglia at the TIA-affected cerebral cortex and basal ganglion. Similar NFL, GFAP and Iba1 alteration was found in the white matter of corpus callosum. In summary, the current study demonstrated that recurrent TIA may trigger neuronal cytoskeleton change, astrogliosis and microgliosis without induction of cell death at the acute and subacute stage. Our study indicates that TIA-induced neuronal cytoskeleton modification and neuroinflammation may be involved in the vascular contribution to cognitive impairment and dementia.

Keywords: Transient ischemic attack; cytoskeleton; astrogliosis; microgliosis; neuroinflammation; white matter.

Translational Stroke Research, in press 2022

1. Introduction

Transient ischemic attack (TIA) was defined as an episode of rapid-onset and short-lasting focal neurological disorder attributed to focal ischemia of CNS without acute infarction. ¹ TIA usually occurs more than once with one-third of TIA patients having recurrent episodes, and recurrent TIA within 7 days are associated with a higher risk of severe stroke than after a single TIA. ³⁻⁵ Besides, white matter damage in TIA patients correlates with early cognitive decline ⁸ and TIA may significantly contribute to Alzheimer's disease (AD) pathology ⁷, supporting vascular contribution to AD and ADRD. ^{9,10} However, TIA has received little attention in the experimental research field compared with other types of stroke, and its pathophysiology have been rarely studied.

The traditional TIA definition was based on full resolution of neurological symptoms within 24 hours of onset. Nevertheless, full functional recovery does not necessary indicate absence of neuropathological changes at the CNS. Early MRI studies has shown infarct in 46 - 81% of classically diagnosed TIA patients. ^{11,12} Diffusion-weighted MRI (DWI) lesion are frequently observed in TIA patients. ¹ Furthermore, decreased fractional anisotropy has been found in TIA patients even without DWI lesion. ¹⁵ Functional MRI study has revealed a decreased resting-state network connectivity at 1-month after onset of TIA symptoms. ¹⁰⁷ In a rat experimental TIA model, cortical selective neuronal loss with congruent microglial activation have been observed without MRI lesion and necrosis. ²⁰ In a mouse TIA model, neuronal apoptosis and cerebral vasculature abnormalities has been found without DWI and T2-weighted MRI (T2WI) lesion in the brain. ²² These studies suggest that TIA may induces microstructure modification in the brain even without infarct. In the current study, we established a recurrent TIA model in rats and investigated the

neuropathological change after recurrent TIA with a focus on AD-related biomarkers, neuronal cytoskeleton, and gliosis.

2. Materials and methods

2.1 Animals.

Sprague Dawley male rats (3-month-old) were purchased from the Charles River Laboratories (Hollister, CA). All animals were kept in independent ventilating cages with access to laboratory chow and water ad libitum under a fixed 12:12 light-dark cycle. All animal procedures were reviewed and approved by the University of North Texas Health Science Center Institutional Animal Care and Use Committee.

2.2 Surgical procedure.

The ischemic stroke and TIA were induced by transient middle cerebral artery occlusion (MCAO) under 2.0% isoflurane anesthesia as previously described.¹⁰⁸ Body temperature was maintained at 36.5 to 37.5 °C with a thermostat-controlled heating blanket during the entire procedure. The internal carotid artery (ICA) was exposed, and a 4-0 monofilament nylon suture with a silicone-coated tip (Doccol Cooperation, MA) was introduced into the ICA lumen and gently advanced to the origin of the middle cerebral artery (MCA) until proper resistance was felt. The blood flow was restored by suture withdrawal from ICA and MCA for reperfusion after 75-min MCAO for ischemic stroke. For recurrent TIA, the MCA was occluded for 10 min and the procedure was repeated three times every other day (Day 0, 2, 4). For sham surgery, all physiological parameters remained the same as recurrent TIA group except that the suture was not introduced into the MCA. The rats were sacrificed at 1, 3, or 7 days after TIA for further analysis as described below.

2.3 Behavior test.

Rats (N=5-21 per group) underwent neurobehavioral tests to evaluate motor function. The Garcia behavioral assessments, the cylinder test and body weight measurements were performed at the same time of the day from 24 hours before surgery to the experimental end points by an investigator blinded to the experimental groups.

2.3.1 Garcia neurological test.

The Garcia score, ranging from 0 to 18, is a scale to evaluate neurological function based on different parameters including spontaneous activity, symmetry of movement and outstretch of limbs, circling behavior, climbing ability, body proprioception, and vibrissae touch.¹⁰⁹ The lower score indicates more severe neurological damage. The Garcia Neurological test was performed at 2-hour after first TIA or ischemic stroke and tested repeatedly every day.

2.3.2 Cylinder test.

The cylinder test was used to assess locomotor asymmetry after TIA or ischemic stroke. The rats were placed inside a tall, open-top cylinder, and the forelimb activity when rearing against the wall was observed. The number of impaired and unimpaired forelimb contacts was recorded and the percentage of impaired forelimb contacts in total contacts was calculated for each animal.¹¹⁰ A trial continued until a rat performs a minimum of 20 independent rears where they touch the walls of the cylinder using their forelimbs (around 5 min/animal). One trial was conducted during each testing period. Cylinder test was performed 24-hour before TIA or ischemic stroke and repeated every other day after TIA or ischemic stroke.

2.4 Sample preparation and Western blot analysis.

The rats were anesthetized using isoflurane inhalation and cardiac perfusion with ice-cold normal saline. Brains were immediately harvested and the cross section from Bregma +1 to -1 mm was sampled for Western blot analysis. The rest of the brain was fixed in 4% paraformaldehyde and processed for paraffin embedding.

For Western blot analysis collection, the neuroanatomical potential core of infarct predominantly supplied by MCA was further dissected into the cerebral cortex and basal ganglia region, the detailed identification of the core of the infarct has been well-accepted and used by us.¹¹¹ To ensure equal loading, protein concentration was determined using Pierce 660nm Protein assay reagent (Thermo Scientific). Protein was then be resolved on SDS gel and transferred to a nitrocellulose membrane. After blocking with milk, blots were incubated overnight with anticipated primary antibodies (**Table1**) at 4 °C followed by secondary antibody (Goat, Jackson Immunoresearch, West Grove, PA). Chemiluminescence signal was detected with Biospectrum 500 UVP imaging system. Protein band density was quantified by ImageJ (NIH, USA) and normalized to β -actin.

2.5 Immunohistochemistry and TUNEL Staining.

Coronal brain sections (7- μ m thick) were obtained from the cerebrum after fixation and paraffin embedding. For immunostaining, sections were blocked with 5% donkey serum and 0.2% Triton-X in Superblock Blocking BufferTM (Thermo Scientific, USA) for 1h at room temperature after de-paraffinization and antigen retrieval. Sections were then washed and incubated with primary antibodies (**Table 1**) at 4 °C overnight followed by 60-min incubation of Alexa Fluor conjugated secondary antibodies (Thermo Fisher Scientific, USA). The sections were mounted with ProLongTM Gold antifade reagent with DAPI (Invitrogen, USA). Z-stack microscopic images were obtained by Zeiss LSM 510 META

confocal microscope (Carl Zeiss, USA). Images were processed for maximum intensity Z-projection by ImageJ software (NIH, USA). To detect apoptotic cells, the fragmentation of genomic DNA was recognized by in situ staining of DNA ends with TdT-mediated dUTP nick end labeling (TUNEL; Progega, USA) following the manufacturer's instruction. Axio Observer Z1 fluorescent microscope (Carl Zeiss, USA) was used to detect FITC-labeled TUNEL stain.

2.6 Imaging analysis.

For fluorescence intensity analysis, microscopic images were taken using Image Xpress PICO system (Molecular Device, CA) or confocal microscope. Same threshold was applied to select target protein-positive staining and exclude background using ImageJ. Four or five regions of interests (ROIs) were randomly selected in the ipsi- and contralateral cortex and basal ganglia. The fluorescence intensity and positive area fraction were measured by analyzing mean gray value and area fraction. For soma and axon of tau fluorescence analysis, 18-25 neurons/animal were selected from 40x confocal images, the soma and axon region were manually selected and mean gray value was valued. In corpus callosum, four 40x confocal microscopic images were taken to measure mean density (mean gray value) and area fraction from ipsi- and contralateral side. For Iba1⁺ cell count analysis, four 40x confocal images were taken in affected areas and the total number of Iba1 & DAPI positive labeled cells were counted for each animal.

2.7 Data collection and statistics.

Data were depicted as mean \pm standard error of mean (SEM). When assessing functional performance in behavior tests, one-way ANOVA followed by Tukey's multiple comparison test or Kruskal-Wallis test followed by Dunn's multiple comparison test were

used for multiple groups comparison with one independent variable. Two-way ANOVA followed by Bonferroni's multiple comparison test was performed to compare groups with two independent variables. Paired t-test was used to determine the difference between the ipsilateral and contralateral side of the brain for Western blot and immunofluorescence imaging analysis. The α level was set at 0.05, and p-value < 0.05 was considered statistically significant. Statistical analyses were performed using Graph Pad Prism V.7.

3. Results

3.1 Establishment of recurrent TIAs model based on TIA definition

Previous studies have found that 12.5-min MCAO was a threshold for no infarction and 10-min MCAO is the optimal model for TIA in rats.^{23,28} In the current study, recurrent TIA was induced by 3 times 10-min MCAO every other day. Behavior assessments were performed every day for up to 7 days after the last TIA episode, and the brains were collected at 1, 3, or 7-day after the last TIA for further analysis on (PSD1/D5, PSD3/D7, PSD7/D11) (**Figure 1**). No neurological impairment was observed after recurrent TIA as compared to sham, evidenced by the Garcia neurological and cylinder tests. While ischemic stroke induced by 75-min MCAO as positive control exhibited severe neurological impairment (**Figure 2a, 2b**). However, recurrent TIAs significantly impacted body weight than sham. The rats temporarily lost 5.8% of baseline body weight for up to 3 days and gradually gained 5.2% of baseline at 7-day after recurrent TIAs, whereas ischemic stroke dramatically induced body weight loss around 19.7% of baseline for at least 7 days after reperfusion (**Figure 2c**). To confirm acute infarction and perform histochemical studies in recurrent TIA model, we further dissected and defined the brain

as potentially core of infarct exclusively supplied by MCA as described above (**Figure 3**). As predicted, 75-min MCAO induced extensive apoptosis in the MCA territory evidenced by TUNEL staining. There was very minimal apoptosis detected in the affected cerebral cortex and basal ganglia region on day-1, 3, 7 (PSD1,3,7) after recurrent TIA (**Figure 4a, 4b**).

3.2 BACE1 expression and vascular endothelial growth factor (VEGF) expression after recurrent TIA

We determined the effect of recurrent TIA on beta-secretase (BACE) and VEGF activation. Western blot analysis indicated that no significant difference of BACE1 expression was observed in the affected cerebral cortex and basal ganglia region at 3, and 7 days after recurrent TIA (**Figure 5a, 5b,5c**). Besides, there was no significant difference of VEGF expression in the cortex and basal ganglia on day 3 after recurrent TIA (**Figure 6a, 6b**). Representative immunofluorescence microscopy further confirmed that VEGF exhibited a similar expression pattern in the ipsilateral cortex and basal ganglia as compared the contralateral side on PSD3 after recurrent TIA (**Figure 6c**).

3.3 Neuronal cytoskeletal modification induced by recurrent TIA

We determined the effect of recurrent TIA on tau phosphorylation. Western blot analysis demonstrated significantly decreased total tau expression in the TIA affected basal ganglia, but not cortex, at 1 day after recurrent TIA. In addition, a significantly reduced expression of phospho-tau at Ser396 was observed in the frontoparietal cortex and basal ganglia on day 1 after recurrent TIA. The reduction of tau and phosph-tau seems recovered quickly and no significant difference in the level of tau and p-tau at Ser396 was found at 3 or 7 days after recurrent TIA (**Figure 7a, 7b, 7c**).

Immunohistochemistry and confocal microscopy confirmed the reduction of p-tau (Ser396) and total tau in the TIA-affected territory at 1 day after TIA (**Figure 8**). Quantitative analysis indicated a significant reduction of total tau in the ipsilateral basal ganglia, but not cortex, as compared with the contralateral side at 1 day after recurrent TIA (**Figure 9a**). Further analysis showed a significantly immunofluorescence intensity reduction in soma and axon, with no difference in soma/axon expression ratio in cerebral cortex at 1 day after recurrent TIA (**Figure 9b**). Immunohistochemistry of P-tau (Ser396) exhibited a significantly decreased fluorescence intensity in the affected cortex and basal ganglia region on day 1 after recurrent TIA (**Figure 10**). Similarly, significant reduction of phosphorylated tau at Ser202/Thr205 (AT8) was indicated in the cortex and basal ganglia at day 1, but not 3 and 7, after recurrent TIA evidenced by Western blot (**Figure 11**) and immunohistochemical analysis (**Figure 12**).

Western blot and quantitative analysis indicated a significant decrease of MAP2 in the ipsilateral cortex and basal ganglia at 1, 3, and 7 days after recurrent TIA as compared with the contralateral side (n=7) (**Figure 13a,13b**). Immunohistochemistry and confocal microscopy demonstrated a significant MAP2 loss in the soma and apical dendrites in the TIA-affected cortical and basal ganglia region on day-1, 3, and 7 after recurrent TIA (**Figure 14,15**). On the other hand, the frontoparietal cortex supplied by ACA showed no change in MAP2 immunoreactivity (**Figure 15**).

We further explored neurofilament-Light chain modulation after recurrent TIA. Western blot analysis demonstrated a significant increase of NFL expression in the TIA-affected basal ganglia as compared to the contralateral side at 3, but not 1 and 7, days after recurrent TIA (**Figure 16**). Confocal microscopy images demonstrated a significant

increase of NFL staining in the axon bundles at the ipsilateral basal ganglia at 3 days after recurrent TIA (**Figure 17**).

3.4 Recurrent TIA induces astrogliosis and microgliosis

Western blot analysis indicated a significant GFAP elevation in the ipsilateral cortex and basal ganglia as compared with the contralateral side at 1, 3, and 7 days after recurrent TIA (**Figure 18**). Immunohistochemistry and microscopy analysis indicated reactive astrogliosis in the TIA-affect cortical and basal ganglia region at 7 days after recurrent TIA, evidenced by the GFAP⁺ area fraction elevation (**Figure 19**). Confocal microscopy of Iba1 immunohistochemistry demonstrated active microglia phenotype in the TIA-affected cortical and basal ganglia regions, evidenced by the significant increase in Iba1⁺ area fraction and cell count at 7 days after recurrent TIA (**Figure 20**). The Iba1-positive microglia scatter in the contralateral cortical and basal ganglia regions with typical ramified morphology. On the other hand, large amount of Iba1-positive microglia congregates in the TIA-affected cortex and basal ganglia and display amoeboid morphology. Some Iba1-positive microglia juxtapose to each other with large and irregular nuclei (**Figure 19**).

3.5 White matter modification in response to recurrent TIA

We determined neuronal and glial cytoskeletal alteration in the corpus callosum at 7 days after recurrent TIA. Immunohistochemistry and confocal microscopy revealed increased NFL⁺ area fraction and mean intensity in the ipsilateral corpus callosum as compared with the contralateral corresponding region. In addition, there was a significant increase in area fraction for GFAP and Iba1 immunostaining in the ipsilateral corpus callosum with no difference in mean intensity as compared with the contralateral region.

No significant difference in Iba1⁺ cell count was observed in ipsilateral corpus callosum as compared with the contralateral region (**Figure 21,22**). Higher magnification confocal images of triple immunofluorescence labeling from NFL, GFAP, Iba1 or DAPI demonstrated neuronal and glial cytoskeletal interaction and network which potentially enable the modification in corpus callosum after recurrent TIAs (**Figure 23**). No significant change of myelin basic protein (MBP) in term of MBP⁺ area fraction and mean intensity was observed at 7 days after recurrent TIA (**Figure 24**).

4. Discussion

TIA used to be a symptomatic diagnosis disease characterized as reversible stroke-like neurological deficits. Recently, AHA/ASA council has revised the TIA definition from time-based to tissue-based as a transient episode of neurological dysfunction caused by focal brain, spinal cord or retinal ischemia without acute infarction.¹ Thus, three criteria should be met for an experimental TIA model based on the tissue-based definition: temporary blockage of a cerebral artery, an episode of neurological dysfunction, and no detected infarct lesion.²³ The rodent intraluminal suture MCAO model is the most frequently used and reliable experimental stroke model that revealed many aspects of ischemic stroke pathophysiology.²⁴⁻²⁶ Recently, ten minutes or shorter intraluminal suture MCAO has been used for TIA model in rats, which induces minimal apoptosis without T2WI lesion.^{28,29} In the current study, we introduced three times 10-minute MCAO in rats as a recurrent TIA model. The TIA rats circled to the lesion side immediately after waking up from the anesthesia and fully recovered quickly without any detected neurological deficit. Neither infarct, brain swollen, nor apoptosis was observed in the TIA-affected brain region at up to 1 week after recurrent TIA.

Vascular endothelial growth factor (VEGF) plays an important role in angiogenesis, neurogenesis, and vascular permeability, which has multiple effects associated with ischemic stroke ¹¹². It is demonstrated that VEGF expression upregulation has been observed following ischemic stroke in both rodents ¹¹³ and human samples ¹¹⁴, indicating the increased angiogenesis induced by cerebral ischemia. VEGF expression is closely related to blood-brain-barrier (BBB) leakage especially in the acute phase after ischemic stroke, and VEGF administration to rodent brain may promote the BBB leakage following ischemic stroke ¹¹⁵. In the present study, we observed no VEGF expression change at day-3 after recurrent TIA, which may provide evidence that no BBB dysfunction was induced by recurrent TIA in the acute phase.

Cerebrovascular changes often coexist with AD. Amyloid angiopathy frequently occurs in AD patients. ¹¹⁶ There is increasing evidence supporting vascular contribution to AD and ADRD. ^{9,10,117} Ischemic stroke, including TIA, is associated with high risk of AD and ADRD ^{118,119}. Our previous studies using experimental ischemic stroke models have demonstrated that ischemic stroke induces AD-like tauopathy and BACE1 activation, providing evidence that AD and vascular cognitive impairment/dementia, traditionally considered distinct clinical and pathophysiological entities, might share common features and converging pathogenic mechanisms. ^{36,37,120,121} We expected that recurrent TIA may increase BACE1 activation and tau phosphorylation without inducing infarct lesion. Instead, we observed a transient reduction of total tau and phospho-tau at multiple phosphorylation sites after TIA. No change of BACE1 expression was found after recurrent TIA. To our surprise, an early and persistent change of MAP2 was indicated after recurrent TIA.

The modification of neuronal cytoskeleton components, including tau, MAP2, and NFL have been extensively investigated in ischemic stroke. Diminished tau and MAP2 associated with NFL up-regulation in the ischemic lesion have been identified in experimental stroke model of permanent MCAO as well as human stroke cases.^{65,122} However, modification of neuronal cytoskeleton in response to TIA has not been explored. In the current study, we observed an early and lasting MAP2 reduction in the soma and apical dendrites at the affected cortical and basal ganglia regions after recurrent TIA. A transient reduction of total tau and increase of NFL at the basal ganglia was indicated at day 1 and 3 after recurrent TIA, respectively. We speculate that the differential modification of MAP2, tau, and NFL might be attributed to the different localization of these cytoskeleton components. MAP2 predominantly express in the soma and dendrites while tau is axon-specific or enriched.⁵⁶ NFL is located in larger caliber myelinated axons.¹²³ There is indication for differential vulnerability of axonal and dendritic microtubule components in response to ischemic stroke.⁴⁸ Microtubules in myelinated axons may be more stable than those in dendrites. At the CNS, axons are enwrapped by oligodendrocyte-produced myelin, which may provide metabolic substrates to fuel axon energy requirements¹²⁴. Tau is closely associated with myelin thickness¹²⁵ and downregulation of tau decrease myelin basal protein expression.¹²⁶ In the present study, no myelin damage was indicated after recurrent TIA evidenced by the absence of MBP loss at the corpus callosum. It is plausible that myelin could protect tau or NFL to make them less vulnerable than MAP2 in dendrite and soma during TIA.

Neuroinflammation characterized as activation of astrocyte and microglia has been recognized as a common feature of neurological disorders¹²⁷. In term of ischemic stroke,

peri-infarct astrocyte undergoes reactive astrogliosis to form compact glial scar which might protect the surrounding healthy brain from exposure to the toxic elements and cellular debris in the infarct area. On the other hand, it impedes axons regeneration beyond the glial scar, hence, hinder the recovery process.⁸⁵ In the current study, increased GFAP expression was observed in TIA-affected cortical and basal ganglia regions at 1, 3 and 7 days after recurrent TIA, suggesting an early and persistent astrogliosis induced by recurrent TIA. The reactive astrogliosis was confirmed by the enlargement of astrocyte and increase of GFAP intensity by immunohistochemistry. The TIA-induced astrogliosis is diffusive without formation of compact glia scar. Furthermore, diffusive microgliosis was observed in the TIA-affected regions at 7 days after recurrent TIA evidenced by immunohistochemistry of Iba1.

Microglia has been long believed to like other CNS glial cells with neuroectodermal origin. It is now firmly established that microglia are derived from myeloid progenitors belong to the immune system.¹²⁸ In the rodent and human brain, microglia turn over several times during a lifetime by coupling proliferation and apoptosis.¹²⁹ In the current study, we demonstrated that recurrent TIA may induce extensive microgliosis even without neuronal cell death. Interestingly, many of these amoeboid microglia congregate and juxtapose to each other in the TIA-affected cortical and basal ganglia regions with large and irregular nuclei. Some of the enlarged microglia seem even have 2 adjacent nuclei. It is likely that the TIA-induced microgliosis is mainly attributed to the activation and proliferation of endogenous brain parenchymal microglia.

White matter microstructure changes and damage has been found to be closely correlated with cognitive dysfunction in TIA patients.^{8,130} White matter change are also

common in all stages of AD patient evidenced by white matter hyperintensity.¹³¹ White matter hyperintensity has been proposed as a neuroimaging marker for TIA diagnosis¹³. White matter hyperintensity often involves more than one structure and different presentations of white matter hyperintensity may be associated with different neuropathological changes including myelin loss, axonal disruption, astrogliosis and microglia activation.¹⁴ We observed astrocyte and microglia activation at the corpus callosum after recurrent TIA, evidenced by the hypertrophic cell bodies and extend long, wide processes. Furthermore, our study indicates that recurrent TIA may induce axonal change in the white matter evidenced by the NFL elevation at the corpus callosum even without myelin loss. The cytoskeleton is essential for neuronal function that ensure the transmission of chemical and electrical signals between neurons.⁴¹ NFL is a primary component of neurofilament in the CNS. There is mounting evidence that increase of NFL in blood and cerebrospinal fluid might be a promising biomarker for axonal damage in various neurological disorders¹³². The increase of NFL at the basal ganglia and corpus callosum suggest potential axonal damage after recurrent TIA, which may further trigger astrocyte and microglia activation.

Ischemic preconditioning, a sublethal ischemia, can incite endogenous protective signaling against subsequent lethal ischemic stroke. Preconditioning can be triggered by stimuli even without serious cell damage¹³³. TIA might induce ischemic tolerance to subsequent severe ischemic stroke. An experimental study demonstrated that 5-minute ipsilateral TIA alleviates subsequent permanent ischemic stroke as compared with contralateral TIA in a rat MCAO model²⁹. It is still not clear whether ischemic preconditioning occurs after TIA in humans¹³⁴⁻¹³⁶. There is growing evidence that

microglia may play a critical role in ischemic preconditioning ¹³⁷. Indeed, microglia have complex roles that can both harm and protect the brain in physiological and pathological conditions ¹³⁸. It is plausible that TIA-induced neuroinflammation could be beneficial or detrimental depending on the nature, intensity, and duration of the ischemia.

In summary, the present study established a recurrent TIA model in rats based on the recent tissue-based TIA definition. Our study demonstrated that recurrent TIA induces neuronal cytoskeletal modification, astrogliosis and microgliosis in the TIA-affected cortical and basal ganglia regions and white matter of corpus callosum. Our study indicate that recurrent TIA may trigger neuronal cytoskeletal modification and neuroinflammation, which may potentially impair white matter and neural network, thus, contribute to the onset and progression of cognitive impairment and dementia. **(Figure 25)** Future studies focused on the effect of TIA on each cytoskeleton components, neuroinflammation, and neural network may elucidate the involvement of TIA in the vascular contribution to cognitive impairment and dementia.

CHAPTER 2

Characterizing Region-Specific Glucose Metabolic Profile of the Rodent Brain Using Seahorse XFe96 Analyzer

SUMMARY: The brain is highly complex with diverse structural characteristics in accordance with specific functions. Accordingly, differences in regional function, cellular compositions, and active metabolic pathways may link to differences in glucose metabolism at different brain regions. In the current study, we optimized an acute biopsy punching method and characterized region-specific glucose metabolism of rat and mouse brain by a Seahorse XFe96 analyzer. We demonstrated that 0.5 mm diameter tissue punches from 180- μ m thick brain sections allow metabolic measurements of anatomically defined brain structures using Seahorse XFe96 analyzer. Our result indicated that the cerebellum displays a more quiescent phenotype of glucose metabolism than cerebral cortex, basal ganglia, and hippocampus. In addition, the cerebellum has higher AMPK activation than other brain regions evidenced by the expression of pAMPK, upstream pLKB1, and downstream pACC. Furthermore, rodent brain has relatively low mitochondrial oxidative phosphorylation efficiency with up to 30% of respiration linked to proton leak. In summary, our study discovered region-specific glucose metabolic profile and relative high proton leak coupled respiration in the brain. Our study warrants future research on spatial mapping of the brain glucose metabolism in physiological and pathological conditions and exploring the mechanisms and significance of mitochondrial uncoupling in the brain.

Keywords: Brain, glucose, hippocampus, metabolism, respiration

J Cereb Blood Flow Metab. 2022;42(7):1259-1271. doi:10.1177/0271678X221077341

1. Introduction

The mammalian brain is the most expensive organ in terms of energy expenditure in the whole body with fine regulatory mechanisms to ensure adequate energy substrates supply in register with neuronal activity. The brain uses glucose as the primary fuel for energy production predominately through mitochondrial oxidative phosphorylation ¹³⁹. Nonetheless, glucose metabolism is not of homogeneity in the whole brain. The brain is highly complex with diverse structural characteristics in accordance with specific functions. Accordingly, differences in regional cellular compositions, axonal and dendritic density, neurotransmitter distribution, and active metabolic pathways, may link to difference in neuronal function and glucose metabolism for different brain regions ^{140,141}. A recent study using imaging mass spectrometry demonstrated that some of the glucose metabolism enzymes and ATP level vary dramatically cross the brain ¹⁴². Disruption of glucose metabolism forms the pathophysiological basis for many brain disorders ¹⁴³⁻¹⁴⁵. Therefore, the brain spatial metabolic signatures are of high relevance in our understanding of the normal brain physiology and neuropathology of neurological diseases.

Extracellular flux assay by the Seahorse XFe24 and XFe96 analyzers has provided a technique for simultaneous measurement of respiration and glycolysis in 24 and 96-well plates ¹⁴⁶. The dynamic measure of oxygen consumption rate (OCR) and extracellular acidification rate (ECAR) enables characterization of metabolic parameters in cultured cells and isolated mitochondria. However, the cultured cells do not recapitulate the complex neuron-glia interaction and extracellular matrix in the brain. The purified mitochondria from brain tissue provide neither intracellular or extracellular environment

nor spatial metabolic measurement due to the relatively large amount of tissue required for mitochondrial isolation. Recently, methods have been developed to assess respiration of acute tissue biopsy from anatomically defined rodent brain regions by the Seahorse XFe24 and XFe96 analyzers^{147-149,150}. In the current study, we modified the acute biopsy punching procedure and characterized region-specific glucose metabolic profile of rat and mouse brain by the Seahorse XFe96 analyzer.

2. Materials and methods

2.1 Animals.

Sprague Dawley male and female rats (3-month-old) were purchased from the Charles River Laboratories (Hollister, CA). C57BL/6J female mice (3-month-old) were purchased from the Jackson Laboratory (Bar Harbor, ME). All animals were kept in independent ventilating cages with access to laboratory chow and water ad libitum under a fixed 12:12 light-dark cycle. All animal procedures were reviewed and approved by the University of North Texas Health Science Center Institutional Animal Care and Use Committee and followed EU Directive 2010/63/EU Guide for the Care and Use of Laboratory Animals.

2.2 Preparation of acute brain slices.

Animals were anesthetized using isoflurane inhalation and brains were immediately removed and placed in ice-cold oxygenated artificial cerebrospinal fluid (aCSF; in mmol/L: 120 NaCl, 3.5 KCl, 1.3 CaCl₂, 1 MgCl₂, 0.4 KH₂PO₄, 5 HEPES, 10 D-glucose, pH 7.4). The aCSF was oxygenated by 95% O₂ with 5% CO₂ at least one-hour prior to brain dissection. Agarose (4%) was used to make gel block and brains were

super-glued to the block and then fixed to the tissue holder of a vibratome (VT1000S, Leica, Nussloch, Germany) filled with oxygenated ice-cold aCSF. Coronal and sagittal sections (180 μ m thickness) were obtained from cerebrum and cerebellum, respectively. The sections were transferred to a chamber containing aCSF with continuous oxygenation at room temperature.

2.3 Tissue punching and Seahorse XFe96 analysis.

Brain sections were transferred to a 60 mm cell culture dish containing oxygenated aCSF at room temperature. Reusable biopsy punch (0.5 mm or 0.75 mm diameter, World Precision Instrument, FL, USA) was used to obtain tissue punches from different regions of the cerebral and cerebellar sections under a Zeiss surgical microscope (Carl Zeiss, Germany). The punch was gently pressed overtop the area of interest in the brain section and the obtained tissue punch was immediately injected into a poly-L-lysine (Sigma-Aldrich, USA) coated XFe96 Cell Culture Microplate (Agilent Technologies, CA) based on pre-defined layout. Each well contained 180 μ l aCSF with 1.0 mM pyruvate solution as assay media. After loading the 96-well plate, punches were manually manipulated to position in the bottom center of each well. For each Seahorse assay, brain punches derived from the same animal were seeded in a 96-well plate with n=12 to 16 for each group. The XFe96 Cell Culture Microplate was then transferred to a non-CO₂ incubator at 37 °C for 30 min. During this period, 10X concentration of each drug for assay (prepared in aCSF) was loaded in each injection port (A, B, C, D) of the Seahorse XFe96 Assay sensor cartridge that had been hydrated overnight and exchanged for XF Calibrant solution 3 hours prior to assay initiation. The drug-filled sensor cartridge was inserted into the Seahorse XFe96 Analyzer (Agilent Technologies, CA) for calibration. Once the

calibration finished, the calibration plate was replaced by the tissue-containing microplate to initiate the assay.

Assay protocol contained 4-cycle measurement of OCR / ECAR baseline. Five to twelve cycles measurement was made after injection of oligomycin (Sigma Aldrich, USA), gboxin, or genipin (Cayman Chemical, MI, USA). Four cycles measurement was made after injection of carbonyl cyanide-4-(trifluoromethoxy) phenylhydrazone (FCCP) supplied with pyruvate (Sigma Aldrich, USA). Four cycles measure were finally made after injection of rotenone (EMD Millipore, Germany) / antimycin A (Sigma Aldrich, USA). Each cycle consists of 2-min mix, 1-min wait and 3-min measure period. All the concentrations indicated are final concentration in the well after injection.

2.4 Immunohistochemistry and confocal microscopy.

Young adult female rats were sacrificed by anesthesia and cardiac perfusion with ice-cold normal saline. The brains were harvested and fixed in 4% paraformaldehyde and processed for paraffin embedding. Coronal and sagittal brain sections (7- μ m thick) were obtained from the cerebrum and cerebellum, respectively, for immunostaining. Sections were blocked with 0.2% Triton-X in Superblock Blocking BufferTM (Thermo Scientific, USA) for 20 min at room temperature after de-paraffinization and antigen retrieval. Sections were then washed and incubated with primary antibodies (NeuN: Mouse mAb, 1:150 dilutions, catalog #MAB377, Millipore; GFAP, Rabbit mAb, 1:250 dilutions, catalog #12389, Cell Signaling Technology) at 4 °C overnight followed by 60-min incubation of Alexa Fluor conjugated secondary antibodies (Thermo Fisher Scientific, USA). The sections were mounted with ProLongTM Gold antifade reagent with DAPI (Invitrogen, USA). Z-stack microscopic images were obtained by Zeiss LSM 510 META confocal

microscope (Carl Zeiss, USA). Images were processed for maximum intensity Z-projection by ImageJ software (NIH, USA).

2.5 Western blots.

Young adult mice were euthanized and perfused with ice-cold normal saline. The cerebral cortex, hippocampus, and cerebellum were dissected and protein extractions were obtained for Western blots carried out as previously detailed ¹⁵¹, using following primary antibodies: β 3-Tubulin (D71G9) (Rabbit mAb, 1:1000 dilutions, catalog #5568, Cell Signaling Technology); Aldehyde dehydrogenase 1 family, member L1 (ALDH1L1, Rabbit Ab, 1:1000 dilutions, catalog #ab87117, Abcam); GFAP (D1F4Q) (Rabbit mAb, 1:1000 dilutions, catalog #12389, Cell Signaling Technology); GAPDH (Mouse mAb, 1:5000 dilutions, catalog #sc-3223, Santa Cruz Technology); Phospho-AMPK α (Thr172) (Rabbit mAb, 1:1000 dilutions, catalog #4188, Cell Signaling Technology); AMPK α (23A3) (Rabbit mAb, 1:1000 dilutions, catalog #2603, Cell Signaling Technology); Phospho-Acetyl-CoA Carboxylase (Ser79) (Rabbit Ab, 1:1000 dilutions, catalog #3661, Cell Signaling Technology); Acetyl-CoA Carboxylase (C83B10) (Rabbit Ab, 1:1000 dilutions, catalog #3676, Cell Signaling Technology); Phospho-LKB1 (Ser428) (C67A3) (Rabbit Ab, 1:1000 dilutions, catalog #3482, Cell Signaling Technology); LKB1 (D60C5F10) (Rabbit Ab, 1:1000 dilutions, catalog #13031, Cell Signaling Technology). The membrane was then incubated by HRP-conjugated secondary antibodies (The Jackson ImmunoResearch Laboratories). Chemiluminescence was detected with Biospectrum 500 UVP imaging system. Protein band density was quantified by ImageJ (NIH, USA) and normalized to GAPDH.

2.6 Data collection and statistical analysis.

The animal data reporting of the current study has followed the ARRIVE 2.0 guidelines¹⁵². Raw data of OCR and ECAR curve for each well were compiled with Agilent's Wave 2.6.0 software. Wells with detached or broken tissue punch observed after assay were excluded from analysis. The basal respiration was measured as OCR in the absence of mitochondria inhibitors. The residual OCR values and OCR reduction after oligomycin or gboxin injection was used as proton leak-linked respiration and ATP-production coupled respiration, respectively. The OCR measurement after FCCP / pyruvate injection without oligomycin treatment was used as maximal respiration. The difference between maximal OCR and basal OCR was considered as spare respiration capacity. OCR measurement after rotenone / antimycin A (Rot / AA) injection represented non-mitochondria respiration (Figure 1a). ECAR was used for measure of glycolysis rate. The baseline ECAR was obtained at the starting assay conditions, while the stressed ECAR was obtained in the presence of stressor mix (oligomycin + FCCP). The metabolic phenotype showed the baseline OCR / ECAR of punches, as well as the maximal OCR (obtained after FCCP injection) and ECAR (after oligomycin / FCCP injection). In each figure (panel), data were derived from the brain punches from the same animal and seeded in the same plate. Each experiment was repeated at least 3 times under the same condition from different animals.

Data adhering to normal distribution were depicted as mean \pm SD and non-normally distributed data were presented as median and interquartile range (being the 25th and 75th percentile) unless otherwise stated. The Shapiro-Wilk test was used to test for normality. Two-tailed Student *t*-tests or Mann-Whitney U test were used to identify any significant difference when comparing two groups. One-way ANOVA followed by Tukey's

multiple comparison test or Kruskal-Wallis test followed by Dunn's multiple comparison test were used for multiple groups comparison with one independent variable. The α level was set at 0.05 for all analyses, and p -value < 0.05 was considered statistically significance. Statistical analyses were performed using Graph Pad Prism V.7.

3. Results

3.1 Region-specific glucose metabolic profile of the young and old rat brain

To determine the glucose metabolism in the presence of native intracellular and extracellular environment in well-defined anatomical brain structure, we have optimized a method that enables dynamic metabolic function profiling by the Seahorse XFe96 analyzer using acute rat brain tissue biopsy punches modified from previously reports^{149,150}. We obtained tissue punches from different brain regions at frontoparietal cortex, basal ganglia, hippocampal CA1, dentate gyrus, and cerebellar cortex for metabolic analysis using a Seahorse XF96 analyzer (**Figure 26**).

We compared different size cerebral cortical and cerebellar punches of 0.5 and 0.75 mm in diameter to obtain reliable OCR measurements. We found that the OCR readings of the 0.5 mm diameter cortical and cerebellar punches were within the 20-200 pmol/min range recommended by the manufacturer. In addition, the cerebellum demonstrated a lower basal OCR as compared with the cerebral cortex (**Figure 27**).

We determined the glucose metabolism profile of cerebral cortical, basal ganglia, and cerebellar punches obtained from 3-month-old rats using Seahorse XF Cell Mito Stress Test. Inhibition of mitochondrial complex V by oligomycin has been found to attenuate the maximal OCR response to mitochondrial uncoupler FCCP¹⁵³. Thus, non-

oligomycin groups were included to obtain the maximal OCR rate. Consistently, we observed that cerebellar punches exhibited significantly lower basal OCR than cerebral cortical and basal ganglia punches. Data analysis further revealed that the cerebellum was significantly lower than cerebral cortex and basal ganglia in maximal respiration and non-mitochondria respiration (**Figure 28a, b**). Similarly, significantly lower basal and stressed ECAR were observed in the cerebellum as compared to basal ganglia and / or cerebral cortex (**Figure 28c,d**). Assessment of glucose metabolic phenotype indicated more energetic phenotypes for all groups in response to stress and that the cerebellum displays a more quiescent phenotype than cerebral cortex and basal ganglia evidenced by the lower glycolytic and aerobic activity at the cerebellum than the cerebral cortex and basal ganglia (**Figure 28e**).

We obtained tissue punches from hippocampal dentate gyrus, CA1, and cerebellum of 3-month-old rats for extracellular flux analysis in the same 96-well plate. Our results demonstrated that dentate gyrus exhibited basal OCR values similar to the cerebellum while the basal OCR of the CA1 was within the range of cerebral cortex and basal ganglia (**Figure 29a**). Data analysis further revealed that dentate gyrus and cerebellum were significantly lower than hippocampal CA1 in basal respiration and non-mitochondria respiration. No significant difference was observed in maximal respiration among CA1, dentate gyrus and cerebellum (**Figure 29b**). Dentate gyrus displayed similar basal ECAR as hippocampal CA1, while CA1 was significantly higher than the cerebellum and dentate gyrus in stressed ECAR (**Figure 29c, d**). Assessment of glucose metabolic phenotype indicated that the cerebellum had a quiescent phenotype as compared with hippocampal CA1 and dentate gyrus (**Figure 29e**).

We further determined metabolic phenotype in different brain regions of middle-aged rats. Tissue punches were obtained from cerebral cortex, basal ganglia, and cerebellum of 12-month-old rats, and glucose metabolism was assessed by Seahorse XF Cell Mito Stress test in the same 96-well plate. Consistently, the cerebellum displayed lower basal respiration and non-mitochondrial respiration than cerebral cortex and basal ganglia (**Figure 30a, b**). The cerebellum also displayed lower baseline and stressed ECAR as compared with cerebral cortex and basal ganglia (**Figure 30c, d**).

3.2 Region-specific glucose metabolic profile of the mouse brain

We conducted extracellular flux analysis in different brain regions from 3-month-old mice to explore the region-specific metabolic phenotype in young mouse brain. Consistently, the cerebellum displayed lower basal OCR and ECAR values compared to cerebral cortex and basal ganglia. The cerebellum was significantly lower than cerebral cortex and basal ganglia in basal respiration, maximal respiration, and non-mitochondrial respiration (**Figure 31a, b**). A significantly lower baseline and stressed ECAR was observed in the cerebellum as compared with cerebral cortex and basal ganglia (**Figure 31c, d**). Assessment of glucose metabolic phenotype indicated that the cerebellum displayed a more quiescent phenotype with lower glycolytic and aerobic activity than cerebral cortex and basal ganglia (**Figure 31e**).

In separate analysis, dentate gyrus exhibited similar basal respiration, maximal respiration as the cerebellum. Data analysis suggested that the cerebellum was significantly lower than hippocampal CA1 in basal, maximal respiration, and non-mitochondrial respiration, as well as significantly lower than dentate gyrus in maximal respiration and non-mitochondrial respiration (**Figure 32a,b**). No significant difference in

baseline and stressed ECAR was observed in the cerebellum as compared with CA1 and dentate gyrus (**Figure 32c,d**). Glucose metabolic phenotype assessment implicated a more glycolytic and aerobic activity for hippocampal CA1 as compared to dentate gyrus and cerebellum that both maintained a more quiescent phenotype (**Figure 32e**). Overall, the region-specific metabolic phenotype in cerebral cortex, basal ganglia, hippocampal CA1, dentate gyrus, and cerebellum displayed similar region-specific profile in rat and mouse.

3.3 Oxidative phosphorylation efficiency of mouse brain

We conducted titration experiments to select optimal concentrations of oligomycin on OCR. Oligomycin treatment induced a dose-dependent OCR reduction which reach plateau at 5 to 10 μM (**Figure 33a, b**). We further determined the ATP production and proton leak-linked respiration in the mouse brain using different concentrations of complex V inhibitors. Oligomycin and gboxin decreased OCR to similar levels in the cerebral cortex and cerebellum at 5 μM concentration. Increase of concentration of oligomycin and gboxin to 10 μM did not provide further inhibition of OCR (**Figure 33c, d, e, f**). Data analysis suggested that cerebral cortex has significant higher ATP production, proton leak-linked, and non-mitochondrial respiration than the cerebellum. Interestingly, ATP production-linked respiration is about 50% of the basal respiration in both cerebral cortex and cerebellum. Proton leak-linked respiration comprised up to 30% of basal respiration in the cerebral cortex and cerebellum (**Figure 33c, d, e, f**).

We determined the effect of uncoupling proteins (UCPs) inhibitor, genipin, on mitochondrial proton leak-linked respiration. Acute treatment of genipin at 50 and 100 μM significantly decreased proton leak coupled OCR with minimal effect on ATP production

coupled OCR (**Figure 34a, b, c**). In addition, chronic treatment of genipin at 100 and 150 μM in aCSF supplied with pyruvate for 60 min displayed a trend to attenuate the basal OCR and significant reduction of proton leak coupled OCR without impact on ATP production coupled respiration (**Figure 34d, e, f**).

3.4 Region-specific metabolic signaling in the mouse brain

We determined the cellular components in the brain punches of different brain regions. Immunohistochemistry and confocal microscopy of the corresponding punch area demonstrated distinct brain structures with different cellular composites (**Figure 35a, b, c**). We further identified the neuronal and astrocytic markers and major metabolic signaling expression in different brain regions of 3-month-old mice. Representative Western blots and quantitative analysis indicated a significantly higher neuronal marker of β 3-tubulin in cerebral cortex than hippocampus and cerebellum (**Figure 36a, d**). The expression of ALDH1L1, an astrocyte marker, was significantly higher in cerebral cortex than hippocampus (**Figure 36a, e**), while GFAP expression was higher in hippocampus and cerebellum than in cerebral cortex (**Figure 36a, f**). Activation of AMPK signaling was significantly higher in the cerebellum than in cerebral cortex and hippocampus evidenced by higher expression of phospho-AMPK α (**Figure 36b, g**), phospho-ACC (**Figure 36b, h**), and phospho-LKB1 (**Figure 36c, i**). These data indicated that cerebral cortex, hippocampus, and cerebellum displayed a diverse cellular composition and difference in activation of metabolic signaling.

4. Discussion

There are three important findings derived from the present study. First, we have optimized a method that enables metabolic function assessment of anatomically defined brain structures by the Seahorse XFe96 analyzer in adult rat and mouse. Second, the rodent brain has region-specific glucose metabolic profile that the cerebellum displays a more quiescent phenotype than cerebral cortex, basal ganglia, and hippocampus. Third, the rodent brain has relatively low mitochondrial oxidative phosphorylation efficiency with high proton leak-linked respiration.

The Seahorse XFe analyzers measure real-time oxygen consumption rate and extracellular acidification rate in a multi-well plate to provide a systemic view of metabolic function in term of basal respiration, ATP production, proton leak, maximal respiration, spare respiratory capacity, and non-mitochondrial respiration in cultured cells and ex-vivo tissue samples. By simultaneously assessing mitochondrial respiration and glycolysis under basal and stressed conditions, it also provides insight into the metabolic phenotype of cells and tissues. The Seahorse XFe analysis of acute brain punches with same thickness, diameter, and weight enables high-resolution spatial mapping of brain glucose metabolism in a relative intact brain microenvironment. In 24-well plate-based assay, 1 mm diameter tissue punches from 250 μm thick rat and mouse brain sections provide reproducible respiratory measurement using Seahorse XFe24 analyzer^{148,150}. In 96-well plate based assay, 0.5 and 0.75 mm diameter tissue punches from 220 μm rat brain sections seems are optimal for metabolic flux analysis¹⁴⁹. The height of micro-chamber of XFe96 cell culture microplates is 200 μm . We obtained tissue punches from 180 μm thick brain sections to avoid tissue damage by the compression of the microsensors during the assay. The small brain tissue punches and the using of the Seahorse XFe96

analyzer allow metabolic measurements of anatomically defined brain structures with sufficient sample size to compare metabolic phenotype of different brain regions in the same 96-well plate assay. Our study demonstrated that this method could be used to define glucose metabolic profile of different brain regions at high-resolution in mouse and rat.

Imaging mass spectrometry of mouse brain sections has demonstrated significant regional differences in glucose metabolism enzymes ¹⁴². The human cerebellum seems are unique in term of energy metabolism with lower metabolic rate for glucose than the cerebrum ¹⁵⁴. In addition, the human cerebellum displays dramatically lower aerobic glycolysis than the cerebral cortex ^{155,156}. In the current study, we consistently observed lower glucose metabolism in the cerebellum than in other brain regions of young and old rats as well as young adult mice. The low glucose metabolic phenotype in the cerebellum was evidenced by the low rate of basal respiration, maximal respiration, non-mitochondrial respiration, as well as glycolysis. The cerebellum displays a more quiescent glucose metabolic phenotype at baseline as compared with cerebral cortex, basal ganglia, and hippocampal CA1 region. The glucose metabolism at cerebral cortex, basal ganglia, and hippocampal CA1 region shift dramatically toward a higher energetic phenotype under stressed condition. The cerebellum have different energy budget distribution from the neocortex with majority of energy on the maintenance of resting potentials while action potentials account for only small part ¹⁵⁷. Our study indicated that the cerebellum has lower spare respiratory capacity than the cerebrum and that the quiescent state of glucose metabolism in the cerebellum has less transition toward active state upon stress.

The brain consists of heterogeneous cells and each cell type has distinct metabolic phenotype. The region-specific glucose metabolism might be due to the difference in cellular compositions of different brain regions. Oxidative phosphorylation is the main mechanism to power neuronal activity in the brain ¹⁵⁸. The cerebellum, although represents only ~10% of total brain mass, contains ~80% of the total brain neurons that are mostly organized in the densest granule layer ¹⁵⁹. Interestingly, the high neuron to glia ratio in the cerebellum is not associated with high glucose metabolism. The granule cells are the most numerous cell type in the cerebellum and dominate the energy use of the cerebellar cortex ¹⁵⁷. Our cerebellar punches contained molecular layer, Purkinje cell layer, and granular layer with granule cells as the predominant cell type. We speculated that the low metabolism rate at the cerebellum was mainly due to the granule cell. Indeed, a similar glucose metabolic profile was observed in the dentate gyrus as in the cerebellum in which granule cell is the principal cell type. The low glucose metabolism of the cerebellar granule cell might be attributed to their small cell body and less dendrites ¹⁶⁰. However, the low glucose metabolism of the cerebellar cortex with a large amount of neurons indicates that the cerebellum might have unique mechanism underlying its higher energy efficient than the cerebrum.

The brain is widely recognized as a highly oxidative organ with disproportionately high fraction of oxygen consumption ¹³⁹. The coupling of ATP synthesis and substrate oxidation in mitochondria is not complete as proton can return to mitochondrial matrix without producing ATP. The classic oxygen electrode experiments have been used since 1950s to determine mitochondrial bioenergetics function ¹⁶¹. The state 4 respiration evaluates the oxygen consumption rate of the mitochondrial respiratory chain

predominately due to a proton leak. The ratio of the state 3 and state 4, termed as respiratory control ratio, indicates the level of coupling between oxidation and phosphorylation process in the mitochondria ¹⁶¹. In the permeabilized adult mouse brain tissue, the respiratory control ratio, calculated as the ratio of the state 3 respiration after adding ADP and the state 4 after adding oligomycin, was around 7 in the cerebral cortex, indicating high mitochondrial oxidative phosphorylation efficiency of the brain ¹⁶². Nonetheless, the measurement of the state 3_{ADP} and state 4_{oligo} respiration may include non-mitochondrial respiration in the permeabilized brain tissue, thus, may not necessarily reflect the mitochondrial oxidative phosphorylation efficiency. In isolated mitochondria, the mitochondrial phosphate / oxygen ratio of rat brain has lower mitochondrial oxidative phosphorylation efficiency than that of heart and liver ¹⁶³. In the present study, we consistently observed high levels of OCR even after complex V inhibition by oligomycin in different brain regions. We suspected that the less OCR inhibition by oligomycin was potentially due to the low concentration at 5 μ M or short measurement period. We conducted a titration experiment to determine the dose dependent effect of oligomycin on OCR with 12-cycle measurement for 85 minutes. Consistently, we observed ~50% OCR reduction upon oligomycin treatment at the concentration of 5, 10, 20, and 50 μ M. Without oligomycin, no spontaneous OCR reduction was observed within 12-cycles measurement. However, the brain punches were less response to FCCP after 12-cycles measurement. In a separate experiment, oligomycin at 10 μ M did not provide further OCR reduction after up to 8-cycle measurements. We used another ATP synthase inhibitor, gboxin, to assess the ATP production and proton leak-linked respiration and similar results were observed.

Our results provide further evidence that brain glucose metabolism might be less efficient with substantial uncoupling.

Mitochondrial proton leak is mediated mainly through adenine nucleotide translocase and UCPs ¹⁶⁴. Inhibition of UCPs has been found to reduce OCR in cell cultures ^{165,166}. We determined the effect of UCPs inhibition on OCR in cerebral cortex punches. UCPs inhibition by genipin significantly decreased proton leak coupled respiration with minimal impact on ATP production coupled respiration, suggesting that the observed proton leak-linked respiration is partially mediated through UCPs in the brain.

The significance of unexpected mitochondrial proton leak in the brain is unclear. Expression of UCP-2 has been found in the brain to provide neuroprotective effect against ischemic insult ¹⁶⁷. Similarly, expression of human UCP-2 in the mitochondria of adult fly neurons increases proton leak-dependent state 4 respiration, decrease ROS production, and extend life span ¹⁶⁸. Thus, the mitochondrial proton leak-linked respiration might play important roles in the oxidative defense and survival of the brain cells. UCP1 is well known to be responsible for thermogenesis in brown adipose tissue and body temperature maintenance. There is increasing evidence that brain temperature is significantly higher than arterial blood and that increases in local brain temperature occur in response to various stressful and emotionally arousing environment stimuli although the source of the heat production is not clear ¹⁶⁹⁻¹⁷³. The global distribution of UCP2/4/5 in the brain and their abilities to decrease mitochondrial membrane potential in neurons imply that neuronal UCPs activation may lead to heat generation ^{174,175}. We speculated that the high proton leak may be coupled to heat production and high temperature in the brain.

We expected that the differences in regional glucose metabolism identified by the Seahorse analysis might be associated with different activation of metabolic pathways. AMPK is an evolutionarily conserved energy sensor and regulator for energy metabolism¹⁷⁶. In mammalian adult brain, AMPKs are mainly expressed and constitutively active in neurons, with AMPK α 2 as the predominant catalytic subunit¹⁷⁷. AMPK is phosphorylated, hence, activated by two main mammalian upstream kinases: LKB1 and CaMKK β ¹⁷⁸. LKB1 activates AMPK α 2 but not AMPK α 1¹⁷⁹⁻¹⁸¹. We observed different activation of AMPK signaling in different brain regions. The lowest glucose metabolism in the cerebellum is associated with the highest AMPK activation than other brain regions evidenced by the expression of pAMPK, upstream pLKB1, and downstream pACC. AMPK is activated by events that either compromise cellular ATP production or increase ATP consumption^{176,182}. The high AMPK activation, together with the low rate of basal respiration, maximal respiration, and non-mitochondrial respiration in the cerebellum, indicated that the cerebellum has unique glucose metabolic phenotype as compared with other brain regions.

In summary, the present study determined the region-specific glucose metabolic profile of rodent brain using acute biopsy punches and Seahorse XFe96 analyzer. The metabolic flux analysis indicated that the cerebellum has a more quiescent phenotype of glucose metabolism as compared with the cerebrum. In addition, glucose metabolism might be less efficient in the brain than we expected, with relatively low ATP production-linked respiration with large component of proton leak-linked respiration. Our study warrants future research on spatial mapping of the brain glucose metabolism in

physiological and pathological conditions and exploring the potential mechanisms and significance of mitochondrial uncoupling in the brain.

DISCUSSION AND FUTURE DIRECTION

1. Recurrent TIA induces neuronal cytoskeleton change and gliosis

TIA is symptomatic diagnosis diseases and as a 'warning sign' for severe stroke. The incidence of TIA is estimated 200,000 to 500,000 per year and 15% of stroke patients have reported experiencing TIA before, which indicates that TIA incidence might be much higher.² It is likely that the incidence of TIA has been underestimated since most of the individuals who suffer from TIA don't seek for medical attention because the function gets back to normal quickly before getting medical evaluation. However, the importance of early diagnosis and treatment cannot be underestimated. The rapid intervention following TIA can prevent cerebrovascular damage and recurrence episodes of TIA and avoiding risk factors such as smoking, hypertension or high-fat diet can also help to reduce the risk of subsequent cerebral vascular event. Thus, it is of vital importance to understand the pathophysiology of TIA and explore the useful diagnostic biomarkers to confirm or rule out TIA in clinical practice. Current study has established a recurrent TIA model in rats based on the TIA definition. Unlike ischemic stroke which can induce AD-like biomarkers expression, recurrent TIA doesn't induce BACE1 activation and hyperphosphorylation of tau. Our study indicate that recurrent TIA can trigger neuronal cytoskeletal modification, neuroinflammation including astrogliosis and microgliosis in TIA-affected cortical and basal ganglia region, as well as in corpus callosum in the acute and subacute phase, which may potentially lead to white matter and neural network impairment, and further contribute to cognitive impairment and dementia in the future.

We observed the pathological changes as described above at the acute and subacute phase following recurrent TIA, future studies focus on chronic phase such as one-month after recurrent TIA to detect the TIA neuropathology might be further explored. Increasing evidence shows rapid elevated expression of GFAP or NFL in serum as promising prognosis biomarkers have been observed in various neurological diseases such as traumatic brain injury (TBI), ischemic stroke ^{183,184}. Future studies focus on these TIA-induced neuronal and glial cytoskeletal modulation not only in brain, but also in serum and CSF will give us more insights in the potential preventative and therapeutic strategy for transient ischemic insult. In the current study, 3-month-old young male rats were used, female and middle aged or older animals should be included in the next step considering the critical role of estrogen and age as risk factors in cerebral ischemia. ^{3,185} To apply our recurrent TIA model in the cognitive impairment and dementia for the long-term goal, learning and cognitive function assessment such as water maze test should be included. We observed the neural microstructure alteration in white matter, in terms of corpus callosum in the current study. To measure the white matter functional changes and neural network connectivity following recurrent TIA, in-vivo measurement of electroencephalogram (EEG) to record brain activity can be applied. Besides, T2 weighted MRI to monitor white matter hyperintensity in the acute, subacute or chronic phase after TIA especially abnormal myelination can be included. Additionally, a detailed mechanism underlying TIA-induced microgliosis and the neuroinflammatory responses mediated by activated microglia can be further investigated.

MAPs can regulate microtubule-binding affinity by phosphorylation, mediated by the balance of phosphatase and kinase activity. Under the pathological condition, the

equilibrium of phosphorylation-mediated MAPs binding affinity can be disrupted, leading to microtubule destabilization.⁴⁵ During this process, glycogen synthase kinase-3 β (GSK-3 β) and mitogen-activated protein kinases (MAPK) are primarily responsible for MAPs phosphorylation to regulate MT dynamic, functioning in axonal or dendritic outgrowth and remodeling.¹⁸⁶ There are other protein kinases, such as cAMP-dependent protein kinase (PKA), calmodulin-dependent protein kinase II (CAMKII), cyclin-dependent kinase 5 (CDK5), phospholipid-dependent protein kinase C (PKC), MAPK, all of which are participating in modulating cytoskeleton-mediated neuronal development and plasticity.¹⁸⁷ NFs phosphorylation is the most common PTMs to regulate NF behaviors. PKA, PKC, and CAMKII are involved in NF phosphorylation on head terminal domain in soma, which mediate NFs assembly and inhibit tail terminal phosphorylation to prevent pathological NF aggregation to be exported to axons.⁶⁰ GSK3, CDK5, MAPKs can modulate NF tail domain phosphorylation in axons to regulate spacing between polymers when subjected to stress or growth factor stimulus.¹⁸⁸ Future research focused on the effect of TIA on each cytoskeleton components and the underlying mechanism such as post-translational-modification (PTMs) may elucidate the involvement of TIA in the vascular contribution to cognitive impairment and dementia.

2. Region-specific metabolic profile of the brain

Neuronal cytoskeletal architecture and remodeling under pathological conditions requires the recruitment and coordination of cytoplasmic organelles, especially for mitochondria and glycolytic enzymes transport to regulate compartmentalized signaling mechanism⁹³. The brain glucose metabolism disruption provides the pathophysiological basis for various neurological diseases.¹⁴³ Thus, understanding the brain metabolic

signatures in normal brain are of high relevance in exploring the brain physiology and giving clues to investigate the neuropathology of neurological diseases. Our study aimed to establish and optimize an 'ex vivo' method which enables to monitor the dynamic metabolic profile including the mitochondria and glycolytic activity and apply it to different brain regions in normal brain, as well as under pathological condition in the future.

Current optimized method has successfully discovered region-specific glucose metabolic profile and relative high proton leak coupled respiration in the rodent brain which is partially mediated by uncoupling protein (UCP1). Future studies focus on spatial mapping of the brain glucose metabolism in pathological conditions, especially following transient ischemic insult may be explored, which provide the insights in TIA neuropathology. Both male and female rodents have been used for our study and no sex difference was indicated in non-mitochondria, basal or maximal respiration, as well as in ECAR, however, the effect of sex hormone on glucose metabolism can be further investigated based on our well-established platform. Although glucose has been considered as the primary fuel for brain metabolism, there are some minor oxidative substrates for brain including fatty acid and some amino acids, which contribute to the characterization of metabolic compartmentation in the brain.¹³⁹ Based on our optimized protocol, by incubating acute brain punches under various glucose availability and supplying with different substrates (fatty acid, amino acid etc.), we can further develop our method to determine the brain ability to utilize different fuel substrates from different brain regions. Thus, future direction will focus on characterizing region-specific complicated metabolic function in rodent brains beyond measuring glucose-dependent OCR. Besides, our study warrants future research on exploring the potential mechanisms

and significance of mitochondrial uncoupling in the brain in physiological and pathological conditions.

BIBLIOGRAPHY

1. Easton JD, Saver JL, Albers GW, Alberts MJ, Chaturvedi S, Feldmann E, Hatsukami TS, Higashida RT, Johnston SC, Kidwell CS, et al. Definition and evaluation of transient ischemic attack: a scientific statement for healthcare professionals from the American Heart Association/American Stroke Association Stroke Council; Council on Cardiovascular Surgery and Anesthesia; Council on Cardiovascular Radiology and Intervention; Council on Cardiovascular Nursing; and the Interdisciplinary Council on Peripheral Vascular Disease. The American Academy of Neurology affirms the value of this statement as an educational tool for neurologists. *Stroke*. 2009;40:2276-2293. doi: 10.1161/STROKEAHA.108.192218
2. Fisher M. Stroke and TIA: epidemiology, risk factors, and the need for early intervention. *Am J Manag Care*. 2008;14:S204-211.
3. Khare S. Risk factors of transient ischemic attack: An overview. *J Midlife Health*. 2016;7:2-7. doi: 10.4103/0976-7800.179166
4. Walz ET, Brink T, Slivka A. Pattern and frequency of recurrent transient ischemic attacks. *J Stroke Cerebrovasc Dis*. 1997;6:121-124. doi: 10.1016/s1052-3057(97)80227-3
5. Purroy F, Jimenez Caballero PE, Gorospe A, Torres MJ, Alvarez-Sabin J, Santamarina E, Martinez-Sanchez P, Canovas D, Freijo MJ, Egido JA, et al. Recurrent transient ischaemic attack and early risk of stroke: data from the

- PROMAPA study. *J Neurol Neurosurg Psychiatry*. 2013;84:596-603. doi: 10.1136/jnnp-2012-304005
6. Mok VCT, Lam BYK, Wang Z, Liu W, Au L, Leung EYL, Chen S, Yang J, Chu WCW, Lau AYL, et al. Delayed-onset dementia after stroke or transient ischemic attack. *Alzheimers Dement*. 2016;12:1167-1176. doi: 10.1016/j.jalz.2016.05.007
 7. Kalaria RN, Akinyemi R, Ihara M. Does vascular pathology contribute to Alzheimer changes? *J Neurol Sci*. 2012;322:141-147. doi: 10.1016/j.jns.2012.07.032
 8. Zamboni G, Griffanti L, Jenkinson M, Mazzucco S, Li L, Kuker W, Pendlebury ST, Rothwell PM, Oxford Vascular S. White Matter Imaging Correlates of Early Cognitive Impairment Detected by the Montreal Cognitive Assessment After Transient Ischemic Attack and Minor Stroke. *Stroke*. 2017;48:1539-1547. doi: 10.1161/STROKEAHA.116.016044
 9. Gorelick PB, Scuteri A, Black SE, Decarli C, Greenberg SM, Iadecola C, Launer LJ, Laurent S, Lopez OL, Nyenhuis D, et al. Vascular contributions to cognitive impairment and dementia: a statement for healthcare professionals from the american heart association/american stroke association. *Stroke*. 2011;42:2672-2713. doi: 10.1161/STR.0b013e3182299496
 10. Goulay R, Mena Romo L, Hol EM, Dijkhuizen RM. From Stroke to Dementia: a Comprehensive Review Exposing Tight Interactions Between Stroke and Amyloid-beta Formation. *Transl Stroke Res*. 2020;11:601-614. doi: 10.1007/s12975-019-00755-2

11. Fazekas F, Fazekas G, Schmidt R, Kapeller P, Offenbacher H. Magnetic resonance imaging correlates of transient cerebral ischemic attacks. *Stroke*. 1996;27:607-611. doi: 10.1161/01.str.27.4.607
12. Bhadelia RA, Anderson M, Polak JF, Manolio TA, Beauchamp N, Knepper L, O'Leary DH. Prevalence and associations of MRI-demonstrated brain infarcts in elderly subjects with a history of transient ischemic attack. The Cardiovascular Health Study. *Stroke*. 1999;30:383-388. doi: 10.1161/01.str.30.2.383
13. Nagy M, Azeem MU, Soliman Y, Nawab SA, Jun-O'Connell AH, Goddeau RP, Jr., Moonis M, Silver B, Henninger N. Pre-existing White Matter Hyperintensity Lesion Burden and Diagnostic Certainty of Transient Ischemic Attack. *J Stroke Cerebrovasc Dis*. 2019;28:944-953. doi: 10.1016/j.jstrokecerebrovasdis.2018.12.022
14. Alber J, Alladi S, Bae HJ, Barton DA, Beckett LA, Bell JM, Berman SE, Biessels GJ, Black SE, Bos I, et al. White matter hyperintensities in vascular contributions to cognitive impairment and dementia (VCID): Knowledge gaps and opportunities. *Alzheimers Dement (N Y)*. 2019;5:107-117. doi: 10.1016/j.trci.2019.02.001
15. Ferris JK, Edwards JD, Ma JA, Boyd LA. Changes to white matter microstructure in transient ischemic attack: A longitudinal diffusion tensor imaging study. *Hum Brain Mapp*. 2017;38:5795-5803. doi: 10.1002/hbm.23768
16. Li R, Wang S, Zhu L, Guo J, Zeng L, Gong Q, He L, Chen H. Aberrant functional connectivity of resting state networks in transient ischemic attack. *PLoS One*. 2013;8:e71009. doi: 10.1371/journal.pone.0071009

17. Guo J, Chen N, Li R, Wu Q, Chen H, Gong Q, He L. Regional homogeneity abnormalities in patients with transient ischaemic attack: a resting-state fMRI study. *Clin Neurophysiol.* 2014;125:520-525. doi: 10.1016/j.clinph.2013.08.010
18. Bentes C, Canhao P, Peralta AR, Viana P, Fonseca AC, Geraldes R, Pinho EMT, Paiva T, Ferro JM. Usefulness of EEG for the differential diagnosis of possible transient ischemic attack. *Clin Neurophysiol Pract.* 2018;3:11-19. doi: 10.1016/j.cnp.2017.10.001
19. Serlin Y, Ofer J, Ben-Arie G, Veksler R, Ifergane G, Shelef I, Minuk J, Horev A, Friedman A. Blood-Brain Barrier Leakage: A New Biomarker in Transient Ischemic Attacks. *Stroke.* 2019;50:1266-1269. doi: 10.1161/STROKEAHA.119.025247
20. Ejaz S, Emmrich JV, Sawiak SJ, Williamson DJ, Baron JC. Cortical selective neuronal loss, impaired behavior, and normal magnetic resonance imaging in a new rat model of true transient ischemic attacks. *Stroke.* 2015;46:1084-1092. doi: 10.1161/STROKEAHA.114.007581
21. Liu YH, Liao LD, Tan SSH, Kwon KY, Ling JM, Bandla A, Shih YI, Tan ETW, Li W, Ng WH, et al. Assessment of neurovascular dynamics during transient ischemic attack by the novel integration of micro-electrocorticography electrode array with functional photoacoustic microscopy. *Neurobiol Dis.* 2015;82:455-465. doi: 10.1016/j.nbd.2015.06.019
22. Wang J, Li Y, Yu H, Li G, Bai S, Chen S, Zhang P, Tang Z. DI-3-N-Butylphthalide Promotes Angiogenesis in an Optimized Model of Transient Ischemic Attack in C57BL/6 Mice. *Front Pharmacol.* 2021;12:751397. doi: 10.3389/fphar.2021.751397

23. Wang J, Zhang P, Tang Z. Animal models of transient ischemic attack: a review. *Acta Neurol Belg.* 2020;120:267-275. doi: 10.1007/s13760-020-01295-5
24. Liu F, McCullough LD. Middle cerebral artery occlusion model in rodents: methods and potential pitfalls. *J Biomed Biotechnol.* 2011;2011:464701. doi: 10.1155/2011/464701
25. Bonnin P, Kubis N, Charriaut-Marlangue C. Collateral Supply in Preclinical Cerebral Stroke Models. *Transl Stroke Res.* 2021. doi: 10.1007/s12975-021-00969-3
26. Wolf VL, Ergul A. Progress and challenges in preclinical stroke recovery research. *Brain Circ.* 2021;7:230-240. doi: 10.4103/bc.bc_33_21
27. Pedrono E, Durukan A, Strbian D, Marinkovic I, Shekhar S, Pitkonen M, Abo-Ramadan U, Tatlisumak T. An optimized mouse model for transient ischemic attack. *J Neuropathol Exp Neurol.* 2010;69:188-195. doi: 10.1097/NEN.0b013e3181cd331c
28. Durukan Tolvanen A, Tatlisumak E, Pedrono E, Abo-Ramadan U, Tatlisumak T. TIA model is attainable in Wistar rats by intraluminal occlusion of the MCA for 10min or shorter. *Brain Res.* 2017;1663:166-173. doi: 10.1016/j.brainres.2017.03.010
29. Fan C, Zhang L, He Z, Shao P, Ding L, Wang G, Niu W, Jia J. Reduced Severity of Outcome of Recurrent Ipsilateral Transient Cerebral Ischemia Compared with Contralateral Transient Cerebral Ischemia in Rats. *J Stroke Cerebrovasc Dis.* 2017;26:2915-2925. doi: 10.1016/j.jstrokecerebrovasdis.2017.07.035

30. McKhann G, Drachman D, Folstein M, Katzman R, Price D, Stadlan EM. Clinical diagnosis of Alzheimer's disease: report of the NINCDS-ADRDA Work Group under the auspices of Department of Health and Human Services Task Force on Alzheimer's Disease. *Neurology*. 1984;34:939-944. doi: 10.1212/wnl.34.7.939
31. de la Torre JC. Alzheimer disease as a vascular disorder: nosological evidence. *Stroke*. 2002;33:1152-1162. doi: 10.1161/01.str.0000014421.15948.67
32. Rapoport SI. Functional brain imaging to identify affected subjects genetically at risk for Alzheimer's disease. *Proc Natl Acad Sci U S A*. 2000;97:5696-5698. doi: 10.1073/pnas.120178897
33. Lee BC, Mintun M, Buckner RL, Morris JC. Imaging of Alzheimer's disease. *J Neuroimaging*. 2003;13:199-214.
34. Snowdon DA, Nun S. Healthy aging and dementia: findings from the Nun Study. *Ann Intern Med*. 2003;139:450-454. doi: 10.7326/0003-4819-139-5_part_2-200309021-00014
35. Zlokovic BV. Neurovascular pathways to neurodegeneration in Alzheimer's disease and other disorders. *Nat Rev Neurosci*. 2011;12:723-738. doi: 10.1038/nrn3114
36. Wen Y, Onyewuchi O, Yang S, Liu R, Simpkins JW. Increased beta-secretase activity and expression in rats following transient cerebral ischemia. *Brain Res*. 2004;1009:1-8. doi: 10.1016/j.brainres.2003.09.086
37. Wen Y, Yang S, Liu R, Simpkins JW. Transient cerebral ischemia induces site-specific hyperphosphorylation of tau protein. *Brain Res*. 2004;1022:30-38. doi: 10.1016/j.brainres.2004.05.106

38. Witte H, Bradke F. The role of the cytoskeleton during neuronal polarization. *Curr Opin Neurobiol.* 2008;18:479-487. doi: 10.1016/j.conb.2008.09.019
39. Menon S, Gupton SL. Building Blocks of Functioning Brain: Cytoskeletal Dynamics in Neuronal Development. *Int Rev Cell Mol Biol.* 2016;322:183-245. doi: 10.1016/bs.ircmb.2015.10.002
40. Blanquie O, Bradke F. Cytoskeleton dynamics in axon regeneration. *Curr Opin Neurobiol.* 2018;51:60-69. doi: 10.1016/j.conb.2018.02.024
41. Munoz-Lasso DC, Roma-Mateo C, Pallardo FV, Gonzalez-Cabo P. Much More Than a Scaffold: Cytoskeletal Proteins in Neurological Disorders. *Cells.* 2020;9. doi: 10.3390/cells9020358
42. Brown CE, Wong C, Murphy TH. Rapid morphologic plasticity of peri-infarct dendritic spines after focal ischemic stroke. *Stroke.* 2008;39:1286-1291. doi: 10.1161/STROKEAHA.107.498238
43. Zhang S, Boyd J, Delaney K, Murphy TH. Rapid reversible changes in dendritic spine structure in vivo gated by the degree of ischemia. *J Neurosci.* 2005;25:5333-5338. doi: 10.1523/JNEUROSCI.1085-05.2005
44. Hinman JD. The back and forth of axonal injury and repair after stroke. *Curr Opin Neurol.* 2014;27:615-623. doi: 10.1097/WCO.0000000000000149
45. Dehmelt L, Halpain S. The MAP2/Tau family of microtubule-associated proteins. *Genome Biol.* 2005;6:204. doi: 10.1186/gb-2004-6-1-204
46. Gao YL, Wang N, Sun FR, Cao XP, Zhang W, Yu JT. Tau in neurodegenerative disease. *Ann Transl Med.* 2018;6:175. doi: 10.21037/atm.2018.04.23

47. Matesic DF, Lin RC. Microtubule-associated protein 2 as an early indicator of ischemia-induced neurodegeneration in the gerbil forebrain. *J Neurochem.* 1994;63:1012-1020. doi: 10.1046/j.1471-4159.1994.63031012.x
48. Yanagihara T, Brengman JM, Mushynski WE. Differential vulnerability of microtubule components in cerebral ischemia. *Acta Neuropathol.* 1990;80:499-505. doi: 10.1007/BF00294610
49. Kwei S, Jiang C, Haddad GG. Acute anoxia-induced alterations in MAP2 immunoreactivity and neuronal morphology in rat hippocampus. *Brain Res.* 1993;620:203-210. doi: 10.1016/0006-8993(93)90157-i
50. Ota A, Ikeda T, Ikenoue T, Toshimori K. Sequence of neuronal responses assessed by immunohistochemistry in the newborn rat brain after hypoxia-ischemia. *Am J Obstet Gynecol.* 1997;177:519-526. doi: 10.1016/s0002-9378(97)70139-x
51. Kharlamov A, LaVerde GC, Nemoto EM, Jungreis CA, Yushmanov VE, Jones SC, Boada FE. MAP2 immunostaining in thick sections for early ischemic stroke infarct volume in non-human primate brain. *J Neurosci Methods.* 2009;182:205-210. doi: 10.1016/j.jneumeth.2009.06.014
52. Kuhn J, Meissner C, Oehmichen M. Microtubule-associated protein 2 (MAP2)--a promising approach to diagnosis of forensic types of hypoxia-ischemia. *Acta Neuropathol.* 2005;110:579-586. doi: 10.1007/s00401-005-1090-9
53. Popp A, Jaenisch N, Witte OW, Frahm C. Identification of ischemic regions in a rat model of stroke. *PLoS One.* 2009;4:e4764. doi: 10.1371/journal.pone.0004764

54. Buddle M, Eberhardt E, Ciminello LH, Levin T, Wing R, DiPasquale K, Raley-Susman KM. Microtubule-associated protein 2 (MAP2) associates with the NMDA receptor and is spatially redistributed within rat hippocampal neurons after oxygen-glucose deprivation. *Brain Res.* 2003;978:38-50. doi: 10.1016/s0006-8993(03)02758-6
55. Park D, Joo SS, Lee HJ, Choi KC, Kim SU, Kim YB. Microtubule-associated protein 2, an early blood marker of ischemic brain injury. *J Neurosci Res.* 2012;90:461-467. doi: 10.1002/jnr.22769
56. Mages B, Fuhs T, Aleithe S, Blietz A, Hobusch C, Hartig W, Schob S, Krueger M, Michalski D. The Cytoskeletal Elements MAP2 and NF-L Show Substantial Alterations in Different Stroke Models While Elevated Serum Levels Highlight Especially MAP2 as a Sensitive Biomarker in Stroke Patients. *Mol Neurobiol.* 2021;58:4051-4069. doi: 10.1007/s12035-021-02372-3
57. Wen Y, Yang SH, Liu R, Perez EJ, Brun-Zinkernagel AM, Koulen P, Simpkins JW. Cdk5 is involved in NFT-like tauopathy induced by transient cerebral ischemia in female rats. *Biochim Biophys Acta.* 2007;1772:473-483. doi: 10.1016/j.bbadis.2006.10.011
58. Ulamek-Kozioł M, Czuczwar SJ, Januszewski S, Pluta R. Proteomic and Genomic Changes in Tau Protein, Which Are Associated with Alzheimer's Disease after Ischemia-Reperfusion Brain Injury. *Int J Mol Sci.* 2020;21. doi: 10.3390/ijms21030892
59. Yuan A, Rao MV, Sasaki T, Chen Y, Kumar A, Veeranna, Liem RK, Eyer J, Peterson AC, Julien JP, et al. Alpha-internexin is structurally and functionally

- associated with the neurofilament triplet proteins in the mature CNS. *J Neurosci*. 2006;26:10006-10019. doi: 10.1523/JNEUROSCI.2580-06.2006
60. Didonna A, Opal P. The role of neurofilament aggregation in neurodegeneration: lessons from rare inherited neurological disorders. *Mol Neurodegener*. 2019;14:19. doi: 10.1186/s13024-019-0318-4
61. Aleithe S, Blietz A, Mages B, Hobusch C, Hartig W, Michalski D. Transcriptional Response and Morphological Features of the Neurovascular Unit and Associated Extracellular Matrix After Experimental Stroke in Mice. *Mol Neurobiol*. 2019;56:7631-7650. doi: 10.1007/s12035-019-1604-4
62. Mages B, Aleithe S, Altmann S, Blietz A, Nitzsche B, Barthel H, Horn AKE, Hobusch C, Hartig W, Krueger M, et al. Impaired Neurofilament Integrity and Neuronal Morphology in Different Models of Focal Cerebral Ischemia and Human Stroke Tissue. *Front Cell Neurosci*. 2018;12:161. doi: 10.3389/fncel.2018.00161
63. Schroeder E, Vogelgesang S, Popa-Wagner A, Kessler C. Neurofilament expression in the rat brain after cerebral infarction: effect of age. *Neurobiol Aging*. 2003;24:135-145. doi: 10.1016/s0197-4580(02)00063-5
64. Dewar D, Dawson DA. Changes of cytoskeletal protein immunostaining in myelinated fibre tracts after focal cerebral ischaemia in the rat. *Acta Neuropathol*. 1997;93:71-77. doi: 10.1007/s004010050584
65. Hartig W, Krueger M, Hofmann S, Preissler H, Markel M, Frydrychowicz C, Mueller WC, Bechmann I, Michalski D. Up-regulation of neurofilament light chains is associated with diminished immunoreactivities for MAP2 and tau after ischemic

- stroke in rodents and in a human case. *J Chem Neuroanat.* 2016;78:140-148. doi: 10.1016/j.jchemneu.2016.09.004
66. Pujol-Calderon F, Portelius E, Zetterberg H, Blennow K, Rosengren LE, Hoglund K. Neurofilament changes in serum and cerebrospinal fluid after acute ischemic stroke. *Neurosci Lett.* 2019;698:58-63. doi: 10.1016/j.neulet.2018.12.042
67. De Marchis GM, Katan M, Barro C, Fladt J, Traenka C, Seiffge DJ, Hert L, Gensicke H, Disanto G, Sutter R, et al. Serum neurofilament light chain in patients with acute cerebrovascular events. *Eur J Neurol.* 2018;25:562-568. doi: 10.1111/ene.13554
68. Nielsen HH, Soares CB, Hogedal SS, Madsen JS, Hansen RB, Christensen AA, Madsen C, Clausen BH, Frich LH, Degn M, et al. Acute Neurofilament Light Chain Plasma Levels Correlate With Stroke Severity and Clinical Outcome in Ischemic Stroke Patients. *Front Neurol.* 2020;11:448. doi: 10.3389/fneur.2020.00448
69. Candelario-Jalil E. Injury and repair mechanisms in ischemic stroke: considerations for the development of novel neurotherapeutics. *Curr Opin Investig Drugs.* 2009;10:644-654.
70. Xing C, Arai K, Lo EH, Hommel M. Pathophysiologic cascades in ischemic stroke. *Int J Stroke.* 2012;7:378-385. doi: 10.1111/j.1747-4949.2012.00839.x
71. Dirnagl U. Inflammation in stroke: the good, the bad, and the unknown. *Ernst Schering Res Found Workshop.* 2004:87-99. doi: 10.1007/978-3-662-05426-0_5
72. Shi K, Tian DC, Li ZG, Ducruet AF, Lawton MT, Shi FD. Global brain inflammation in stroke. *Lancet Neurol.* 2019;18:1058-1066. doi: 10.1016/S1474-4422(19)30078-X

73. Wake H, Moorhouse AJ, Jinno S, Kohsaka S, Nabekura J. Resting microglia directly monitor the functional state of synapses in vivo and determine the fate of ischemic terminals. *J Neurosci.* 2009;29:3974-3980. doi: 10.1523/JNEUROSCI.4363-08.2009
74. Ekdahl CT, Kokaia Z, Lindvall O. Brain inflammation and adult neurogenesis: the dual role of microglia. *Neuroscience.* 2009;158:1021-1029. doi: 10.1016/j.neuroscience.2008.06.052
75. Bachiller S, Jimenez-Ferrer I, Paulus A, Yang Y, Swanberg M, Deierborg T, Boza-Serrano A. Microglia in Neurological Diseases: A Road Map to Brain-Disease Dependent-Inflammatory Response. *Front Cell Neurosci.* 2018;12:488. doi: 10.3389/fncel.2018.00488
76. Banati RB, Gehrmann J, Schubert P, Kreutzberg GW. Cytotoxicity of microglia. *Glia.* 1993;7:111-118. doi: 10.1002/glia.440070117
77. Kettenmann H, Hanisch UK, Noda M, Verkhratsky A. Physiology of microglia. *Physiol Rev.* 2011;91:461-553. doi: 10.1152/physrev.00011.2010
78. Ransohoff RM, Perry VH. Microglial physiology: unique stimuli, specialized responses. *Annu Rev Immunol.* 2009;27:119-145. doi: 10.1146/annurev.immunol.021908.132528
79. Colonna M, Butovsky O. Microglia Function in the Central Nervous System During Health and Neurodegeneration. *Annu Rev Immunol.* 2017;35:441-468. doi: 10.1146/annurev-immunol-051116-052358
80. Patel AR, Ritzel R, McCullough LD, Liu F. Microglia and ischemic stroke: a double-edged sword. *Int J Physiol Pathophysiol Pharmacol.* 2013;5:73-90.

81. Fu R, Shen Q, Xu P, Luo JJ, Tang Y. Phagocytosis of microglia in the central nervous system diseases. *Mol Neurobiol.* 2014;49:1422-1434. doi: 10.1007/s12035-013-8620-6
82. Neumann J, Sauerzweig S, Ronicke R, Gunzer F, Dinkel K, Ullrich O, Gunzer M, Reymann KG. Microglia cells protect neurons by direct engulfment of invading neutrophil granulocytes: a new mechanism of CNS immune privilege. *J Neurosci.* 2008;28:5965-5975. doi: 10.1523/JNEUROSCI.0060-08.2008
83. Morioka T, Kalehua AN, Streit WJ. Characterization of microglial reaction after middle cerebral artery occlusion in rat brain. *J Comp Neurol.* 1993;327:123-132. doi: 10.1002/cne.903270110
84. Schilling M, Besselmann M, Muller M, Strecker JK, Ringelstein EB, Kiefer R. Predominant phagocytic activity of resident microglia over hematogenous macrophages following transient focal cerebral ischemia: an investigation using green fluorescent protein transgenic bone marrow chimeric mice. *Exp Neurol.* 2005;196:290-297. doi: 10.1016/j.expneurol.2005.08.004
85. Sofroniew MV. Molecular dissection of reactive astrogliosis and glial scar formation. *Trends Neurosci.* 2009;32:638-647. doi: 10.1016/j.tins.2009.08.002
86. Farina C, Aloisi F, Meinl E. Astrocytes are active players in cerebral innate immunity. *Trends Immunol.* 2007;28:138-145. doi: 10.1016/j.it.2007.01.005
87. Gotz M, Huttner WB. The cell biology of neurogenesis. *Nat Rev Mol Cell Biol.* 2005;6:777-788. doi: 10.1038/nrm1739
88. Nowicka D, Rogozinska K, Aleksy M, Witte OW, Skangiel-Kramska J. Spatiotemporal dynamics of astroglial and microglial responses after

- photothrombotic stroke in the rat brain. *Acta Neurobiol Exp (Wars)*. 2008;68:155-168.
89. Huang L, Wu ZB, Zhuge Q, Zheng W, Shao B, Wang B, Sun F, Jin K. Glial scar formation occurs in the human brain after ischemic stroke. *Int J Med Sci*. 2014;11:344-348. doi: 10.7150/ijms.8140
90. Wang H, Song G, Chuang H, Chiu C, Abdelmaksoud A, Ye Y, Zhao L. Portrait of glial scar in neurological diseases. *Int J Immunopathol Pharmacol*. 2018;31:2058738418801406. doi: 10.1177/2058738418801406
91. Rolls A, Shechter R, Schwartz M. The bright side of the glial scar in CNS repair. *Nat Rev Neurosci*. 2009;10:235-241. doi: 10.1038/nrn2591
92. Wanner IB, Deik A, Torres M, Rosendahl A, Neary JT, Lemmon VP, Bixby JL. A new in vitro model of the glial scar inhibits axon growth. *Glia*. 2008;56:1691-1709. doi: 10.1002/glia.20721
93. Terenzio M, Schiavo G, Fainzilber M. Compartmentalized Signaling in Neurons: From Cell Biology to Neuroscience. *Neuron*. 2017;96:667-679. doi: 10.1016/j.neuron.2017.10.015
94. Zhang S, Zuo W, Guo XF, He WB, Chen NH. Cerebral glucose transporter: the possible therapeutic target for ischemic stroke. *Neurochem Int*. 2014;70:22-29. doi: 10.1016/j.neuint.2014.03.007
95. Camandola S, Mattson MP. Brain metabolism in health, aging, and neurodegeneration. *EMBO J*. 2017;36:1474-1492. doi: 10.15252/emj.201695810

96. Zhang S, Lachance BB, Mattson MP, Jia X. Glucose metabolic crosstalk and regulation in brain function and diseases. *Prog Neurobiol.* 2021;204:102089. doi: 10.1016/j.pneurobio.2021.102089
97. Putzu A, Valtorta S, Di Grigoli G, Haenggi M, Belloli S, Malgaroli A, Gemma M, Landoni G, Beretta L, Moresco RM. Regional Differences in Cerebral Glucose Metabolism After Cardiac Arrest and Resuscitation in Rats Using [(18)F]FDG Positron Emission Tomography and Autoradiography. *Neurocrit Care.* 2018;28:370-378. doi: 10.1007/s12028-017-0445-0
98. Hahn DK, Geocadin RG, Greer DM. Quality of evidence in studies evaluating neuroimaging for neurologic prognostication in adult patients resuscitated from cardiac arrest. *Resuscitation.* 2014;85:165-172. doi: 10.1016/j.resuscitation.2013.10.031
99. Li YQ, Liao XX, Lu JH, Liu R, Hu CL, Dai G, Zhang XS, Shi XC, Li X. Assessing the early changes of cerebral glucose metabolism via dynamic (18)FDG-PET/CT during cardiac arrest. *Metab Brain Dis.* 2015;30:969-977. doi: 10.1007/s11011-015-9658-0
100. Walberer M, Backes H, Rueger MA, Neumaier B, Endepols H, Hoehn M, Fink GR, Schroeter M, Graf R. Potential of early [(18)F]-2-fluoro-2-deoxy-D-glucose positron emission tomography for identifying hypoperfusion and predicting fate of tissue in a rat embolic stroke model. *Stroke.* 2012;43:193-198. doi: 10.1161/STROKEAHA.111.624551
101. Yuan H, Frank JE, Hong Y, An H, Eldeniz C, Nie J, Bunevicius A, Shen D, Lin W. Spatiotemporal uptake characteristics of [18]F-2-fluoro-2-deoxy-D-glucose in a rat

- middle cerebral artery occlusion model. *Stroke*. 2013;44:2292-2299. doi: 10.1161/STROKEAHA.113.000903
102. Backes H, Walberer M, Ladwig A, Rueger MA, Neumaier B, Endepols H, Hoehn M, Fink GR, Schroeter M, Graf R. Glucose consumption of inflammatory cells masks metabolic deficits in the brain. *Neuroimage*. 2016;128:54-62. doi: 10.1016/j.neuroimage.2015.12.044
103. Li Y, Lu B, Sheng L, Zhu Z, Sun H, Zhou Y, Yang Y, Xue D, Chen W, Tian X, et al. Hexokinase 2-dependent hyperglycolysis driving microglial activation contributes to ischemic brain injury. *J Neurochem*. 2018;144:186-200. doi: 10.1111/jnc.14267
104. Lauro C, Chece G, Monaco L, Antonangeli F, Peruzzi G, Rinaldo S, Paone A, Cutruzzola F, Limatola C. Fractalkine Modulates Microglia Metabolism in Brain Ischemia. *Front Cell Neurosci*. 2019;13:414. doi: 10.3389/fncel.2019.00414
105. Amaral AI, Teixeira AP, Martens S, Bernal V, Sousa MF, Alves PM. Metabolic alterations induced by ischemia in primary cultures of astrocytes: merging ¹³C NMR spectroscopy and metabolic flux analysis. *J Neurochem*. 2010;113:735-748. doi: 10.1111/j.1471-4159.2010.06636.x
106. Zhou P, Guan T, Jiang Z, Namaka M, Huang QJ, Kong JM. Monocarboxylate transporter 1 and the vulnerability of oligodendrocyte lineage cells to metabolic stresses. *CNS Neurosci Ther*. 2018;24:126-134. doi: 10.1111/cns.12782
107. Simmatis LER, Scott SH, Jin AY. The Impact of Transient Ischemic Attack (TIA) on Brain and Behavior. *Front Behav Neurosci*. 2019;13:44. doi: 10.3389/fnbeh.2019.00044

108. Roy Choudhury G, Ryou MG, Poteet E, Wen Y, He R, Sun F, Yuan F, Jin K, Yang SH. Involvement of p38 MAPK in reactive astrogliosis induced by ischemic stroke. *Brain Res.* 2014;1551:45-58. doi: 10.1016/j.brainres.2014.01.013
109. Garcia JH, Wagner S, Liu KF, Hu XJ. Neurological deficit and extent of neuronal necrosis attributable to middle cerebral artery occlusion in rats. Statistical validation. *Stroke.* 1995;26:627-634; discussion 635. doi: 10.1161/01.str.26.4.627
110. Schallert T, Fleming SM, Leasure JL, Tillerson JL, Bland ST. CNS plasticity and assessment of forelimb sensorimotor outcome in unilateral rat models of stroke, cortical ablation, parkinsonism and spinal cord injury. *Neuropharmacology.* 2000;39:777-787. doi: 10.1016/s0028-3908(00)00005-8
111. Shi J, Yang SH, Stubbley L, Day AL, Simpkins JW. Hypoperfusion induces overexpression of beta-amyloid precursor protein mRNA in a focal ischemic rodent model. *Brain Res.* 2000;853:1-4. doi: 10.1016/s0006-8993(99)02113-7
112. Greenberg DA, Jin K. Vascular endothelial growth factors (VEGFs) and stroke. *Cell Mol Life Sci.* 2013;70:1753-1761. doi: 10.1007/s00018-013-1282-8
113. Chen HH, Chien CH, Liu HM. Correlation between angiogenesis and basic fibroblast growth factor expression in experimental brain infarct. *Stroke.* 1994;25:1651-1657. doi: 10.1161/01.str.25.8.1651
114. Hatakeyama M, Ninomiya I, Kanazawa M. Angiogenesis and neuronal remodeling after ischemic stroke. *Neural Regen Res.* 2020;15:16-19. doi: 10.4103/1673-5374.264442

115. Zhang ZG, Zhang L, Jiang Q, Zhang R, Davies K, Powers C, Bruggen N, Chopp M. VEGF enhances angiogenesis and promotes blood-brain barrier leakage in the ischemic brain. *J Clin Invest*. 2000;106:829-838. doi: 10.1172/JCI9369
116. Jakel L, De Kort AM, Klijn CJM, Schreuder F, Verbeek MM. Prevalence of cerebral amyloid angiopathy: A systematic review and meta-analysis. *Alzheimers Dement*. 2022;18:10-28. doi: 10.1002/alz.12366
117. Govindpani K, McNamara LG, Smith NR, Vinnakota C, Waldvogel HJ, Faull RL, Kwakowsky A. Vascular Dysfunction in Alzheimer's Disease: A Prelude to the Pathological Process or a Consequence of It? *J Clin Med*. 2019;8. doi: 10.3390/jcm8050651
118. Yang J, Wong A, Wang Z, Liu W, Au L, Xiong Y, Chu WW, Leung EY, Chen S, Lau C, et al. Risk factors for incident dementia after stroke and transient ischemic attack. *Alzheimers Dement*. 2015;11:16-23. doi: 10.1016/j.jalz.2014.01.003
119. Corriveau RA, Bosetti F, Emr M, Gladman JT, Koenig JI, Moy CS, Pahigiannis K, Waddy SP, Koroshetz W. The Science of Vascular Contributions to Cognitive Impairment and Dementia (VCID): A Framework for Advancing Research Priorities in the Cerebrovascular Biology of Cognitive Decline. *Cell Mol Neurobiol*. 2016;36:281-288. doi: 10.1007/s10571-016-0334-7
120. Wen Y, Yang S, Liu R, Brun-Zinkernagel AM, Koulen P, Simpkins JW. Transient cerebral ischemia induces aberrant neuronal cell cycle re-entry and Alzheimer's disease-like tauopathy in female rats. *J Biol Chem*. 2004;279:22684-22692. doi: 10.1074/jbc.M311768200

121. Tesco G, Koh YH, Kang EL, Cameron AN, Das S, Sena-Esteves M, Hiltunen M, Yang SH, Zhong Z, Shen Y, et al. Depletion of GGA3 stabilizes BACE and enhances beta-secretase activity. *Neuron*. 2007;54:721-737. doi: 10.1016/j.neuron.2007.05.012
122. Dawson DA, Hallenbeck JM. Acute focal ischemia-induced alterations in MAP2 immunostaining: description of temporal changes and utilization as a marker for volumetric assessment of acute brain injury. *J Cereb Blood Flow Metab*. 1996;16:170-174. doi: 10.1097/00004647-199601000-00020
123. Zetterberg H. Neurofilament Light: A Dynamic Cross-Disease Fluid Biomarker for Neurodegeneration. *Neuron*. 2016;91:1-3. doi: 10.1016/j.neuron.2016.06.030
124. Stassart RM, Mobius W, Nave KA, Edgar JM. The Axon-Myelin Unit in Development and Degenerative Disease. *Front Neurosci*. 2018;12:467. doi: 10.3389/fnins.2018.00467
125. LoPresti P. Tau in Oligodendrocytes Takes Neurons in Sickness and in Health. *Int J Mol Sci*. 2018;19. doi: 10.3390/ijms19082408
126. Seiberlich V, Bauer NG, Schwarz L, Ffrench-Constant C, Goldbaum O, Richter-Landsberg C. Downregulation of the microtubule associated protein tau impairs process outgrowth and myelin basic protein mRNA transport in oligodendrocytes. *Glia*. 2015;63:1621-1635. doi: 10.1002/glia.22832
127. Lyu J, Jiang X, Leak RK, Shi Y, Hu X, Chen J. Microglial Responses to Brain Injury and Disease: Functional Diversity and New Opportunities. *Transl Stroke Res*. 2021;12:474-495. doi: 10.1007/s12975-020-00857-2

128. Prinz M, Jung S, Priller J. Microglia Biology: One Century of Evolving Concepts. *Cell*. 2019;179:292-311. doi: 10.1016/j.cell.2019.08.053
129. Askew K, Li K, Olmos-Alonso A, Garcia-Moreno F, Liang Y, Richardson P, Tipton T, Chapman MA, Riecken K, Beccari S, et al. Coupled Proliferation and Apoptosis Maintain the Rapid Turnover of Microglia in the Adult Brain. *Cell Rep*. 2017;18:391-405. doi: 10.1016/j.celrep.2016.12.041
130. Tariq S, Tsang A, Wang M, Reaume N, Carlson H, Sajobi TT, Longman RS, Smith EE, Frayne R, d'Esterre CD, et al. White matter tract microstructure and cognitive performance after transient ischemic attack. *PLoS One*. 2020;15:e0239116. doi: 10.1371/journal.pone.0239116
131. Nasrabady SE, Rizvi B, Goldman JE, Brickman AM. White matter changes in Alzheimer's disease: a focus on myelin and oligodendrocytes. *Acta Neuropathol Commun*. 2018;6:22. doi: 10.1186/s40478-018-0515-3
132. Gaetani L, Blennow K, Calabresi P, Di Filippo M, Parnetti L, Zetterberg H. Neurofilament light chain as a biomarker in neurological disorders. *J Neurol Neurosurg Psychiatry*. 2019;90:870-881. doi: 10.1136/jnnp-2018-320106
133. Xi G. Clinical translation of cerebral preconditioning. *Transl Stroke Res*. 2010;1:2-3. doi: 10.1007/s12975-010-0012-x
134. Colas-Campas L, Farre J, Mauri-Capdevila G, Molina-Seguin J, Aymerich N, Ois A, Roquer J, Tur S, Garcia-Carreira MDC, Marti-Fabregas J, et al. Inflammatory Response of Ischemic Tolerance in Circulating Plasma: Preconditioning-Induced by Transient Ischemic Attack (TIA) Phenomena in Acute Ischemia Patients (AIS). *Front Neurol*. 2020;11:552470. doi: 10.3389/fneur.2020.552470

135. Johnston SC. Ischemic preconditioning from transient ischemic attacks? Data from the Northern California TIA Study. *Stroke*. 2004;35:2680-2682. doi: 10.1161/01.STR.0000143322.20491.0f
136. Ghozy S, Kacimi SEO, Elfil M, Sobeeh MG, Reda A, Kallmes KM, Rabinstein AA, Holmes DR, Jr., Brinjikji W, Kadirvel R, et al. Transient Ischemic Attacks Preceding Ischemic Stroke and the Possible Preconditioning of the Human Brain: A Systematic Review and Meta-Analysis. *Front Neurol*. 2021;12:755167. doi: 10.3389/fneur.2021.755167
137. McDonough A, Weinstein JR. The role of microglia in ischemic preconditioning. *Glia*. 2020;68:455-471. doi: 10.1002/glia.23695
138. Salter MW, Stevens B. Microglia emerge as central players in brain disease. *Nat Med*. 2017;23:1018-1027. doi: 10.1038/nm.4397
139. Dienel GA. Brain Glucose Metabolism: Integration of Energetics with Function. *Physiol Rev*. 2019;99:949-1045. doi: 10.1152/physrev.00062.2017
140. van Aalst J, Ceccarini J, Sunaert S, Dupont P, Koole M, Van Laere K. In vivo synaptic density relates to glucose metabolism at rest in healthy subjects, but is strongly modulated by regional differences. *J Cereb Blood Flow Metab*. 2021;41:1978-1987. doi: 10.1177/0271678X20981502
141. Shokri-Kojori E, Tomasi D, Alipanahi B, Wiers CE, Wang GJ, Volkow ND. Correspondence between cerebral glucose metabolism and BOLD reveals relative power and cost in human brain. *Nat Commun*. 2019;10:690. doi: 10.1038/s41467-019-08546-x

142. Kleinridders A, Ferris HA, Reyzer ML, Rath M, Soto M, Manier ML, Spraggins J, Yang Z, Stanton RC, Caprioli RM, et al. Regional differences in brain glucose metabolism determined by imaging mass spectrometry. *Mol Metab.* 2018;12:113-121. doi: 10.1016/j.molmet.2018.03.013
143. Mergenthaler P, Lindauer U, Dienel GA, Meisel A. Sugar for the brain: the role of glucose in physiological and pathological brain function. *Trends Neurosci.* 2013;36:587-597. doi: 10.1016/j.tins.2013.07.001
144. Chen L, Wei Z, Chan KW, Li Y, Suchal K, Bi S, Huang J, Xu X, Wong PC, Lu H, et al. D-Glucose uptake and clearance in the tauopathy Alzheimer's disease mouse brain detected by on-resonance variable delay multiple pulse MRI. *J Cereb Blood Flow Metab.* 2021;41:1013-1025. doi: 10.1177/0271678X20941264
145. Grist JT, Miller JJ, Zaccagna F, McLean MA, Riemer F, Matys T, Tyler DJ, Laustsen C, Coles AJ, Gallagher FA. Hyperpolarized (13)C MRI: A novel approach for probing cerebral metabolism in health and neurological disease. *J Cereb Blood Flow Metab.* 2020;40:1137-1147. doi: 10.1177/0271678X20909045
146. Rogers GW, Brand MD, Petrosyan S, Ashok D, Elorza AA, Ferrick DA, Murphy AN. High throughput microplate respiratory measurements using minimal quantities of isolated mitochondria. *PLoS One.* 2011;6:e21746. doi: 10.1371/journal.pone.0021746
147. Schuh RA, Clerc P, Hwang H, Mehrabian Z, Bittman K, Chen H, Polster BM. Adaptation of microplate-based respirometry for hippocampal slices and analysis of respiratory capacity. *J Neurosci Res.* 2011;89:1979-1988. doi: 10.1002/jnr.22650

148. Fried NT, Moffat C, Seifert EL, Oshinsky ML. Functional mitochondrial analysis in acute brain sections from adult rats reveals mitochondrial dysfunction in a rat model of migraine. *Am J Physiol Cell Physiol.* 2014;307:C1017-1030. doi: 10.1152/ajpcell.00332.2013
149. Underwood E, Redell JB, Zhao J, Moore AN, Dash PK. A method for assessing tissue respiration in anatomically defined brain regions. *Sci Rep.* 2020;10:13179. doi: 10.1038/s41598-020-69867-2
150. Qi G, Mi Y, Yin F. Characterizing brain metabolic function ex vivo with acute mouse slice punches. *STAR Protoc.* 2021;2:100559. doi: 10.1016/j.xpro.2021.100559
151. Chaudhari K, Wang L, Kruse J, Winters A, Sumien N, Shetty R, Prah J, Liu R, Shi J, Forster M, et al. Early loss of cerebellar Purkinje cells in human and a transgenic mouse model of Alzheimer's disease. *Neurol Res.* 2021;43:570-581. doi: 10.1080/01616412.2021.1893566
152. Percie du Sert N, Hurst V, Ahluwalia A, Alam S, Avey MT, Baker M, Browne WJ, Clark A, Cuthill IC, Dirnagl U, et al. The ARRIVE guidelines 2.0: Updated guidelines for reporting animal research. *J Cereb Blood Flow Metab.* 2020;40:1769-1777. doi: 10.1177/0271678X20943823
153. Ruas JS, Siqueira-Santos ES, Amigo I, Rodrigues-Silva E, Kowaltowski AJ, Castilho RF. Underestimation of the Maximal Capacity of the Mitochondrial Electron Transport System in Oligomycin-Treated Cells. *PLoS One.* 2016;11:e0150967. doi: 10.1371/journal.pone.0150967
154. Bentourkia M, Bol A, Ivanoiu A, Labar D, Sibomana M, Coppens A, Michel C, Cosnard G, De Volder AG. Comparison of regional cerebral blood flow and glucose

- metabolism in the normal brain: effect of aging. *J Neurol Sci.* 2000;181:19-28. doi: 10.1016/s0022-510x(00)00396-8
155. Vaishnavi SN, Vlassenko AG, Rundle MM, Snyder AZ, Mintun MA, Raichle ME. Regional aerobic glycolysis in the human brain. *Proc Natl Acad Sci U S A.* 2010;107:17757-17762. doi: 10.1073/pnas.1010459107
156. Goyal MS, Hawrylycz M, Miller JA, Snyder AZ, Raichle ME. Aerobic glycolysis in the human brain is associated with development and neotenus gene expression. *Cell Metab.* 2014;19:49-57. doi: 10.1016/j.cmet.2013.11.020
157. Howarth C, Gleeson P, Attwell D. Updated energy budgets for neural computation in the neocortex and cerebellum. *J Cereb Blood Flow Metab.* 2012;32:1222-1232. doi: 10.1038/jcbfm.2012.35
158. Hall CN, Klein-Flugge MC, Howarth C, Attwell D. Oxidative phosphorylation, not glycolysis, powers presynaptic and postsynaptic mechanisms underlying brain information processing. *J Neurosci.* 2012;32:8940-8951. doi: 10.1523/JNEUROSCI.0026-12.2012
159. Azevedo FA, Carvalho LR, Grinberg LT, Farfel JM, Ferretti RE, Leite RE, Jacob Filho W, Lent R, Herculano-Houzel S. Equal numbers of neuronal and nonneuronal cells make the human brain an isometrically scaled-up primate brain. *J Comp Neurol.* 2009;513:532-541. doi: 10.1002/cne.21974
160. Badura A, De Zeeuw CI. Cerebellar Granule Cells: Dense, Rich and Evolving Representations. *Curr Biol.* 2017;27:R415-R418. doi: 10.1016/j.cub.2017.04.009
161. Brand MD, Nicholls DG. Assessing mitochondrial dysfunction in cells. *Biochem J.* 2011;435:297-312. doi: 10.1042/BJ20110162

162. Arias-Reyes C, Losantos-Ramos K, Gonzales M, Furrer D, Soliz J. NADH-linked mitochondrial respiration in the developing mouse brain is sex-, age- and tissue-dependent. *Respir Physiol Neurobiol.* 2019;266:156-162. doi: 10.1016/j.resp.2019.05.011
163. Cocco T, Pacelli C, Sgobbo P, Villani G. Control of OXPHOS efficiency by complex I in brain mitochondria. *Neurobiol Aging.* 2009;30:622-629. doi: 10.1016/j.neurobiolaging.2007.08.002
164. Divakaruni AS, Brand MD. The regulation and physiology of mitochondrial proton leak. *Physiology (Bethesda).* 2011;26:192-205. doi: 10.1152/physiol.00046.2010
165. Mailloux RJ, Adjeitey CN, Harper ME. Genipin-induced inhibition of uncoupling protein-2 sensitizes drug-resistant cancer cells to cytotoxic agents. *PLoS One.* 2010;5:e13289. doi: 10.1371/journal.pone.0013289
166. Jo MJ, Jeong S, Yun HK, Kim DY, Kim BR, Kim JL, Na YJ, Park SH, Jeong YA, Kim BG, et al. Genipin induces mitochondrial dysfunction and apoptosis via downregulation of Stat3/mcl-1 pathway in gastric cancer. *BMC Cancer.* 2019;19:739. doi: 10.1186/s12885-019-5957-x
167. Rubattu S, Stanzione R, Bianchi F, Cotugno M, Forte M, Della Ragione F, Fioriniello S, D'Esposito M, Marchitti S, Madonna M, et al. Reduced brain UCP2 expression mediated by microRNA-503 contributes to increased stroke susceptibility in the high-salt fed stroke-prone spontaneously hypertensive rat. *Cell Death Dis.* 2017;8:e2891. doi: 10.1038/cddis.2017.278

168. Fridell YW, Sanchez-Blanco A, Silvia BA, Helfand SL. Targeted expression of the human uncoupling protein 2 (hUCP2) to adult neurons extends life span in the fly. *Cell Metab.* 2005;1:145-152. doi: 10.1016/j.cmet.2005.01.005
169. Kiyatkin EA, Wise RA. Striatal hyperthermia associated with arousal: intracranial thermorecordings in behaving rats. *Brain Res.* 2001;918:141-152. doi: 10.1016/s0006-8993(01)02985-7
170. Kiyatkin EA, Wise RA. Brain and body hyperthermia associated with heroin self-administration in rats. *J Neurosci.* 2002;22:1072-1080.
171. Kiyatkin EA, Brown PL, Wise RA. Brain temperature fluctuation: a reflection of functional neural activation. *Eur J Neurosci.* 2002;16:164-168. doi: 10.1046/j.1460-9568.2002.02066.x
172. Brown PL, Wise RA, Kiyatkin EA. Brain hyperthermia is induced by methamphetamine and exacerbated by social interaction. *J Neurosci.* 2003;23:3924-3929.
173. Kiyatkin EA. Brain temperature and its role in physiology and pathophysiology: Lessons from 20 years of thermorecording. *Temperature (Austin).* 2019;6:271-333. doi: 10.1080/23328940.2019.1691896
174. Andrews ZB, Diano S, Horvath TL. Mitochondrial uncoupling proteins in the CNS: in support of function and survival. *Nat Rev Neurosci.* 2005;6:829-840. doi: 10.1038/nrn1767
175. Rajagopal MC, Brown JW, Gelda D, Valavala KV, Wang H, Llano DA, Gillette R, Sinha S. Transient heat release during induced mitochondrial proton uncoupling. *Commun Biol.* 2019;2:279. doi: 10.1038/s42003-019-0535-y

176. Hardie DG. AMP-activated protein kinase: an energy sensor that regulates all aspects of cell function. *Genes Dev.* 2011;25:1895-1908. doi: 10.1101/gad.17420111
177. Culmsee C, Monnig J, Kemp BE, Mattson MP. AMP-activated protein kinase is highly expressed in neurons in the developing rat brain and promotes neuronal survival following glucose deprivation. *J Mol Neurosci.* 2001;17:45-58. doi: 10.1385/JMN:17:1:45
178. Steinberg GR, Kemp BE. AMPK in Health and Disease. *Physiol Rev.* 2009;89:1025-1078. doi: 10.1152/physrev.00011.2008
89/3/1025 [pii]
179. Imai K, Inukai K, Ikegami Y, Awata T, Katayama S. LKB1, an upstream AMPK kinase, regulates glucose and lipid metabolism in cultured liver and muscle cells. *Biochem Biophys Res Commun.* 2006;351:595-601. doi: S0006-291X(06)02305-9 [pii]
10.1016/j.bbrc.2006.10.056
180. Sakamoto K, Zarrinpashneh E, Budas GR, Pouleur AC, Dutta A, Prescott AR, Vanoverschelde JL, Ashworth A, Jovanovic A, Alessi DR, et al. Deficiency of LKB1 in heart prevents ischemia-mediated activation of AMPKalpha2 but not AMPKalpha1. *Am J Physiol Endocrinol Metab.* 2006;290:E780-788. doi: 00443.2005 [pii]
10.1152/ajpendo.00443.2005

181. Alessi DR, Sakamoto K, Bayascas JR. LKB1-dependent signaling pathways. *Annu Rev Biochem.* 2006;75:137-163. doi: 10.1146/annurev.biochem.75.103004.142702
182. Hardie DG, Carling D, Gamblin SJ. AMP-activated protein kinase: also regulated by ADP? *Trends Biochem Sci.* 2011;36:470-477. doi: 10.1016/j.tibs.2011.06.004
183. Chen CH, Cheng YW, Chen YF, Tang SC, Jeng JS. Plasma neurofilament light chain and glial fibrillary acidic protein predict stroke in CADASIL. *J Neuroinflammation.* 2020;17:124. doi: 10.1186/s12974-020-01813-5
184. Laverse E, Guo T, Zimmerman K, Foiani MS, Velani B, Morrow P, Adejuwon A, Bamford R, Underwood N, George J, et al. Plasma glial fibrillary acidic protein and neurofilament light chain, but not tau, are biomarkers of sports-related mild traumatic brain injury. *Brain Commun.* 2020;2:fcaa137. doi: 10.1093/braincomms/fcaa137
185. Koellhoffer EC, McCullough LD. The effects of estrogen in ischemic stroke. *Transl Stroke Res.* 2013;4:390-401. doi: 10.1007/s12975-012-0230-5
186. Halpain S, Dehmelt L. The MAP1 family of microtubule-associated proteins. *Genome Biol.* 2006;7:224. doi: 10.1186/gb-2006-7-6-224
187. Sanchez C, Diaz-Nido J, Avila J. Phosphorylation of microtubule-associated protein 2 (MAP2) and its relevance for the regulation of the neuronal cytoskeleton function. *Prog Neurobiol.* 2000;61:133-168. doi: 10.1016/s0301-0082(99)00046-5
188. Perrot R, Berges R, Bocquet A, Eyer J. Review of the multiple aspects of neurofilament functions, and their possible contribution to neurodegeneration. *Mol Neurobiol.* 2008;38:27-65. doi: 10.1007/s12035-008-8033-0

FIGURES

Table 1: Antibodies used in Western blot and immunofluorescence staining

Name	Western blot	IHC	Catalog	Company
GFAP	1:1000	1:250	3670	Cell Signaling Technology
GFAP		1:250	12389	Cell Signaling Technology
BACE1	1:1000		5606	Cell Signaling Technology
MAP2	1:1000	1:200	8707	Cell Signaling Technology
Neurofilament-L	1:1000	1:150	2823	Cell Signaling Technology
Phospho-tau (Ser396)	1:1000	1:150	32057	Abcam
Phospho-tau (Ser202, Thr205)	1:1000	1:150	1020	Invitrogen
Tau	1:1000	1:150	76128	Abcam
Iba1	1:1000	1:200	17198	Cell Signaling Technology
MBP		1:400	50035	Novus Biologicals
β -actin	1:1000	1:200	47778	Santa Cruz Biotechnology
VEGF	1:1000	1:200	7269	Santa Cruz Biotechnology

Behavior Test: Neurological Score + Cylinder Test

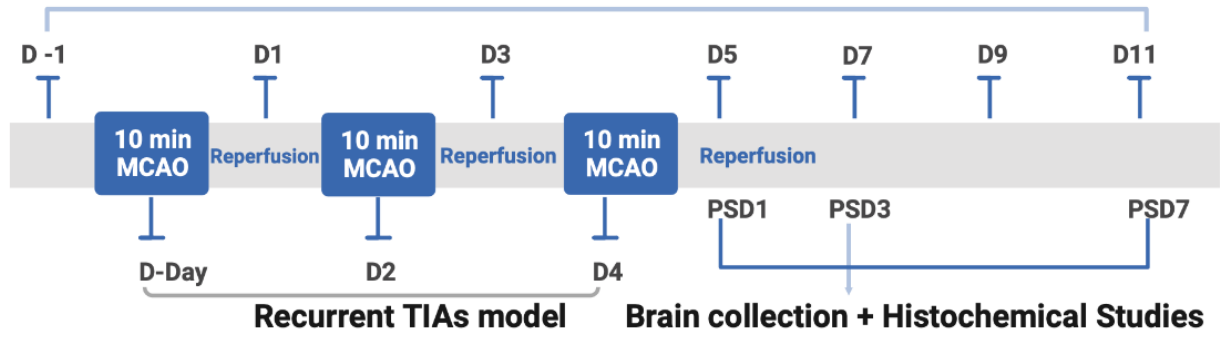


Figure 1: A schema depicts the process of recurrent TIA, behavior assessment, and tissue harvest.

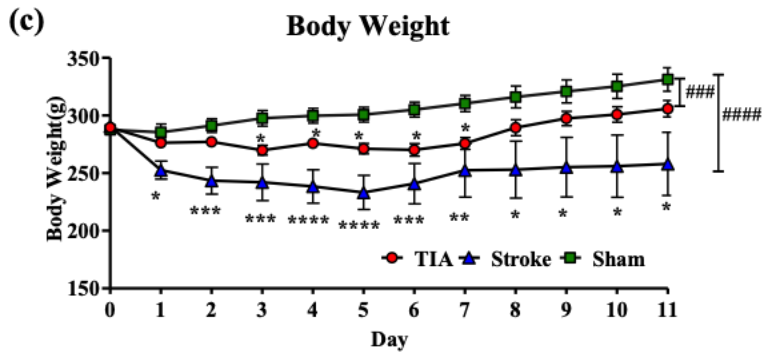
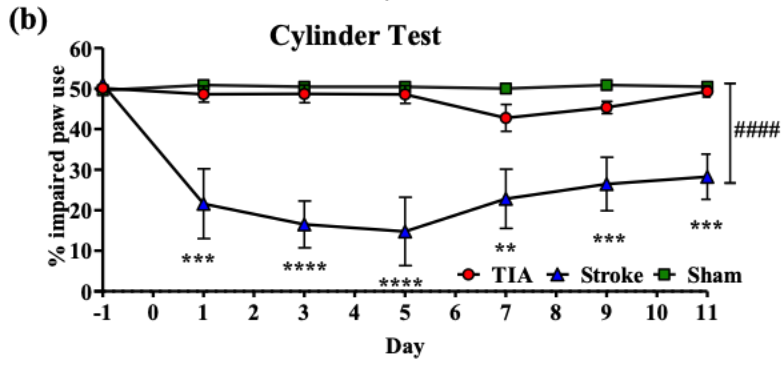
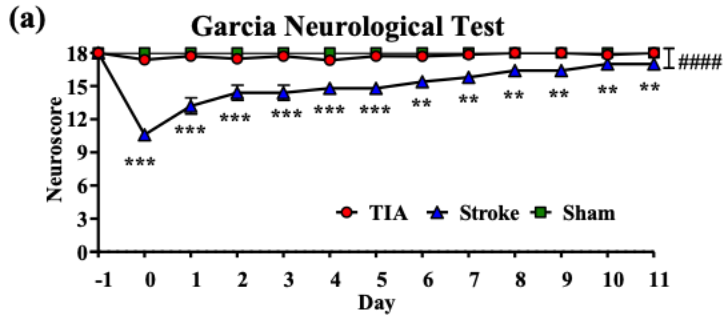


Figure 2. Behavior assessment and body weight measurements after recurrent TIA, ischemic stroke, and sham groups.

(a) Garcia neurological test and cylinder test (b) measured for up to 7-day reperfusion after recurrent TIA as compared to ischemic stroke and sham group. (c) Body weight measured among the groups. Data are expressed as mean and SEM. (n=6-21 for TIA; n= 5 for stroke; n=6 for sham.) ###p < 0.001; ####p < 0.0001 vs sham group, two-way ANOVA followed by Bonferroni's multiple comparison test was used among groups. *p < 0.05, **p < 0.01; ***p < 0.001; ****p < 0.0001 vs sham group for each time point. Kruskal-Wallis test followed by Dunn's multiple comparison test was used to test Garcia neurological scoring and one-way ANOVA followed by Tukey's multiple comparison test was used in cylinder test and body weight measurement.

Bregma +1~-1 mm

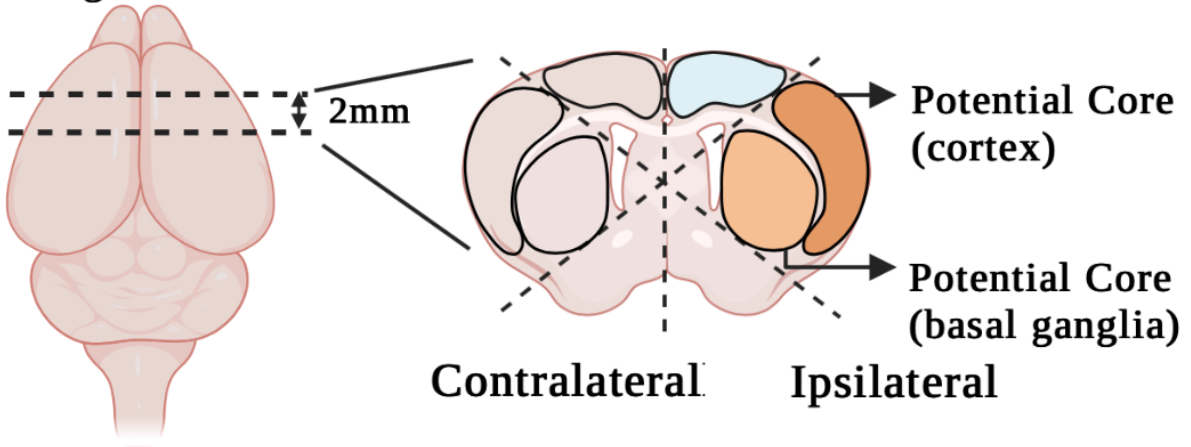


Figure 3. A schema depicting the location and region collected for tissue analysis from recurrent TIA samples.

TUNEL Assay

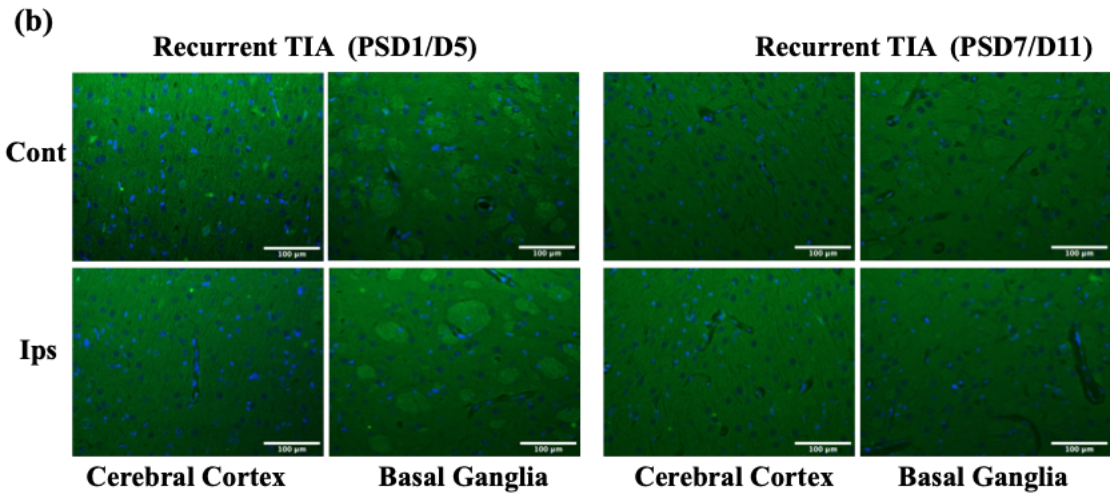
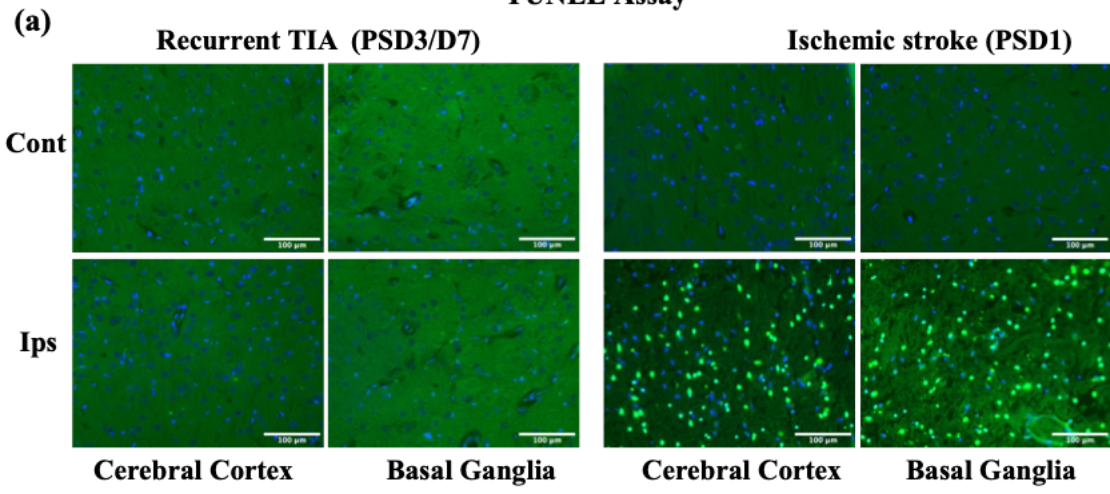


Figure 4. Terminal deoxynucleotidyl transferase-mediated dUTP nick-end labeling (TUNEL) staining on day-1,3,7 after recurrent TIA.

(a) Representative images of TUNEL staining on day-3 after recurrent TIA (PSD3/D7) from contralateral (Cont) and ipsilateral side (Ips) in cerebral cortex and basal ganglia region as compared to the ischemic stroke (75-min MCAO) as a positive control. (b) Representative images of TUNEL staining at post-surgery-day1/D3 and day7/D11 after recurrent TIAs from contralateral (Cont) and ipsilateral side (Ips) in cerebral cortex and basal ganglia region. Scale bars = 100 μ m.

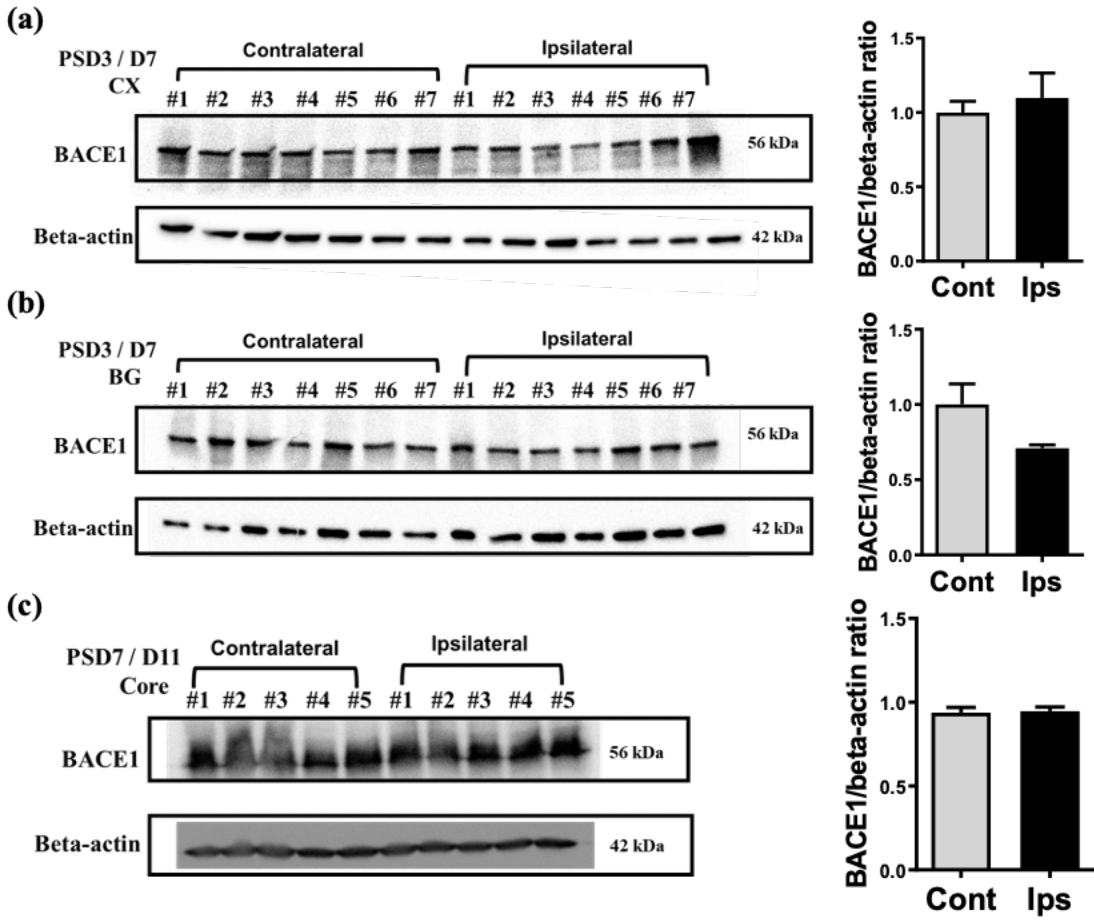


Figure 5. Beta-site amyloid precursor protein (APP) cleaving enzyme-1 (BACE1) alteration after recurrent TIA.

(a,b,c) Representative western blot and data analysis of BACE1 from affected cerebral cortex (CX) and basal ganglia (BG) regions in the ipsilateral and contralateral side at PSD3/D7 (n=5) and PSD7/D11 after recurrent TIAs. (n=5). Data are expressed as mean and SEM. *p < 0.05 in paired t-test.

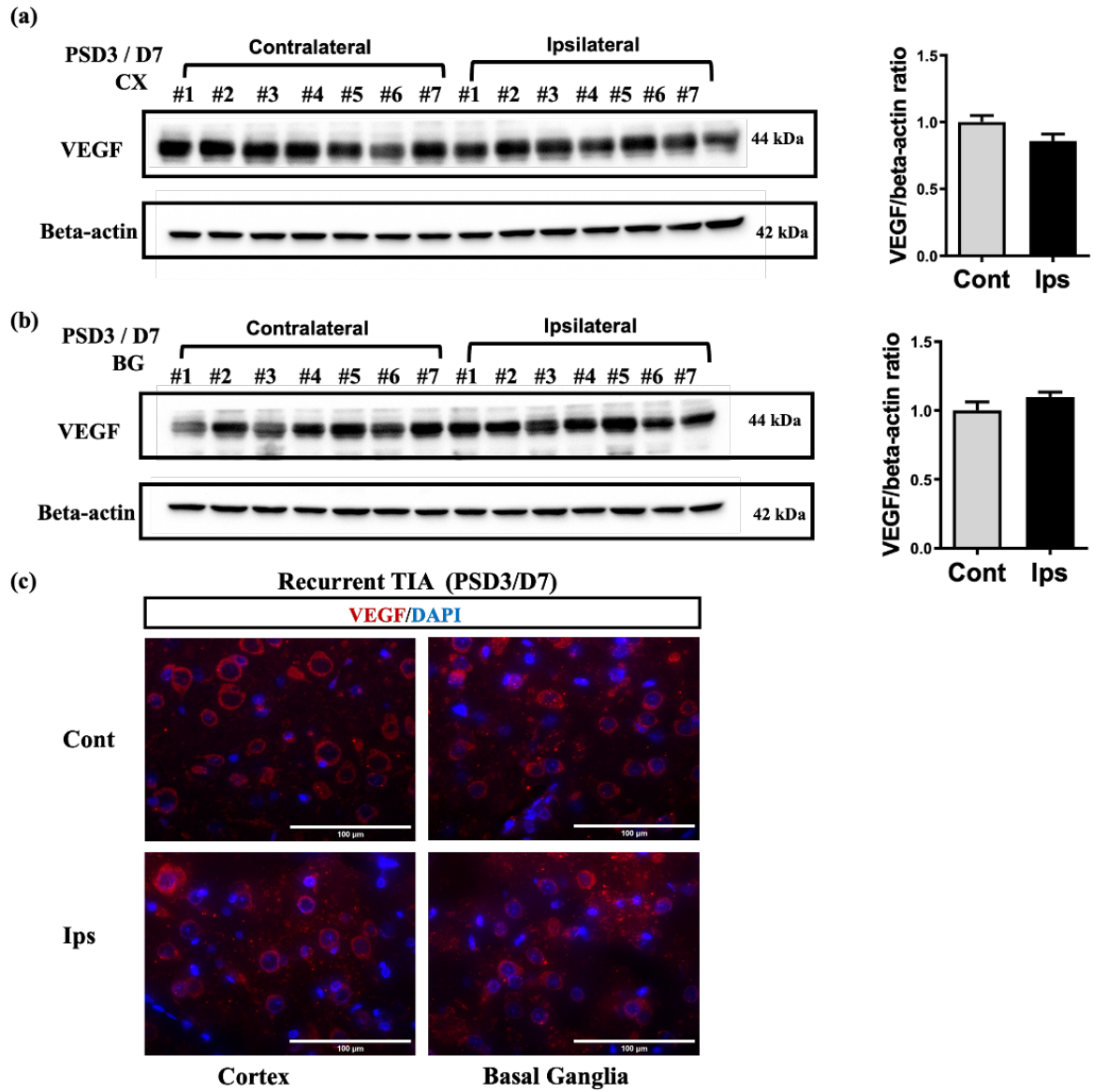


Figure 6. Vascular endothelial growth factor (VEGF) alteration after recurrent TIA.

(a,b) Representative western blot and data analysis of VEGF from affected cerebral cortex (CX) and basal ganglia (BG) regions in the ipsilateral and contralateral side at PSD3/D7 after recurrent TIAs. (n=7) (c) Representative images of VEGF staining at post-surgery-day3/D7 after recurrent TIAs from contralateral (Cont) and ipsilateral side (Ips) in cerebral cortex and basal ganglia region. Scale bars = 100 μ m. Data are expressed as mean and SEM. * $p < 0.05$ in paired t-test.

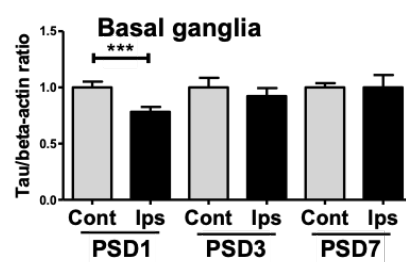
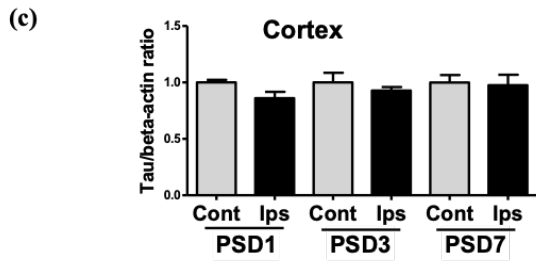
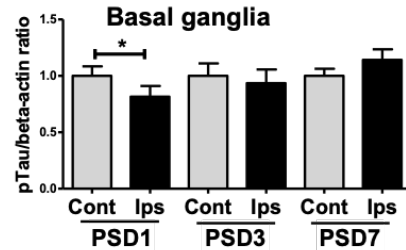
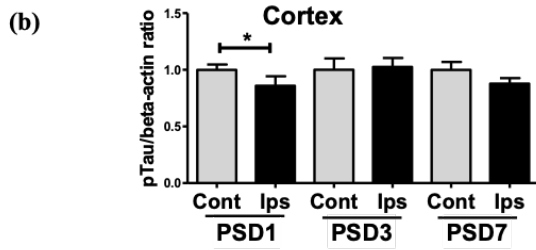
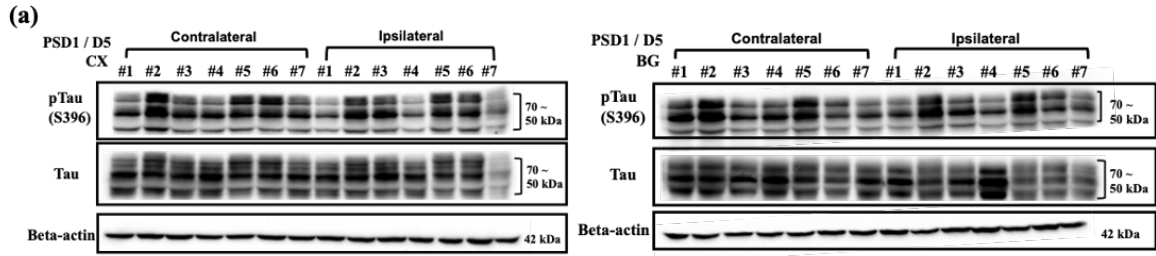


Figure 7. Recurrent TIA-induced phospho-tau and tau alteration in Western blot.

(a) Representative Western blot of p-tau (S396) and Tau from affected cerebral cortex (CX) and basal ganglia (BG) regions in the ipsilateral and contralateral side on PSD1/D5 after recurrent TIA. (n=7). (b,c) Quantitative Western blot analysis of p-tau (S396), tau expression in CX and BG at different time points.

Recurrent TIA (PSD1/D5)

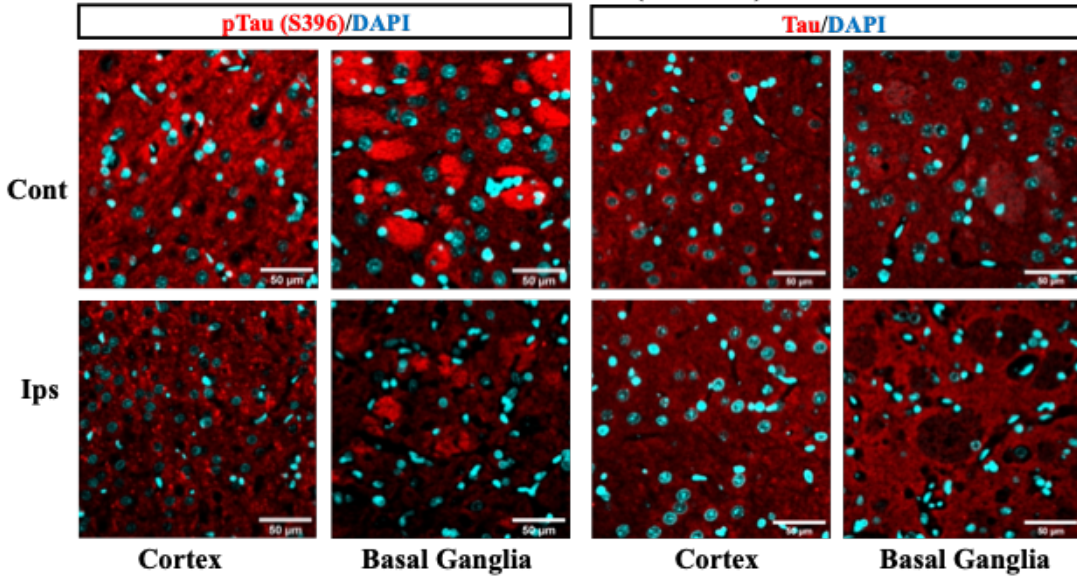


Figure 8. Confocal microscopy of p-tau (S396) and tau alteration after recurrent TIA.

Representative confocal images showing immunofluorescence labeling of p-tau (S396) and tau in affected cortex (CX) and basal ganglia (BG) regions on PSD1/D5. Scale bars = 50 μm .

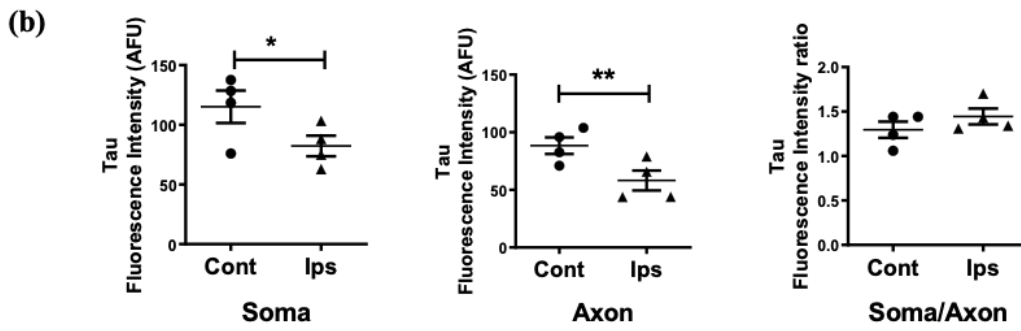
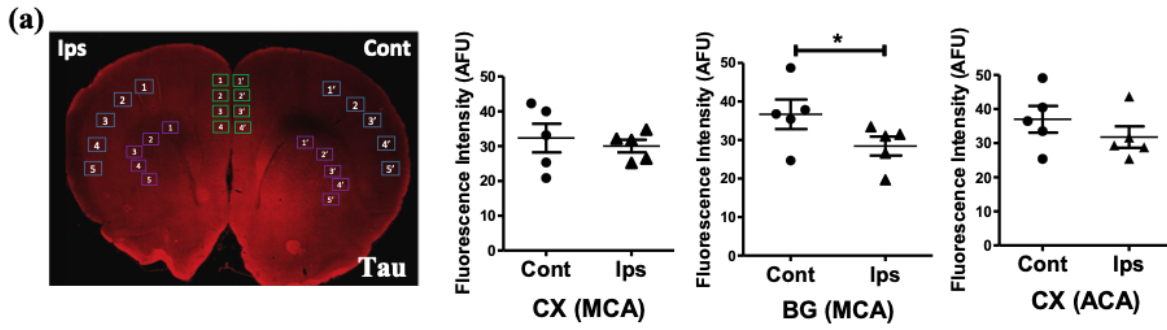


Figure 9. Immunofluorescent quantitative analysis of total tau alteration after recurrent TIA.

(a) The illustration indicating regions of interest (ROIs) used for tau immunofluorescence quantification and data analysis for fluorescence intensity in the affected CX, BG region supplied by MCA and CX supplied by ACA territory on PSD1/D5 after recurrent TIA. (n=5)

(b) Quantitative analysis for tau fluorescence intensity in soma, axon and soma/axon ratio in cerebral cortex region. (n=4) Data are expressed as mean and SEM. *p < 0.05, ***p < 0.001 in paired t-test.

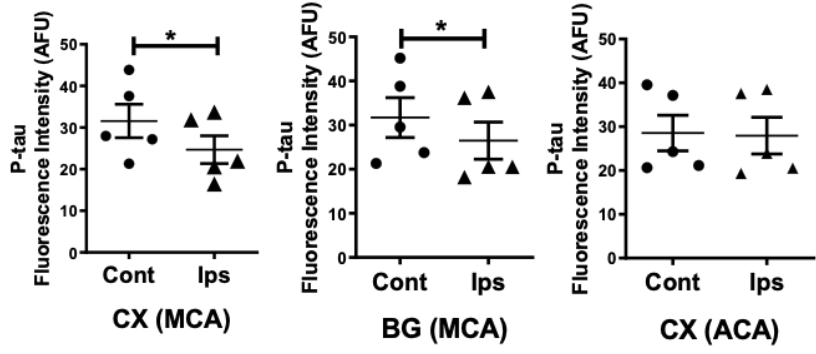
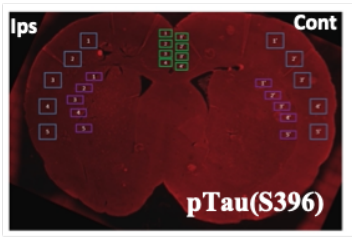
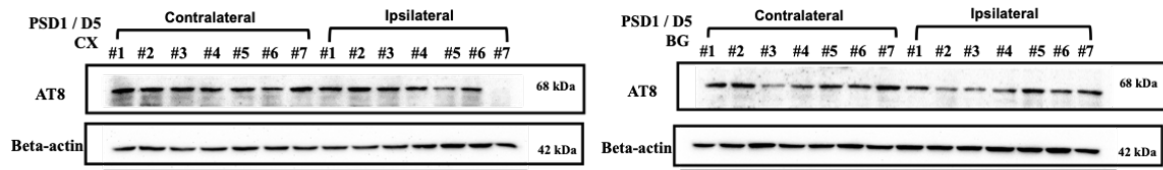


Figure 10. Immunofluorescent quantitative analysis of p-tau (Ser396) alteration after recurrent TIA.

The illustration indicating regions of interest (ROIs) used for quantifications of p-tau (S396) immunofluorescence intensities and data analysis for fluorescence intensity in the affected CX, BG region supplied by MCA and CX supplied by ACA territory at PSD1 /D5 after recurrent TIA. (n=5) Data are expressed as mean and SEM. *p < 0.05 in paired t-test.

(a)



(b)

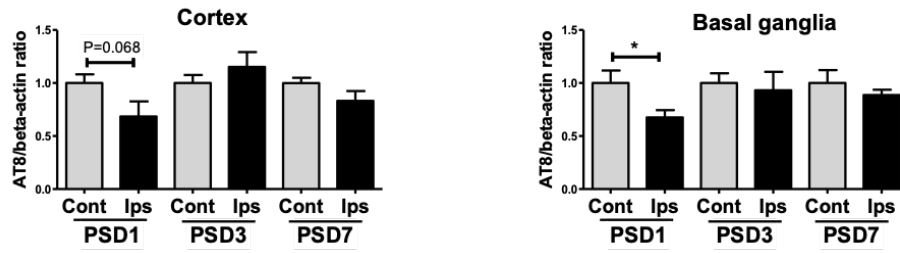


Figure 11. Recurrent TIA-induced phospho-tau (AT8) in Western blot.

(a) Representative Western blot of p-tau (AT8) from affected cerebral cortex (CX) and basal ganglia (BG) regions in the ipsilateral and contralateral side on PSD1/D5 after recurrent TIA. (n=7). (b) Quantitative Western blot analysis of p-tau (AT8) expression in CX and BG at different time points.

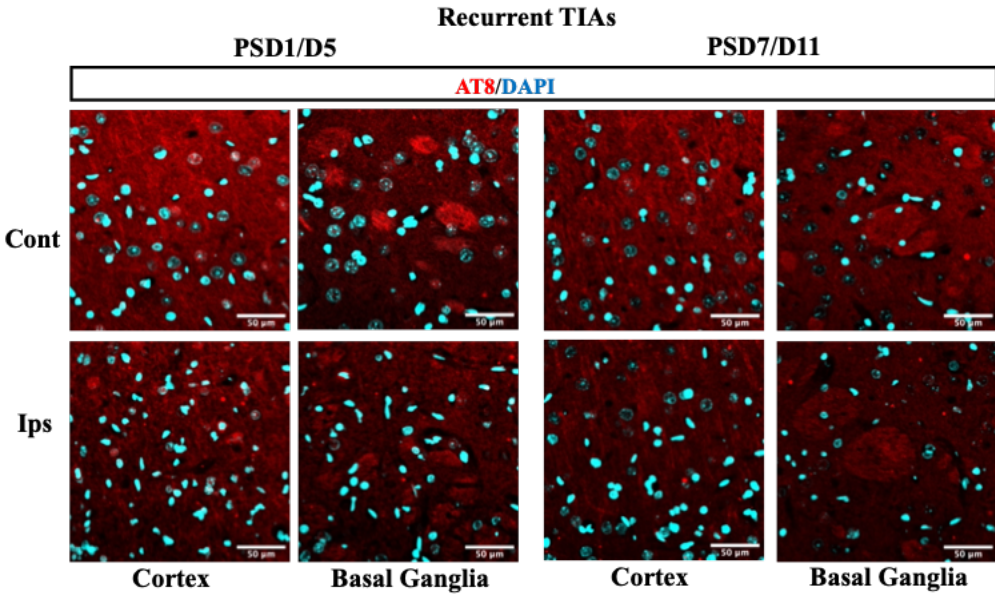
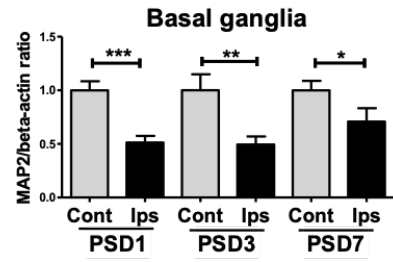
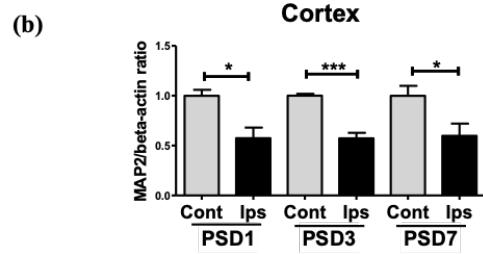
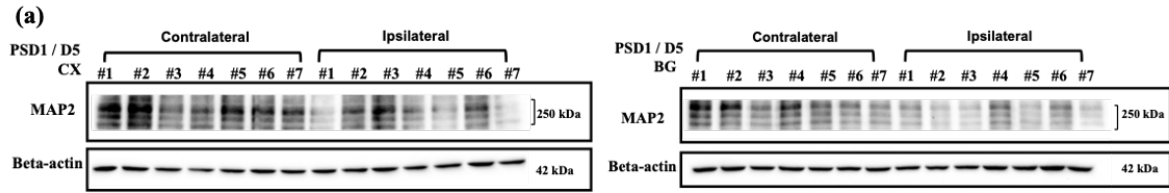


Figure 12. Confocal microscopy of p-tau (AT8) and tau alteration after recurrent TIA.

Representative confocal images showing immunofluorescence labeling of p-tau (AT8) and tau in affected cortex (CX) and basal ganglia (BG) regions on PSD1/D5 and PSD7/D11. Scale bars = 50 μm .



MAP2

Figure 13. Microtubule-associated protein 2 (MAP2) reduction induced by recurrent TIA by Western blots.

(a) Western blots of MAP2 from affected cerebral cortex (CX) and basal ganglia (BG) region in the ipsilateral and contralateral side on PSD1/D5 after recurrent TIA. (n=7). (b) Quantitative western blot analysis of MAP2 expression in CX and BG at different time points. Data are expressed as mean and SEM. * $p < 0.05$, ** $p < 0.01$; *** $p < 0.001$ in paired t-test.

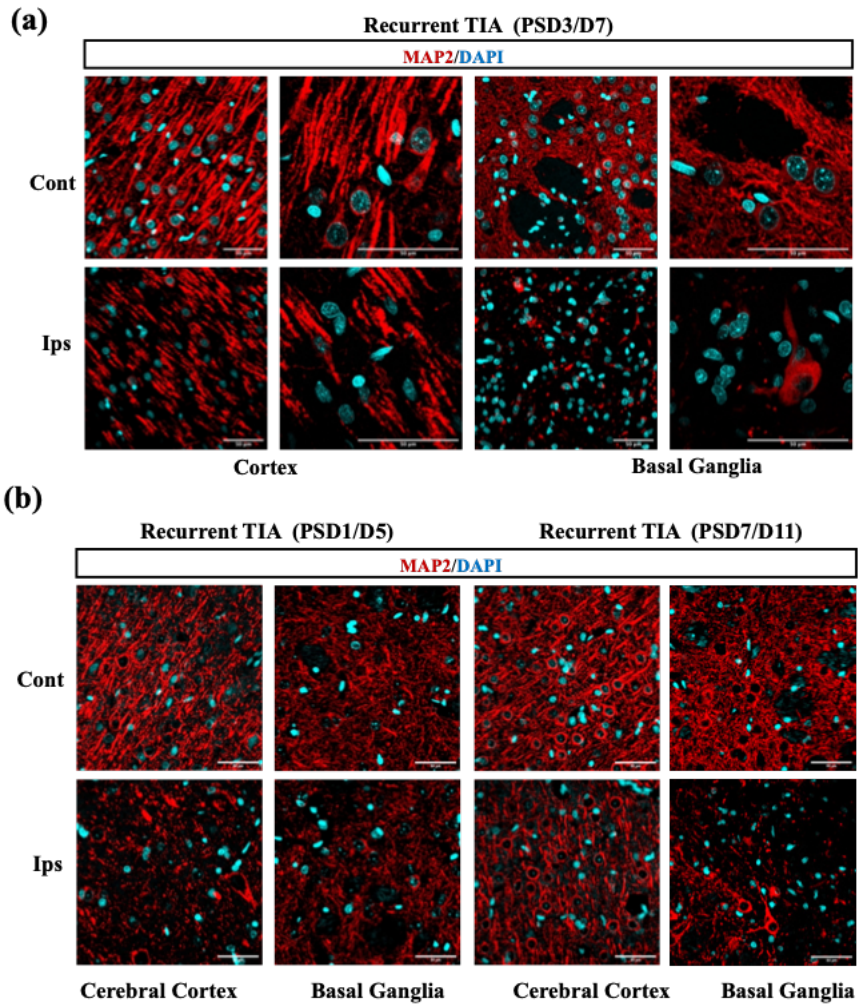


Figure 14. Confocal images of MAP2 expression on PSD1/3/7 after recurrent TIA.

(a) Representative confocal images showing immunofluorescence labeling of MAP2 loss in affected CX and BG regions on PSD3/D7. (b) Representative confocal images showing immunofluorescence labeling of MAP2 loss in affected CX and BG regions at PSD1/ D5 and PSD7/D11 after recurrent TIAs. Scale bars = 50 μ m.

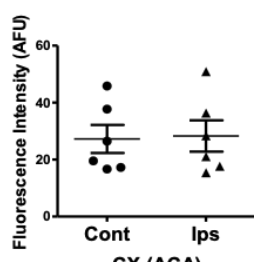
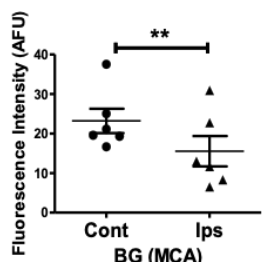
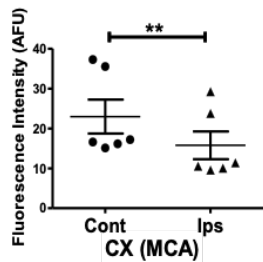
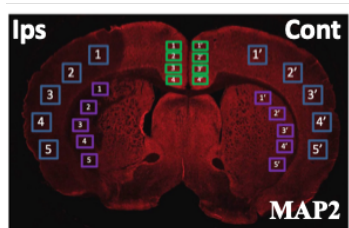
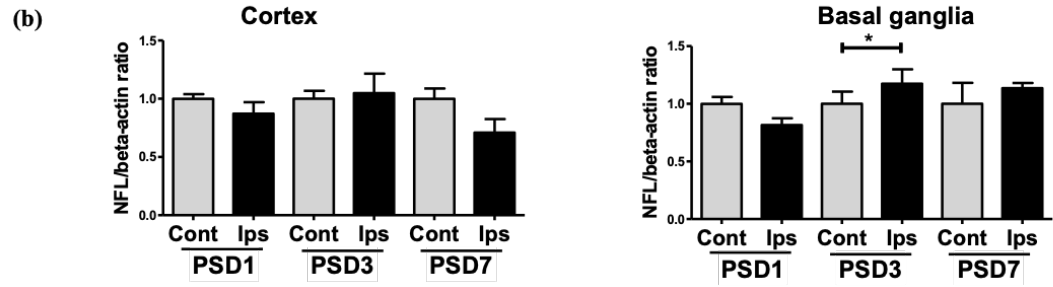
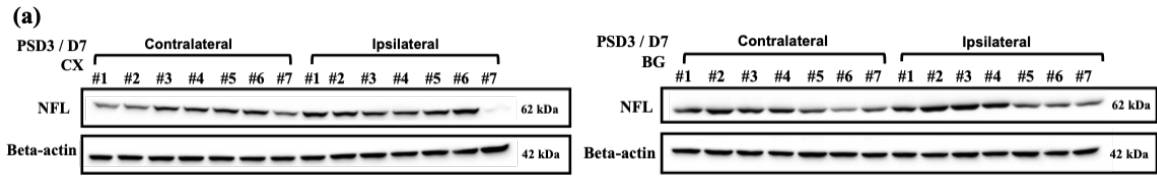


Figure 15. Immunofluorescent quantitative analysis of MAP2 alteration after recurrent TIA.

The illustration indicating regions of interest (ROIs) used for MAP2 immunofluorescence quantification and data analysis for fluorescence intensity in the affected CX, BG region supplied by middle cerebral artery (MCA) and CX supplied by anterior cerebral artery (ACA) territory on PSD3/D7 after recurrent TIA. (n=6) Data are expressed as mean and SEM. *p < 0.05, **p < 0.01; ***p < 0.001 in paired t-test.



NFL

Figure 16. Neurofilament-Light (NFL) elevation after recurrent TIA by Western blots.

(a) Representative Western blot of NFL from affected cerebral cortex (CX) and basal ganglia (BG) region in the ipsilateral and contralateral side on PSD3/D7 after recurrent TIA. (n=7). (b) Quantitative Western blot analysis of NFL expression in CX and BG at different time points. Data are expressed as mean and SEM. *p < 0.05 in paired t-test.

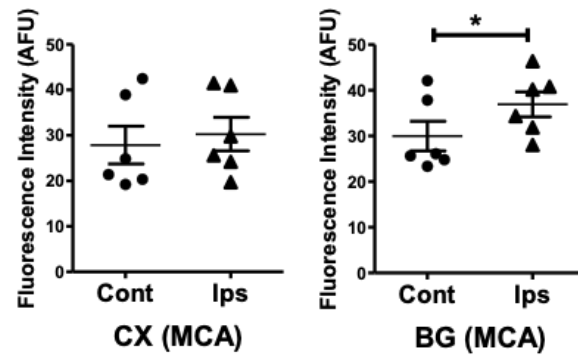
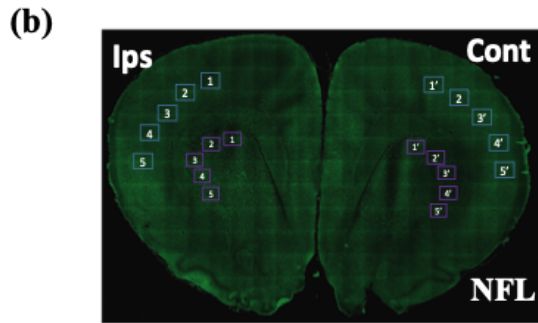
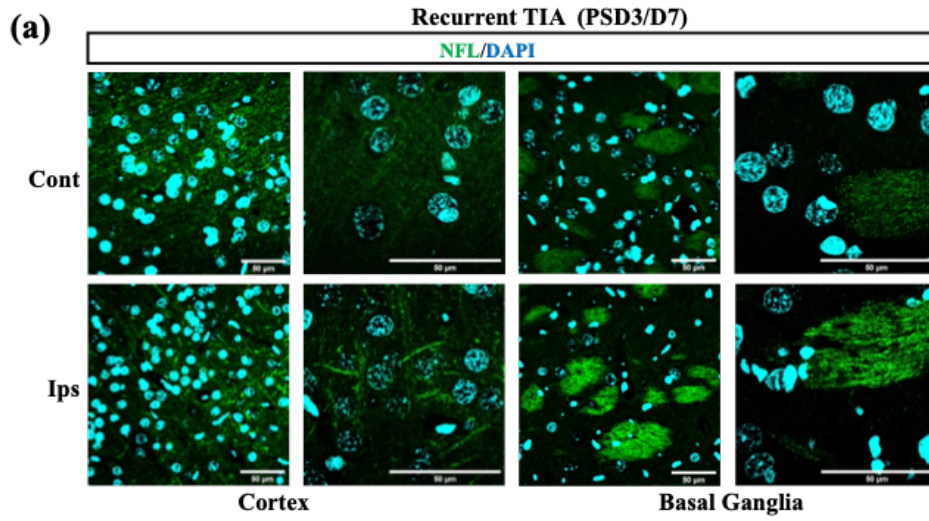


Figure 17. Confocal image and quantitative analysis of Neurofilament-Light (NFL) elevation after recurrent TIA.

(a) Representative confocal images showing immunofluorescence labeling of NFL induction mainly in affected BG region on PSD3/D7. Scale bars = 50 μ m. (b) The illustration indicating regions of interest (ROIs) used for NFL immunofluorescence quantification and data analysis for fluorescence intensity in the affected CX, BG region supplied by MCA at PSD3/D7 after recurrent TIA. (n=6) Data are expressed as mean and SEM. *p < 0.05 in paired t-test.

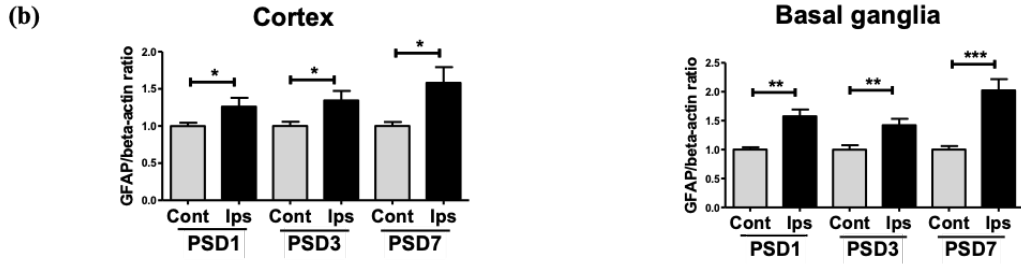
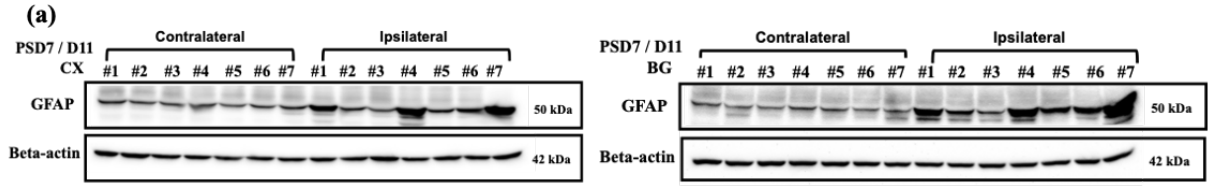
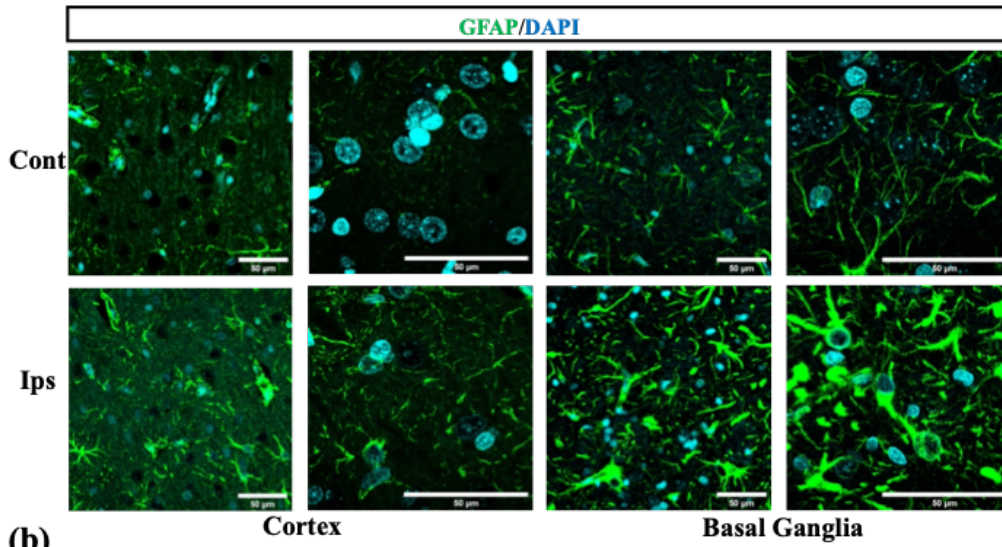


Figure 18. Glial fibrillary acidic protein (GFAP) induction after recurrent TIA by Western blots.

(a) Representative Western blots of GFAP from affected cerebral cortex (CX) and basal ganglia (BG) region in the ipsilateral and contralateral side on PSD7 / D11 after recurrent TIA. (n=7). (b) Quantitative Western blot analysis of GFAP expression in CX and BG at different time points. Data are expressed as mean and SEM. * $p < 0.05$, ** $p < 0.01$; *** $p < 0.001$ in paired t-test.

(a)

Recurrent TIA (PSD7/D11)



(b)

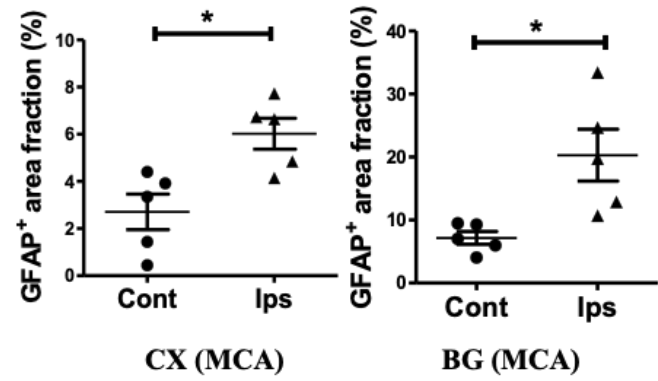
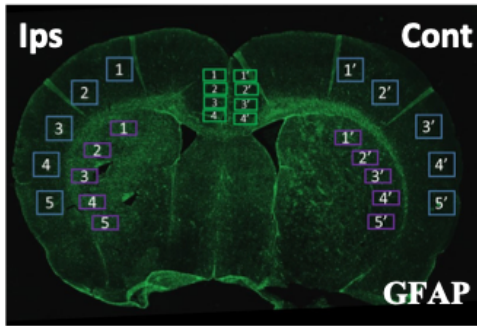


Figure 19. Confocal image and quantitative analysis of Glial fibrillary acidic protein (GFAP) elevation after recurrent TIA.

(a) Representative confocal images showing immunofluorescence labeling of GFAP and induction in affected CX and BG regions on PSD7/D11. Scale bars = 50 μm . (b) The illustration indicating regions of interest (ROIs) used for immunofluorescence quantification and data analysis for GFAP⁺ area fraction in the affected CX, BG region at PSD7/D11 after recurrent TIA. (n=5) Data are expressed as mean and SEM. *p < 0.05, **p < 0.01; ***p < 0.001 in paired t-test.

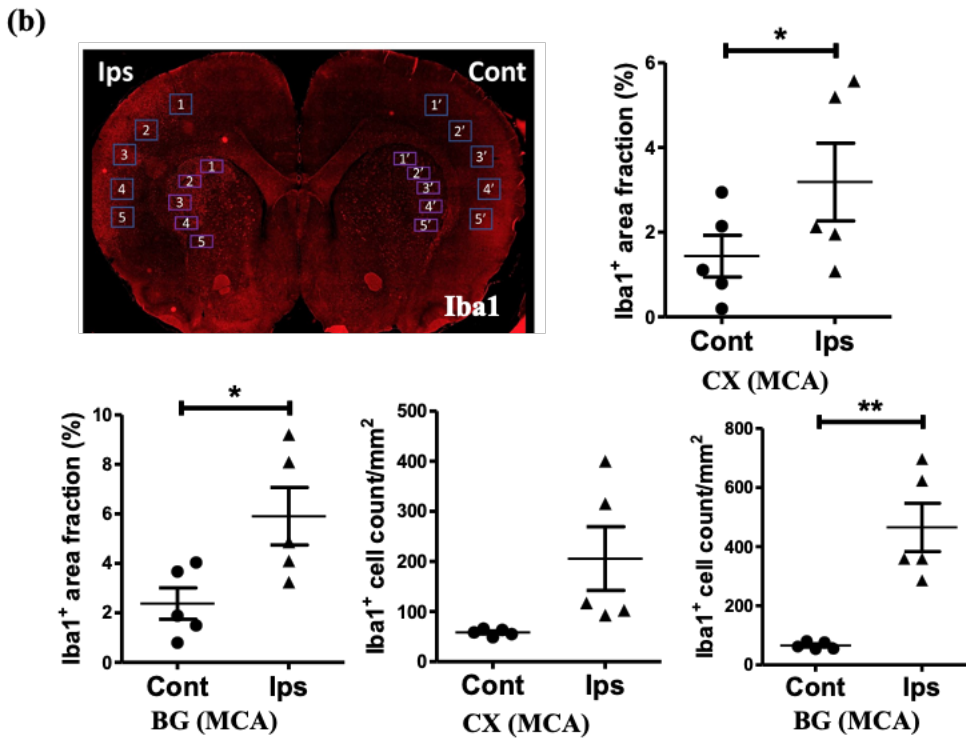
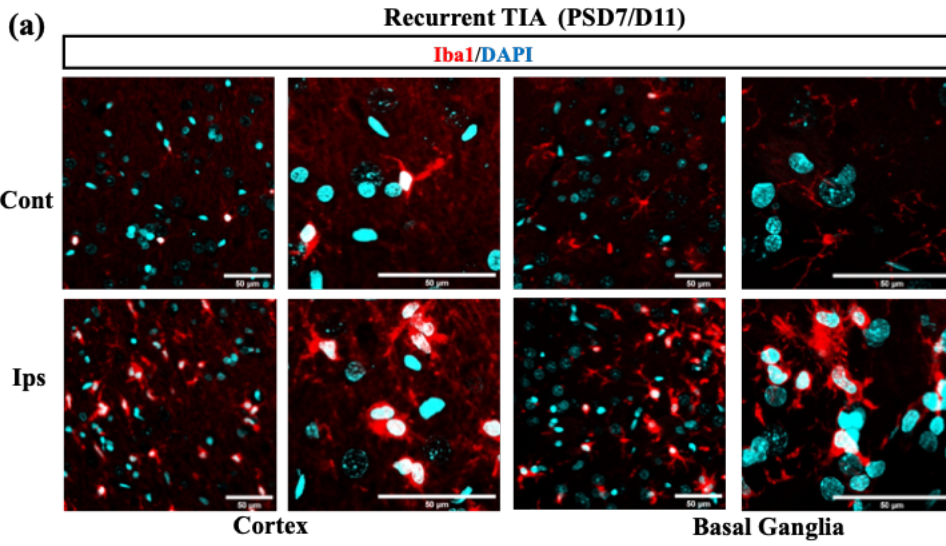


Figure 20. Confocal image and quantitative analysis of ionized calcium binding adaptor molecular 1 (Iba1) alteration after recurrent TIA.

(a) Representative confocal images showing immunofluorescence labeling of Iba1 induction in affected CX and BG regions on PSD7/D11. Scale bars = 50 μ m. (b) The illustration indicating regions of interest (ROIs) used for immunofluorescence quantification and data analysis for Iba1⁺ area fraction and cell count in the affected CX, BG region at PSD7/D11 after recurrent TIA. (n=5) Data are expressed as mean and SEM. *p < 0.05, **p < 0.01; ***p < 0.001 in paired t-test.

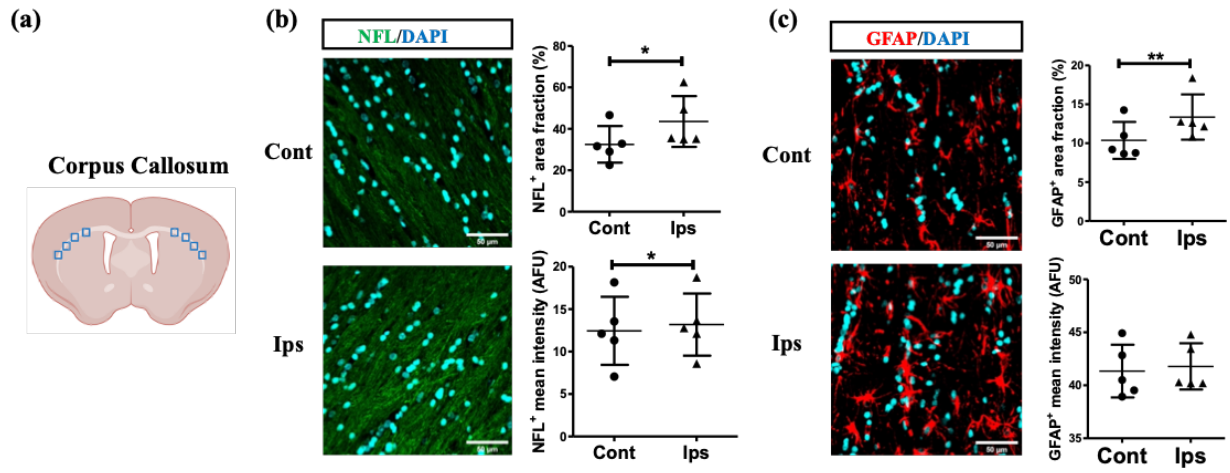


Figure 21. Neurofilament-light (NFL), glial fibrillary acidic protein (GFAP) alteration in corpus callosum in response to recurrent TIA.

(a) A schema depicting the regions of interest (ROIs) from corpus callosum used for semi-quantitative analysis of immunofluorescence staining. (b,c) Representative confocal images showing staining of NFL, GFAP and DAPI in corpus callosum, and data analysis of area fraction and mean intensity for NFL, GFAP on PSD7. Scale bars = 50 μm . (n=5) Data are expressed as mean and SEM. * $p < 0.05$, ** $p < 0.01$ in paired t-test.

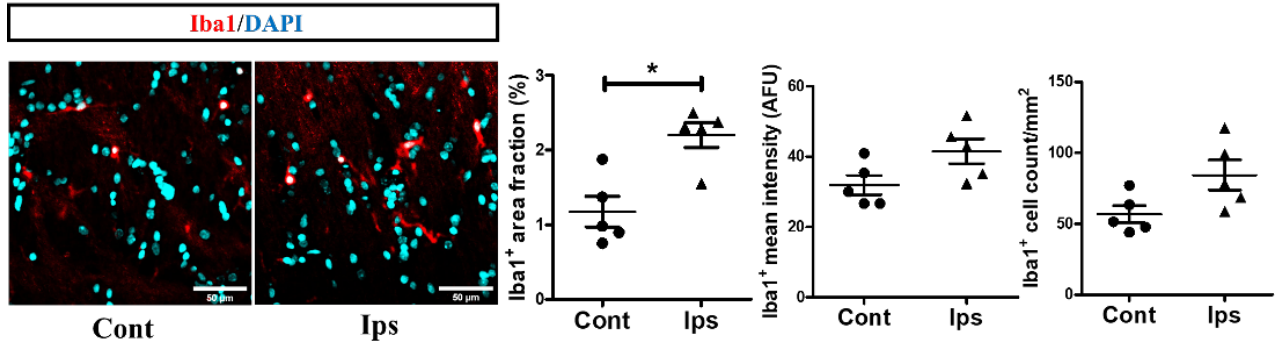


Figure 22. Ionized calcium binding adaptor molecular 1 (Iba1) alteration in corpus callosum in response to recurrent TIA.

Representative confocal images of Iba1 staining and data analysis of Iba1⁺ area fraction, mean intensity and cell count in ROIs on PSD7 after recurrent TIA. Scale bars = 50 μ m. (n=5) Data are expressed as mean and SEM. *p < 0.05, **p < 0.01 in paired t-test.

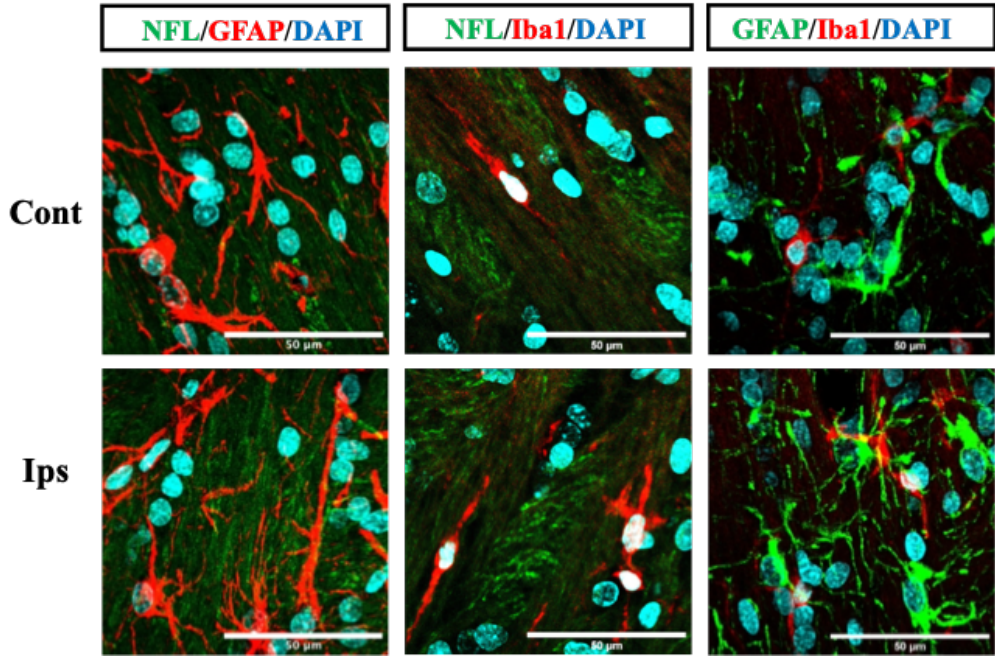


Figure 23. Triple staining of NFL, GFAP, Iba1 and DAPI for potential interaction in corpus callosum induced by recurrent TIA.

Representative confocal microscopy images showing the triple immunofluorescence for NFL, GFAP, Iba1 and DAPI in corpus callosum at PSD7 after recurrent TIAs. Scale bars = 50 μ m.

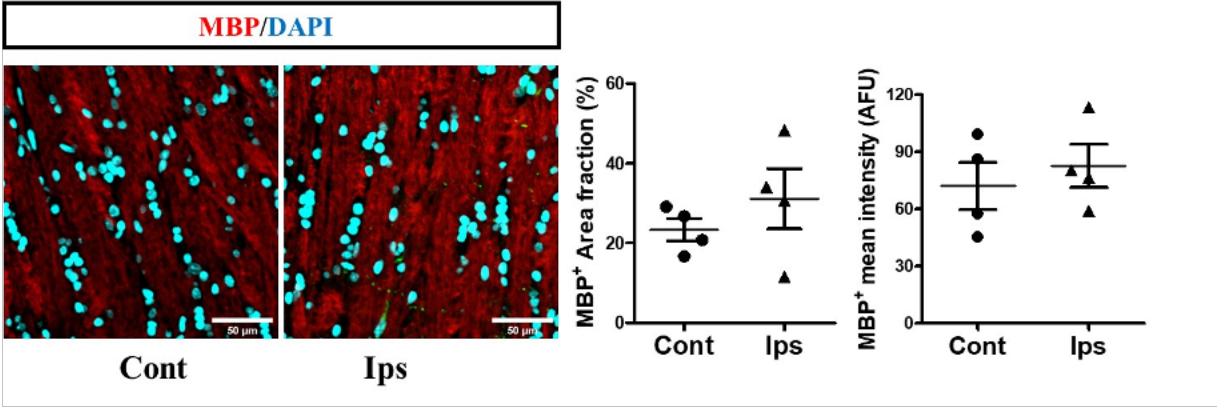


Figure 24. Myelin binding protein (MBP) alteration in corpus callosum in response to recurrent TIA.

Representative confocal images and data analysis of area fraction and mean intensity for myelin basic protein (MBP) in ROIs at PSD7 / D11 after recurrent TIAs. Scale bars = 50 μ m. (n=4) Data are expressed as mean and SEM. $p < 0.05$ in paired t-test.

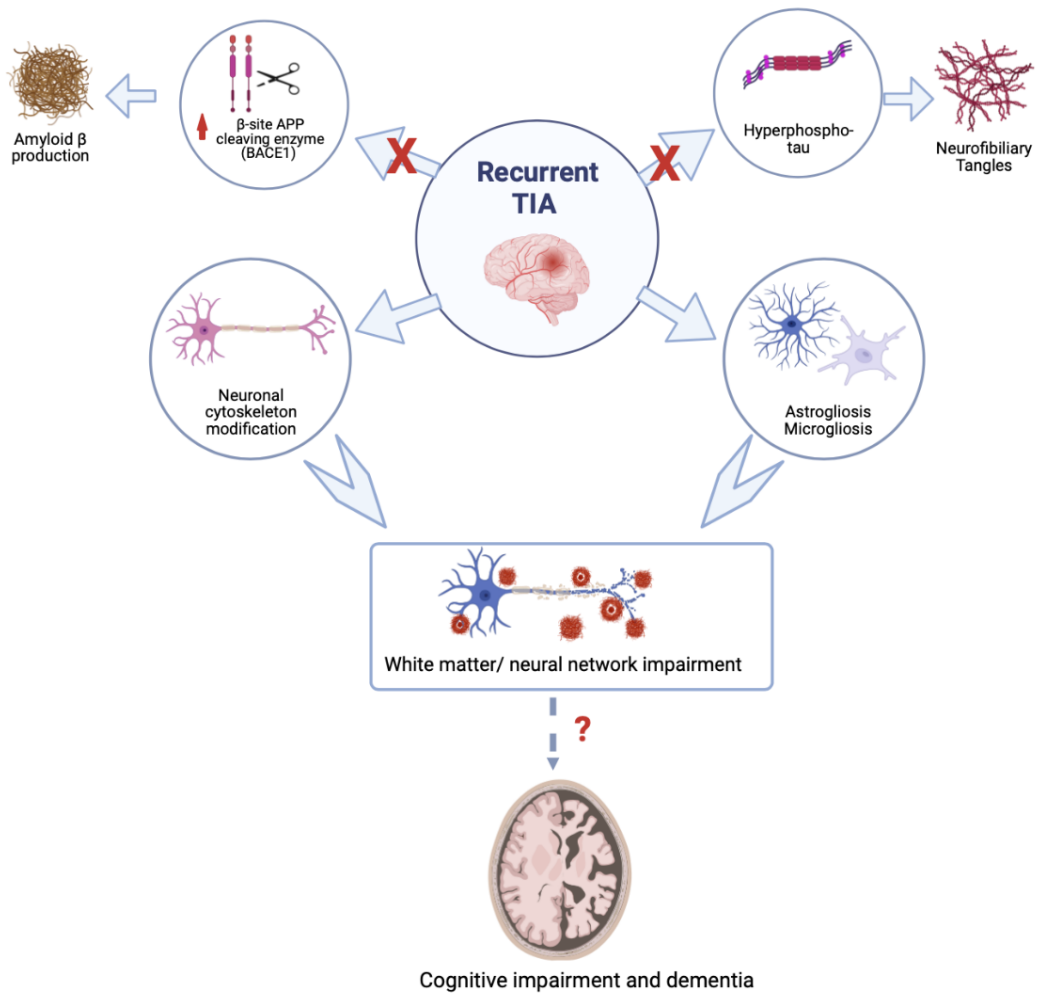


Figure 25. Schematic of pathological changes after recurrent TIA.

Recurrent TIA cannot induce hyperphosphorylation of tau, and BACE1 upregulation, which are the key mediators of neurofibrillary tangles and Amyloid beta formation, respectively. Instead, recurrent TIA can trigger neuronal cytoskeletal modification (MAP2, NFL, tau) and gliosis (astrogliosis and microgliosis) in the TIA-affected cortical and basal ganglia region or corpus callosum, which potentially impair white matter and neural network, contributing to cognitive impairment and dementia.

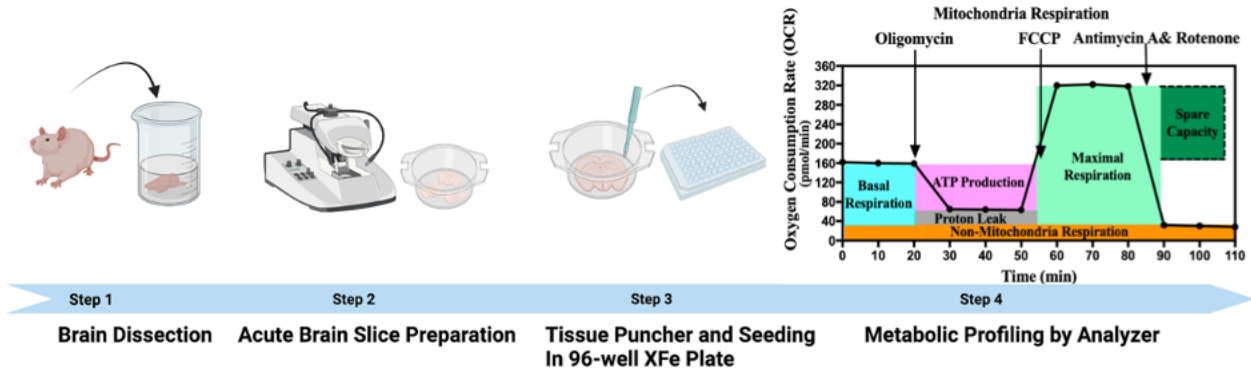


Figure 26. Metabolic analysis of acute tissue punches (0.5 mm diameter) from rodent brain sections (180 μm thick).

Schematic diagram depicts the step of brain harvesting, brain sectioning, tissue punching and seeding in 96-well XFe plate for Seahorse extracellular flux analysis (Created with BioRender.com).

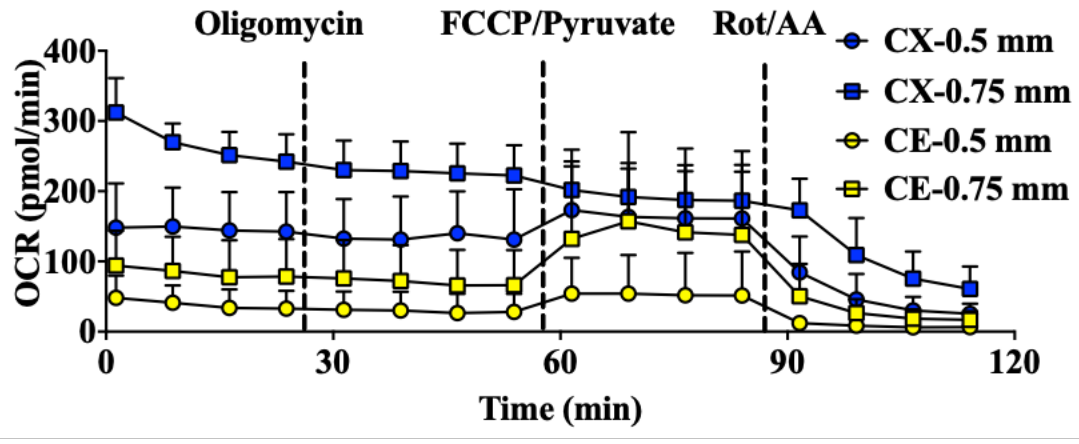


Figure 27. Optimization of brain punch size for metabolic analysis using XF96 analyzer.

Continuous tracings of OCR of different size cerebral cortex and cerebellar punches before and after inhibition of mitochondrial complex V (oligomycin, oligo), addition of mitochondrial oxidative phosphorylation uncoupler FCCP, and inhibition of mitochondrial complexes I/III (rotenone/antimycin A) in the same 96-welled plate. Results are mean \pm SD (n=6-8).

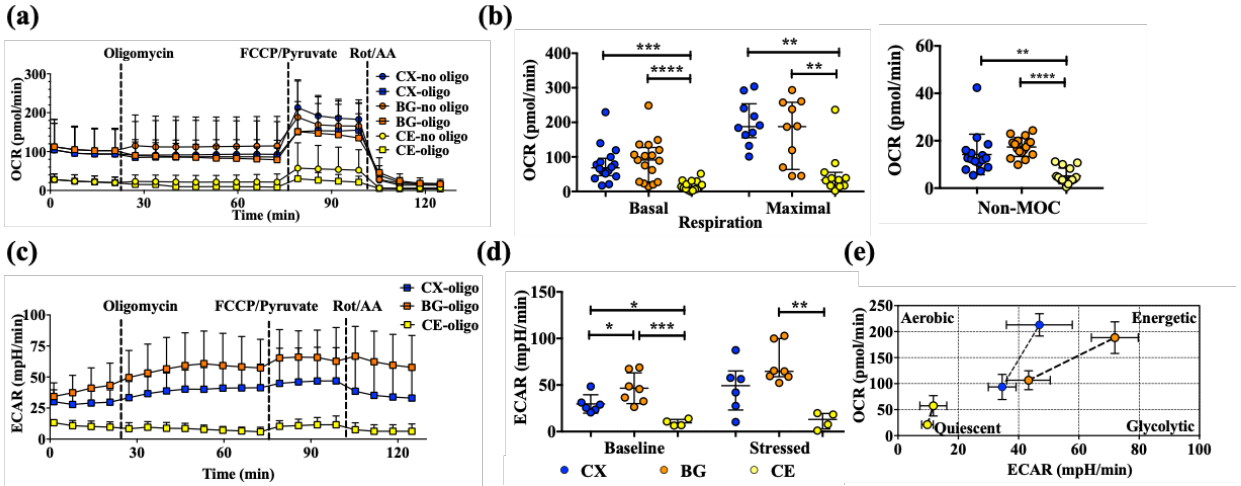
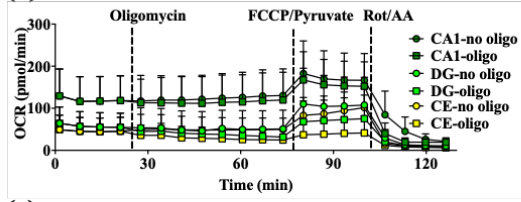


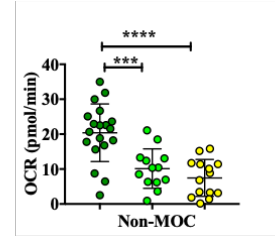
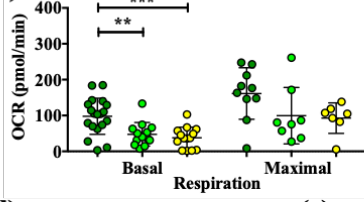
Figure 28. Metabolic analysis of cerebral cortex (CX), basal ganglia (BG), and cerebellum (CE) punches from a 3-month-old female rat using Seahorse XF96 analyzer.

(a) Continuous tracings of oxygen consumption rate (OCR) of CX, BG, and CE punches before and after inhibition of mitochondrial complex V (oligomycin, oligo), addition of mitochondrial oxidative phosphorylation uncoupler FCCP, and inhibition of mitochondrial complexes I / III (rotenone / antimycin A) (Rot / AA) in the same 96-well plate. Non-oligomycin groups (no oligo) were included to obtain the maximal OCR. (b) Scatter dot plots depict basal, maximal respiration, and non-mitochondria respiration (Non-MOC) of each brain region. (c) Continuous tracing of extracellular acidification rate (ECAR) of CX, BG, and CE punches before and after each treatment in the same 96-well plate. (d) Scatter dot plot depicts baseline and stressed ECAR of each brain region. (e) Metabolic profile of CX, BG, and CE from the same assay. Final concentrations: oligomycin 5 μ M, FCCP 1 μ M / pyruvate 0.75 mM, rotenone 1 μ M / antimycin A 1 μ M. Results of OCR / ECAR curve and scatter dot plots are shown as mean \pm SD for normally distributed data, and median with interquartile range for non-normally distributed data. Metabolic profiles are shown as mean \pm SEM. n=4-17, *p < 0.05, **p < 0.01; ***p < 0.001; ****p < 0.0001 in ordinary one-way ANOVA followed by Tukey's multiple comparison test or Kruskal-Wallis test followed by Dunn's multiple comparison test.

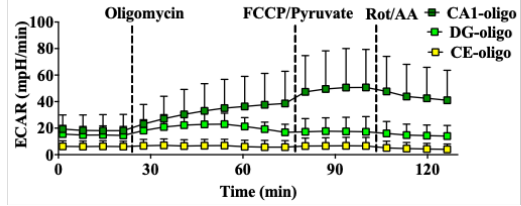
(a)



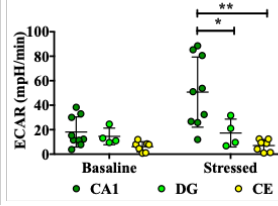
(b)



(c)



(d)



(e)

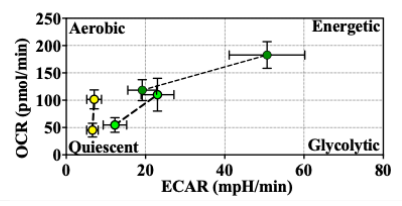


Figure 29. Metabolic analysis of hippocampal CA1, dentate gyrus (DG), and cerebellum (CE) punches from 3-month-old female rat using a Seahorse XFe96 analyzer.

(a) Continuous tracings of OCR of CA1, DG, and CE punches before and after inhibition of mitochondrial complexes and addition of uncoupler in the same 96-well plate. Non-oligomycin groups (no oligo) were included to obtain the maximal OCR. (b) Scatter dot plots depict basal, maximal respiration, and non-mitochondria respiration (Non-MOC) of each brain region. (c) Continuous tracing of ECAR of CA1, DG, and CE punches before and after each treatment in the same 96-well plate. (d) Scatter dot plot depicts baseline and stressed ECAR of each brain region. (e) Metabolic profile of CA1, DG, and CE from same assay. Final concentrations: oligomycin 5 μ M, FCCP1 μ M / pyruvate 0.75 mM, rotenone (Rot) 1 μ M / antimycin A (AA) 1 μ M. Results of OCR / ECAR curve and scatter dot plots are shown as mean \pm SD for normally distributed data, and median with interquartile range for non-normally distributed data. Metabolic profiles are shown as mean \pm SEM. n=4-19, *p < 0.05, **p < 0.01; ***p < 0.001; ****p < 0.0001 in ordinary one-way ANOVA followed by Tukey's multiple comparison test or Kruskal-Wallis test followed by Dunn's multiple comparison test.

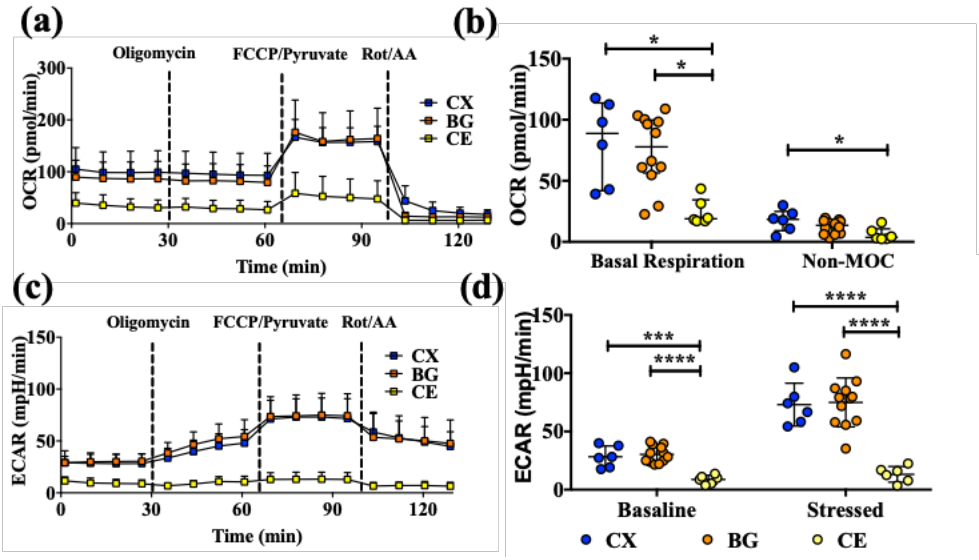


Figure 30. Metabolic analysis of cerebral cortex (CX), basal ganglia (BG), and cerebellum (CE) punches from a 12-month-old female rat using a Seahorse XFe96 extracellular flux analyzer.

(a) Continuous tracings of OCR of CX, BG, and CE punches before and after inhibition of mitochondrial complexes and treatment of uncoupler in the same 96-well plate. Non-oligomycin groups (no oligo) were included to obtain the maximal OCR (not shown). (b) Scatter dot plots depict basal and non-mitochondria respiration (Non-MOC) of each brain region. (c) Continuous tracing of ECAR of CX, BG, and CE punches before and after each treatment in the same 96-well plate. (d) Scatter dot plot depict baseline and stressed ECAR of each brain region. All concentrations of oligomycin and gboxin in the figures were indicated as final concentration in μM . Final concentrations: FCCP 1 μM / pyruvate 0.75 mM, rotenone (Rot) 1 μM / antimycin A (AA) 1 μM . Results of OCR/ECAR curve and scatter dot plots are shown as mean \pm SD for normally distributed data, and median with interquartile range for non-normally distributed data. Metabolic profiles are shown as mean \pm SEM. n=6-20, *p < 0.05, **p < 0.01; ***p < 0.001; ****p < 0.0001 in ordinary one-way ANOVA followed by Tukey's multiple comparison test.

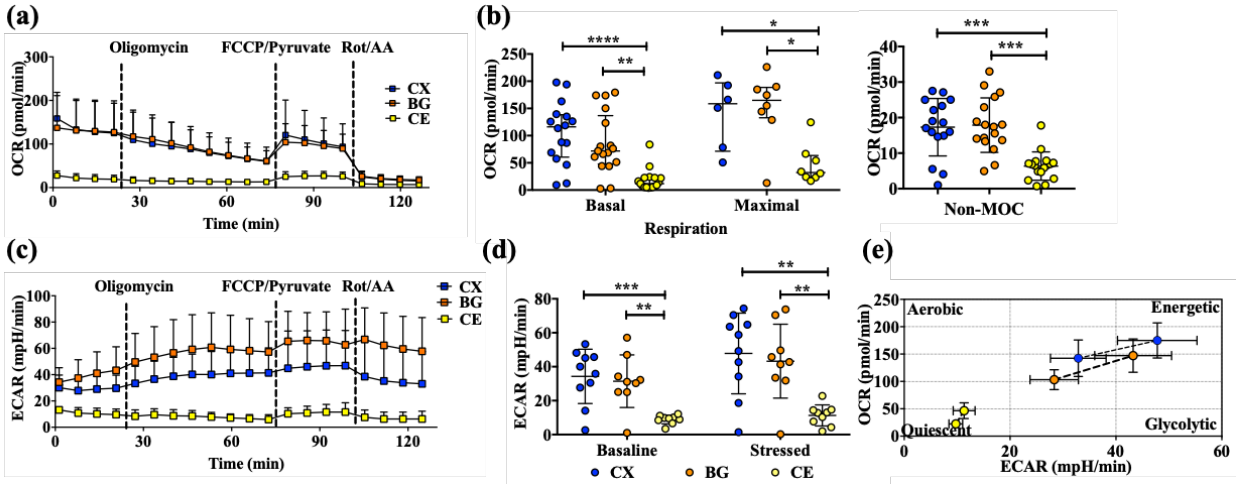


Figure 31. Metabolic analysis of cerebral cortex (CX), basal ganglia (BG), and cerebellum (CE) punches from a 3-month-old female mouse using a Seahorse XFe96 extracellular flux analyzer.

(a) Continuous tracings of OCR of CX, BG, and CE punches before and after inhibition of mitochondrial complexes and treatment of uncoupler in the same 96-well plate. Non-oligomycin groups (no oligo) were included to obtain the maximal OCR (not shown). (b) Scatter dot plots depict basal, maximal respiration, and non-mitochondria respiration (Non-MOC) of each brain region. (c) Continuous tracing of ECAR of CX, BG, and CE punches before and after each treatment in the same 96-well plate. (d) Scatter dot plot depict baseline and stressed ECAR of each brain region. (e) Metabolic profile of CX, BG, and CE from same assay. All concentrations of oligomycin and gboxin in the figures were indicated as final concentration in μM . Final concentrations: FCCP 1 μM / pyruvate 0.75 mM, rotenone (Rot) 1 μM / antimycin A (AA) 1 μM . Results of OCR/ECAR curve and scatter dot plots are shown as mean \pm SD for normally distributed data, and median with interquartile range for non-normally distributed data. Metabolic profiles are shown as mean \pm SEM. $n=6-20$, * $p < 0.05$, ** $p < 0.01$; *** $p < 0.001$; **** $p < 0.0001$ in ordinary one-way ANOVA followed by Tukey's multiple comparison test or Kruskal-Wallis test followed by Dunn's multiple comparison test.

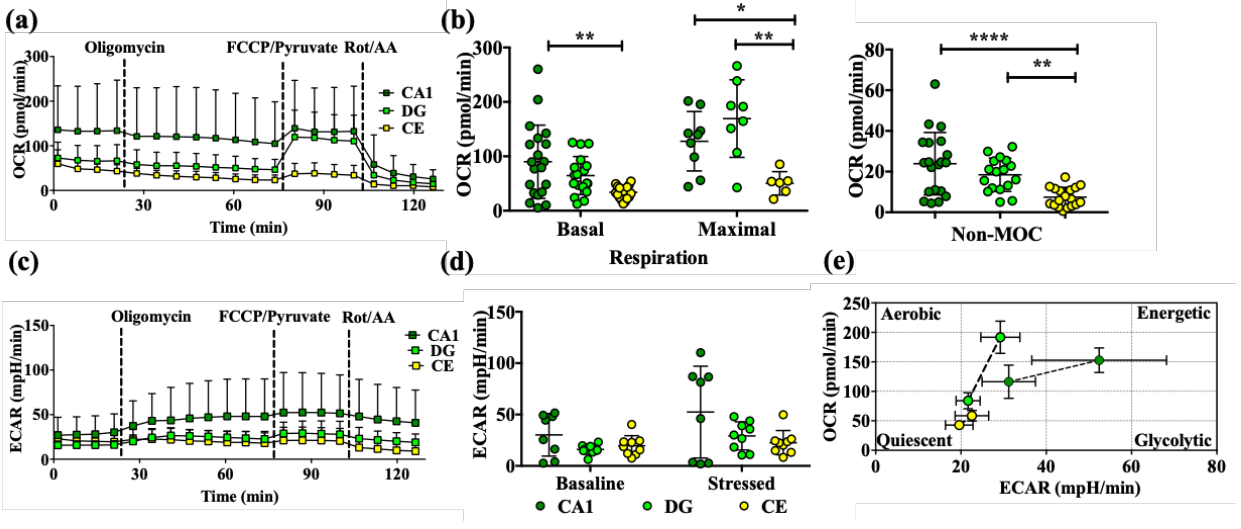


Figure 32. Metabolic analysis of hippocampal (CA1), dentate gyrus (DG), and cerebellum (CE) punches from a 3-month-old female mouse using a Seahorse XFe96 extracellular flux analyzer.

(a) Continuous tracings of OCR of CA1, DG, and CE punches before and after inhibition of mitochondrial complexes and treatment of uncoupler in the same 96-well plate. Non-oligomycin groups (no oligo) were included to obtain the maximal OCR (not shown). (b) Scatter dot plots depict basal, maximal respiration, and non-mitochondria respiration (Non-MOC) of each brain region. (c) Continuous tracing of ECAR of CA1, DG, and CE punches before and after each treatment in the same 96-well plate. (d) Scatter dot plot depict baseline and stressed ECAR of each brain region. (e) Metabolic profile of CA1, DG, and CE from same assay. All concentrations of oligomycin and gboxin in the figures were indicated as final concentration in μM . Final concentrations: FCCP 1 μM / pyruvate 0.75 mM, rotenone (Rot) 1 μM / antimycin A (AA) 1 μM . Results of OCR/ECAR curve and scatter dot plots are shown as mean \pm SD for normally distributed data, and median with interquartile range for non-normally distributed data. Metabolic profiles are shown as mean \pm SEM. $n=6-20$, * $p < 0.05$, ** $p < 0.01$; *** $p < 0.001$; **** $p < 0.0001$ in ordinary one-way ANOVA followed by Tukey's multiple comparison test or Kruskal-Wallis test followed by Dunn's multiple comparison test.

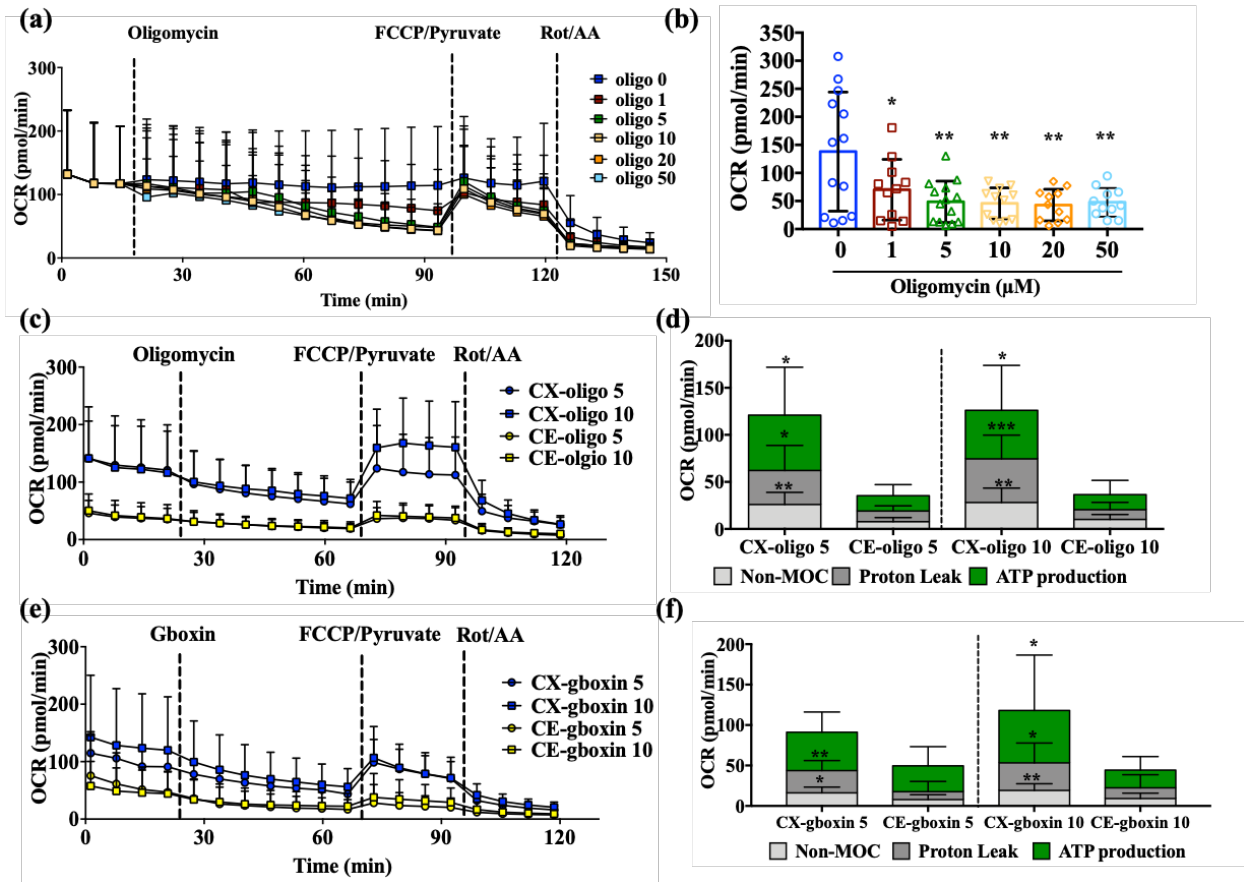


Figure 33. Optimization of mitochondrial complex V inhibition and measurement of non-mitochondria respiration, ATP production-linked respiration, and proton leak-linked respiration in the cerebral cortex and cerebellum.

(a) Continuous tracings of OCR of CX punches from a 3-month-old female mouse before and after inhibition of complex V by different concentration of oligomycin (0, 1, 5, 10, 20, 50 μ M). OCR was measured for 12 cycles of 85 minutes after addition of oligomycin. (b) Bar graph showing dose-dependent effect of oligomycin on OCR. Results are mean \pm SD. n=11-14. *p < 0.05, **p < 0.01 in ordinary one-way ANOVA followed by Tukey's multiple comparison test. (c) Continuous tracings of OCR of CX and CE punches from a 3-month-old mouse before and after inhibition of complex V by oligomycin (5 or 10 μ M) (oligo 5 / 10), addition of FCCP / pyruvate, and rotenone / antimycin A (Rot / AA). (d) Stacked bar graph showing non-mitochondria respiration, ATP production-linked respiration, and proton leak-linked respiration of CX and CE punches. (e) Continuous tracings of OCR of CX and CE punches from 3-month-old female mouse before and after inhibition of complex V by gboxin (5 or 10 μ M) (gboxin 5 / 10), addition of FCCP / pyruvate, and rotenone / antimycin A. (f) Stacked bar graph showing non-mitochondria respiration, ATP production-linked respiration, and proton leak-linked respiration of CX and CE punches. Results are mean \pm SD. n=8-12. *p < 0.05, **p < 0.01; ***p < 0.001 in either un-paired Student t-test for data or Mann-Whitney U test.

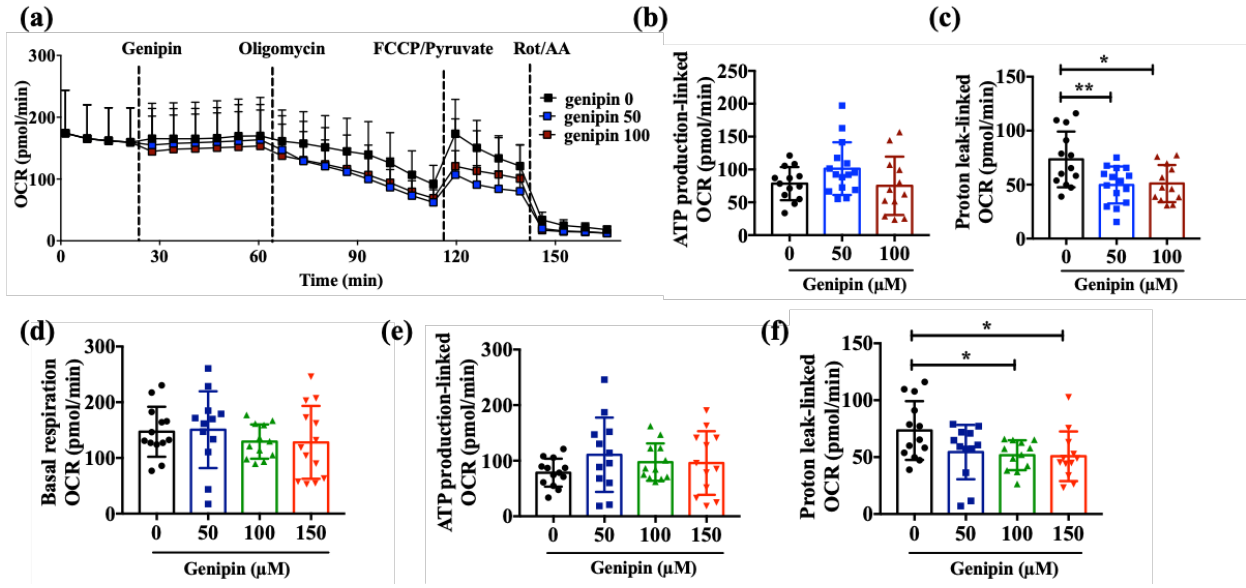


Figure 34. Inhibition of uncoupling proteins decreased proton leak coupled OCR in cerebral cortex punches.

(a) Continuous tracings of OCR of the cerebral cortex punches from a 3-month-old female mouse before and after treatment of UCPs inhibitor (genipin 50, 100 μ M), oligomycin (5 μ M), FCCP 1 μ M / pyruvate 0.75 mM, and rotenone (Rot) 1 μ M / antimycin A (AA) 1 μ M. (b, c) Bar graphs showing the effect of UCPs inhibition by genipin on ATP production coupled (b) and proton leak coupled (c) respiration. (d, e, f) Bar graphs show the effect of chronic treatment (60 minutes) of genipin on basal OCR (d), ATP production-linked OCR (e), and proton leak-linked OCR in the cerebral cortex punches from a 3-month-old female mouse. Results are mean \pm SD. n=12-15. *p < 0.05, **p < 0.01; ***p < 0.001 in ordinary one-way ANOVA followed by Tukey's multiple comparison test.

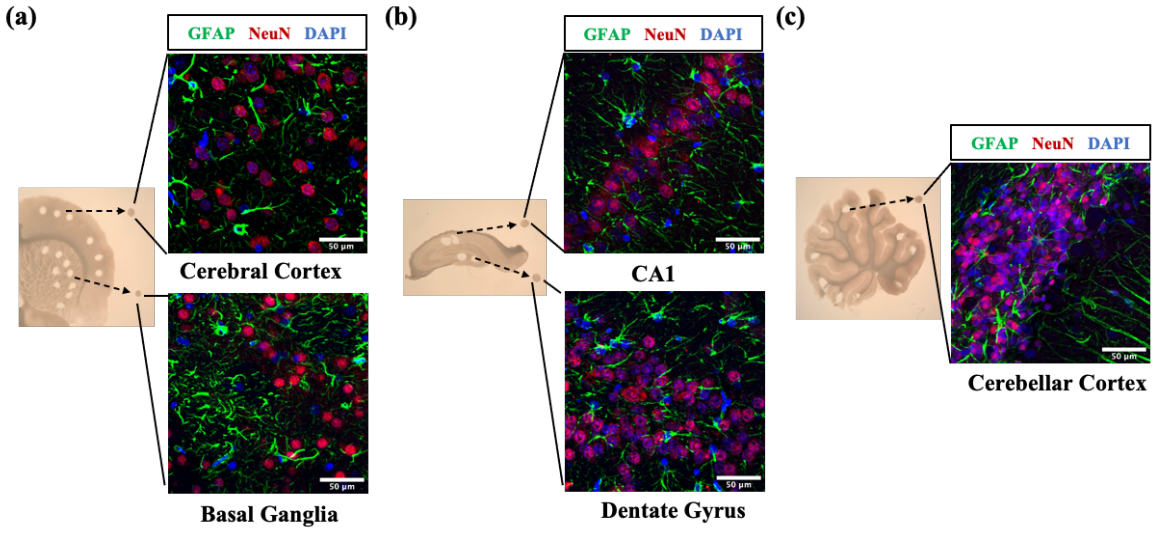


Figure 35. Immunohistochemistry of GFAP, NeuN, and DAPI depict different cellular components of different brain regions.

(a) Coronal section of the cerebrum depicts the location of tissue punches at cerebral cortex and basal ganglia and representative confocal images show neuron and astrocyte components of cerebral cortical and basal ganglia punches. (b) Coronal section of hippocampus depicts the location of tissue punches at hippocampal CA1 and dentate gyrus and representative confocal images show neuron and astrocyte components of CA1 and dentate gyrus punches. (c) Sagittal section of the cerebellum depicts the location of the tissue punches at cerebellar cortex and representative confocal images show neuron and astrocyte components of cerebellar cortex punches. Brain sections were stained by GFAP (green), NeuN (red), and nucleus counterstained by DAPI (blue).

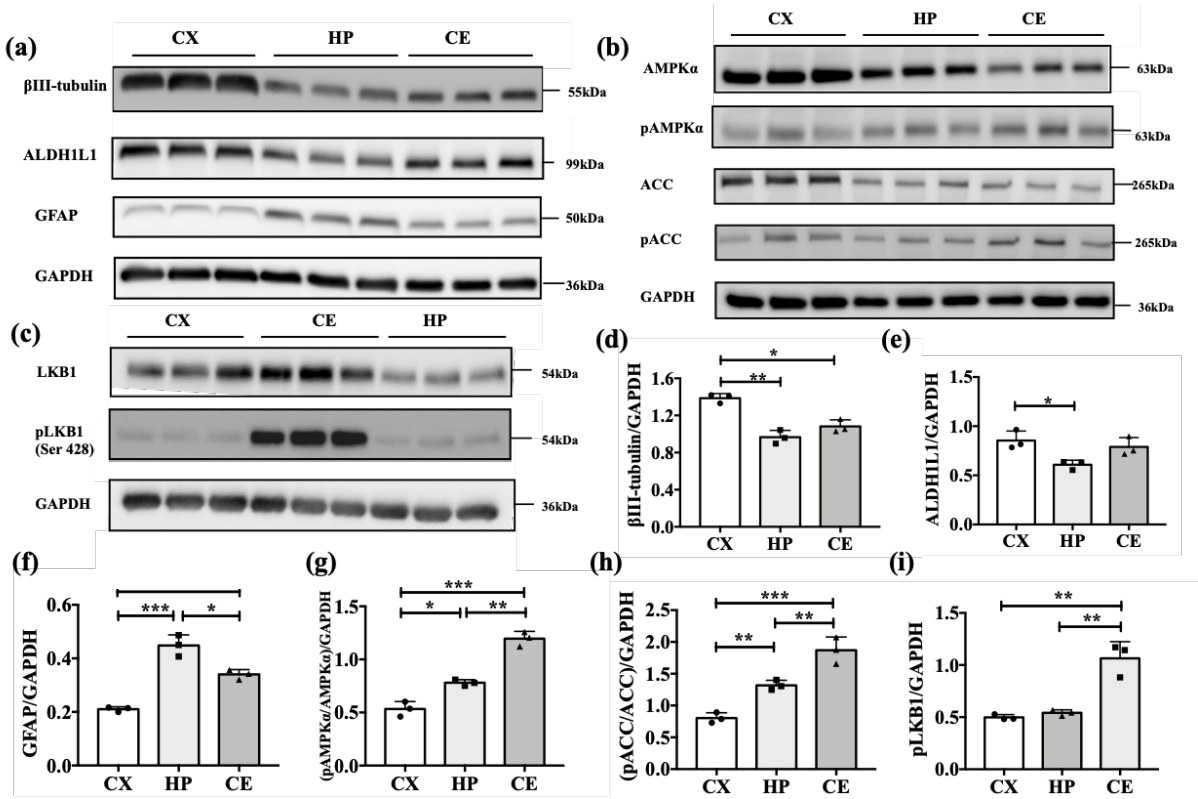


Figure 36. Cellular composition and metabolic signaling in different mouse brain regions.

(a) Western blots of β 3Tubulin, GFAP, ALDH1L1, GAPDH at the cerebral cortex (CX), hippocampus (HP), and cerebellum (CE) of 3-month-old mouse. (b) Western blots of AMPK α , pAMPK α , ACC, pACC, GAPDH at CX, HP, CE of 3-month-old mouse. (c) Western blots of LKB1, pLKB1, GAPDH at CX, HP, CE of 3-month-old mouse. (d-i). Quantitative analysis of β 3-Tubulin, ALDH1, GFAP, pAMPK α , pACC, and pLKB1 expression at CX, HP, and CE. Results are mean \pm SD (n=3). *p < 0.05, **p < 0.01, ***p < 0.001 in repeated measure for one-way ANOVA followed by Tukey's multiple comparison.

Appendix



49 Spadina Ave. Suite 200
Toronto ON M5V 2J1 Canada
www.biorender.com

Confirmation of Publication and Licensing Rights

July 20th, 2022
Science Suite Inc.

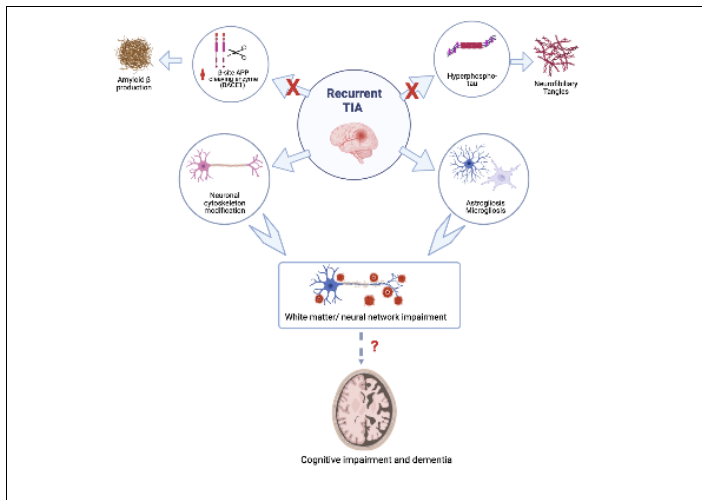
Subscription: Student Plan
Agreement number: OR246LJKY4
Journal name: Linshu Wang dissertation

To whom this may concern,

This document is to confirm that Linshu Wang has been granted a license to use the BioRender content, including icons, templates and other original artwork, appearing in the attached completed graphic pursuant to BioRender's [Academic License Terms](#). This license permits BioRender content to be sublicensed for use in journal publications.

All rights and ownership of BioRender content are reserved by BioRender. All completed graphics must be accompanied by the following citation: "Created with BioRender.com".

BioRender content included in the completed graphic is not licensed for any commercial uses beyond publication in a journal. For any commercial use of this figure, users may, if allowed, recreate it in BioRender under an Industry BioRender Plan.



For any questions regarding this document, or other questions about publishing with BioRender refer to our [BioRender Publication Guide](#), or contact BioRender Support at support@biorender.com.